RICE UNIVERSITY

# AFM-Based Mechanical Nanomanipulation
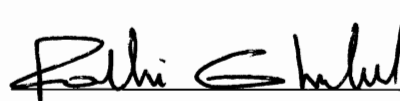
by

**Fakhreddine Landolsi**

A Thesis Submitted
in Partial Fulfillment of the
Requirements for the Degree
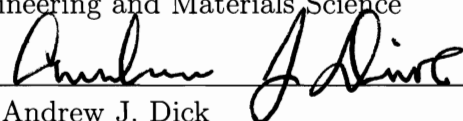
**Doctor of Philosophy**
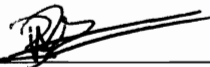
Approved, Thesis Committee:

Dr. Fathi H. Ghorbel, Chair
Professor of Mechanical Engineering and
Materials Science
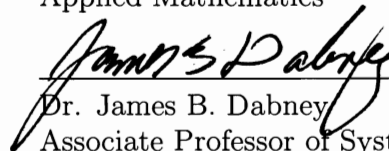
Dr. Marcia K. O'Malley
Associate Professor of Mechanical
Engineering and Materials Science

Dr. Andrew J. Dick
Assistant Professor of Mechanical
Engineering and Materials Science

Dr. Beatrice Riviere
Associate Professor of Computational and
Applied Mathematics

Dr. James B. Dabney
Associate Professor of Systems Engineering
University of Houston - Clear Lake

Houston, Texas

April, 2011

# Abstract

## AFM-Based Mechanical Nanomanipulation

by

### Fakhreddine Landolsi

Advances in several research areas increase the need for more sophisticated fabrication techniques and better performing materials. Tackling this problem from a bottom-up perspective is currently an active field of research. The bottom-up fabrication procedure offers sub-nanometer accurate manipulation. At this time, candidates to achieve nanomanipulation include chemical (self-assembly), biotechnology methods (DNA-based), or using controllable physical forces (e.g. electrokinetic forces, mechanical forces). In this thesis, new methods and techniques for mechanical nanomanipulation using probe force interaction are developed. The considered probes are commonly used in Atomic Force Microscopes (AFMs) for high resolution imaging. AFM-based mechanical nanomanipulation will enable arranging nanoscale entities such as nanotubes and molecules in a precise and controlled manner to assemble and produce novel devices and systems at the nanoscale. The novelty of this research stems from the development of new modeling of the physics and mechanics of the tip interaction with nanoscale entities, coupled with the development of new smart cantilevers with multiple degrees of freedom. The gained knowledge from the conducted simulations and analysis is expected to enable true precision and repeatability of nanomanipulation tasks which is not feasible with existing methods and technologies.

# Acknowledgements

I dedicate this work to my parents Naamen Landolsi and Amel Laouini, and to my brother Mohamed Landolsi.

I would like to express my gratitude to my advisor, Dr. Fathi Ghorbel, who has been my mentor and my guide. His guidance, support, and constant flow of ideas were invaluable to the success of my efforts. I would like to thank Dr. James Dabney for his helpful suggestions and comments. I would also like to thank the rest of my thesis committee, Dr. Marcia O'Malley, Dr. Andrew J. Dick and Dr. Beatrice Riviere, for being helpful and accomodating throughout the process of the defense of this work. Thanks to my colleagues and friends, Sushant Dutta, Yan Chen, Andrew Lynch and David Trevino, for their help and camaraderie throughout.

Finally, thanks to all my family and friends, who have been my pillars of strength through thick and thin.

# Table of Contents

# List of Publications

Landolsi, F., Ghorbel, F. H. , Lou, J., Lu, H. and Sun, Y., **"Nanoscale Friction Dynamic Modeling,"** *ASME Journal of Dynamic Systems, Measurement and Control,* 131 (2009), 061102.

Landolsi, F., Sun, Y., Lu, H., Ghorbel, F. H. and Lou, J., **"Regular and Reverse Nanoscale Stick-Slip Behavior: Modeling and Experiments,"** *Applied Surface Science,* 256 (2010) 2577-2582.

Landolsi, F. and Ghorbel, F. H., **"Duo-Biomorph Based AFM Cantilever for Nanomanipulation,"** *Smart Materials and Structures,* 19 (2010) 065028.

Landolsi, F., Ghorbel, F. H. and Dabney, J. B., **"Friction and Adhesion Coupling During AFM-based Nanomanipulation,"** *ASME Journal of Dynamic Systems, Measurement and Control,* (in review).

Landolsi, F. , Ghorbel, F. H. and Dick, A. J., **"Analysis of the Occurrence of Stick-Slip in AFM-Based Nano-Pushing,"** *Journal of Nonlinear Dynamics,* (in review).

Landolsi, F. and Ghorbel, F. H., **"Adhesion-Based Multi-Sample Nanomanipulation,"** *ASME Journal of Dynamic Systems, Measurement and Control,* (in review).

Landolsi, F. and Ghorbel, F. H., **"Design and Control of a New Nanomanipulator,"** *Smart Materials and Structures,* (in review).

Landolsi, F., Dabney, J. B. and Ghorbel, F. H., **"An AFM-Based Nanomanipulation Model Describing the Atomic Two Dimensional Stick-Slip Behavior,"** *Proc. of the ASME International Mechanical Engineering Congress and Exposition,* (10 pages) Seattle, Washington November 11-15, 2007.

Landolsi, F., Dabney, J. B. and Ghorbel, F. H., **"Effect of Interaction Modeling in AFM-Based Nanomanipulation,"** *Proc. of the ASME 2008 Dynamic Systems and Control Conference,* (8 pages) Ann Arbor, Michigan, October 20-22, 2008.

Landolsi, F., Dabney, J. B. and Ghorbel, F. H., **"Vibrational AFM-Based Nano-Placing Modeling and Simulation,"** *Proc. of the ASME 2009 Dynamic Systems and Control Conference,* (8 pages) Hollywood, California, October 12-14, 2009.

Landolsi, F., Dabney, J. B. and Ghorbel, F. H., **"A New AFM Cantilever Design for Manipulation at the Nanoscale,"** *Proc. of the ASME 2010 Dynamic Systems and Control Conference,* (8 pages) Cambridge, Massachusetts, September 13-15, 2010.

Landolsi, F., Dabney, J. B. and Ghorbel, F. H., **"Control of a Piezotube-Based Smart Nanomanipulator,"** *Proc. of the IEEE 2010 Conference on Decision and Control,* (6 pages) Atlanta, Georgia, December 15-17, 2010.

# List of Figures

# List of Tables

# Chapter 1

# Introduction

## 1.1  Nanotechnology

Nanotechnology deals with the exploitation of the physical, chemical and biological prop-
erties of nano-structures [1]. These tiny structures have characteristic dimensions ranging
from 1 to 100 nanometers (1 nm $= 1e-9$m). At this scale, interesting physical, chemical,
and biological properties, that differ in important ways from the properties of bulk mate-
rials, emerge enabling novel applications. Nanotechnology promises to establish markets
and industries that would have not been possible otherwise. The total U.S. federal invest-
ment in this field since the establishment of the National Nanotechnology Initiative (NNI)
in 2001 has reached nearly $12 billion dollars [2]. This investment in research and devel-
opment continues to grow as shown in Figure 1.1. Different countries around the world,
mainly Japan, the European Union and China, established their own nanotechnology ini-
tiatives. The Japanese government reportedly pledged to match the U.S. investment in
nanotechnology dollar for dollar [3]. Collaboration between different countries and labora-
tories is encouraged. Several workshops, e.g. those jointly sponsored between the National
Science Foundation (NSF) and the European Commission (EC), have defined milestones
to boost research effort on the field of nanotechnology [4, 5, 6].

Nanotechnology is new as a field, but surprisingly old as research and practice. For
instance, the Chinese were known more than thousand years ago to color their ceramic
porcelains using $Au$ nanoparticles. More examples exist in the engineering of catalysts,
colloidal dispersions and metallic quantum dots that started centuries ago. The current

wide interest in nanotechnology is boosted by the increasing need to reduce the size of electronic devices. Nanotechnology, as a field, includes but is not limited to (i) understanding the scale effects on the physical characteristics and performances of materials and structures, (ii) processing and synthesizing nano-materials, (iii) fabricating nano-devices and nano-structures, (iv) building new tools for characterization at the nanoscale, and (v) developing a corresponding simulation framework.

Potential applications of nanotechnology are of relevance in different fields such as aerospace, automotive and appliance industries, biotechnology, medicine, communications and security. The main challenges for nanotechnology include the ability to build, test, model and simulate these small structures. In fact, nano-systems are too small for direct measurements and exhibit too many fluctuations to be treated monolithically in space and time. Advances in several research areas increased the need for more sophisticated fabrication techniques and better performing materials. Fabricating improved structures increasingly rely on the ability to control, position and process materials on very small length scales [7].
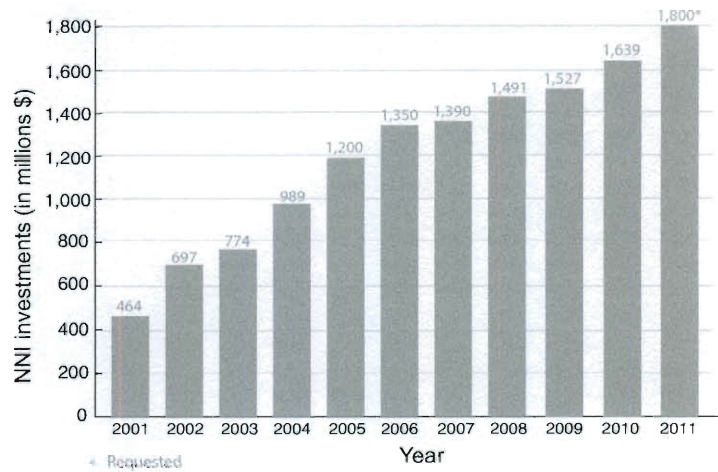


**Figure 1.1:** Evolution of the U.S. federal funding in nanotechnology

## 1.2 Nanorobotics

Central to nanotechnology challenges is the notion of Nanorobotics which is still a science fiction domain with many potentials. We would like to believe that at some point in the future, we would be able to create robots at the nanoscale to perform tasks repeatedly and precisely and produce novel nano-devices and nano-systems. Drexler [8] laid down a school of thought that future manufacturing will rely on massively parallel information processes leading to the inexpensive assembly of structures. Implications would be more than revolutionary to the way we live.

Nanorobots could be realized with existing technologies including micro-machining, protein engineering and polymer synthesis in which perhaps protein-based nanorobots could autonomously build nano-systems out of molecules that are from much more sustainable materials such as metals and polymers. These in turn, will construct stronger and sustainable nanorobots. A nanorobot must have all the attributes of a robot that we currently know: autonomy, actuation, sensing and the ability to compute, but perhaps with different physics domains than the macro-world. Bees, for example, communicate by smell and dancing. Furthermore, it is expected that individual nanorobots will be quite simple and with very limited capabilities. But swarms of nanorobots will collectively be a smart and capable nano-system.

The long ride we still need to take to create nanorobots did not stop chemists, physicists, material scientists, engineers and others to synthesize and process nano-materials and nano-structures and to try to guarantee such level of control. These techniques can be subdivided into two main categories: bottom-up and top-down approaches. In bottom-up fabrication atoms and/or molecules are used to form nano-materials whereas top-down techniques are subtractive processes that start with bulk materials to construct the desired features. Chemical Vapor Deposition (CVD), Atomic Layer Deposition (ALD), self-assembly and direct force nanomanipulation are few examples of bottom-up techniques. Top-down methods include thermal (electrospinning), high energy (arc discharge, laser

ablation) and chemical techniques (anodizing).

Recently, special interest was given to self-assembly and direct force nanomanipulation as potentially good candidates for repeatable and controllable fabrication at the nanoscale. Figure 1.2 summarizes the definition of nanomanipulation as being *the manipulation of nanoscale entities in a repeatable and controlled manner to produce novel devices and systems* [9]. At this time, candidates to achieve nanomanipulation include chemical processes (self-assembly), using biotechnology methods (DNA-based), or using controllable physical forces. The latter could be achieved for example by laser trapping, electrokinetic forces, or with micro-cantilever tip force interactions.
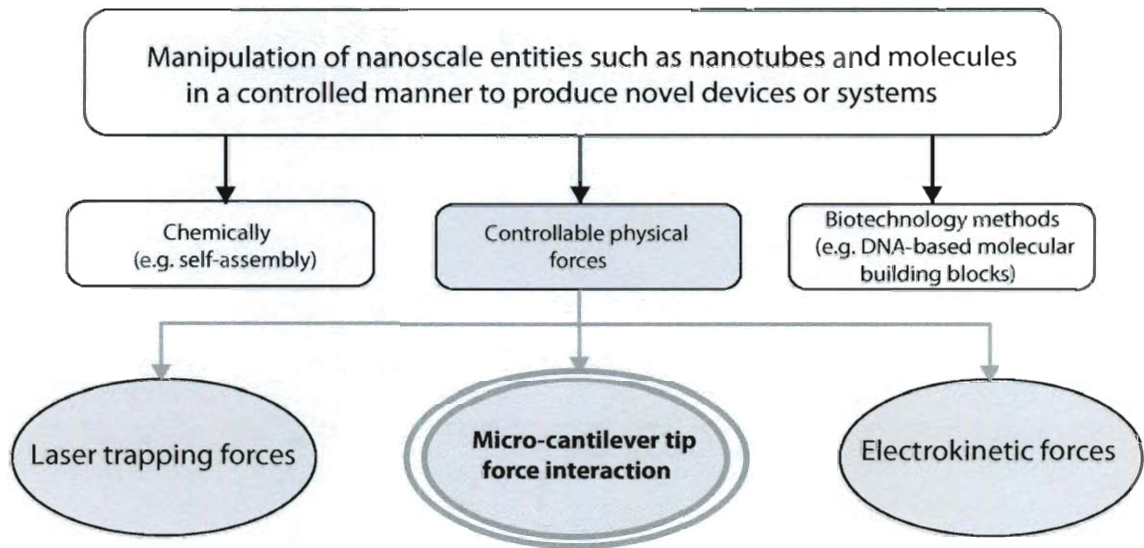


**Figure 1.2:** Nanomanipulation methods [10]

Similar to synthetic approaches, self-assembly techniques rely on the combination of nanoscale patterning and chemical methods to create improved nano-structures [11, 12]. Self-assembly can lead to highly structured systems arranged based on selective control of non-covalent interactions between atoms and molecules. Scaling this technique to macro-molecular structures allows to extend the results to larger length scales. Building blocks used in self-assembly cover a wide range of materials including metallic and non-metallic

cores. However, self-assembly techniques cannot be applied to build non-symmetric structures and to test and validate nano-devices. Direct force nanomanipulation promises higher control levels and sets an interesting framework for nano-device diagnostics and analysis [13, 14].

## 1.3 Direct Force Nanomanipulation

Direct force nanomanipulation encompasses all methods aimed toward fabricating nanoscale structures by applying forces at the nanoscale. Advantages of these techniques include the possibility of fabricating nano-devices with comparable performance. Potential applications are phenomenal. Highly resistive nano-structured alloy and composite materials can be used to improve jet fuselages, internal combustion systems and engines [15]. Nano-devices exploiting advanced semiconductors, molecular electronics and spintronics will lead to extremely high density data storage systems. Moreover, the precise manipulation of single Carbon Nanotubes (CNTs) will enable a wide range of experiments including tube-tube contact mechanics, electrical contact between selected tubes, and the testing of elementary CNT device geometries [16, 17].

Direct force manipulation tools include specially designed manipulators (e.g. Zyvex S100 [18]) or Scanning Probe Microscopes (SPMs) that evolved from imaging setups to promising nanomanipulators. The Zyvex S100 system, for instance, has four probes mounted horizontally in plane each at 90° angle. The probe cross-section can be either rectangular or tubular with a tapered conical tip. The S100 system with the correct co-ordination of the four probes is able to do push or pick and place operations to position objects. SPMs represent our window to the nanoscale. These microscopes can achieve a resolution of few Angstroms ($1\mathring{A} = 1e-10m$). The most widely used SPMs are the Scanning Tunneling Microscopes (STMs) and the Atomic Force Microscopes (AFMs). Figure 1.3 compares the resolution of some SPMs to other microscopes and to the characteristic dimensions of natural mechanisms and structures.
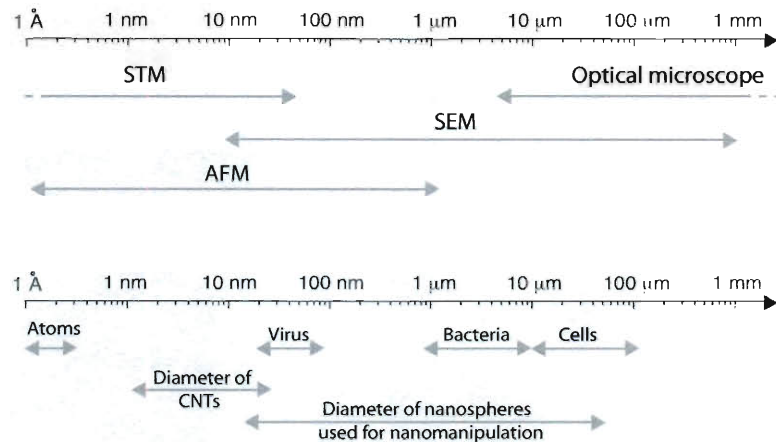
**Figure 1.3:** Order of magnitude of the resolution of common microscopes

## 1.3.1 STM-Based Nanomanipulation

STMs are the first type of SPMs invented in 1981 by Binnig and Rohrer [19, 20]. The functioning principle of an STM is based on the quantum tunneling effect. A bias voltage is applied between an atomically sharpened tip and a sample (Figure 1.4).
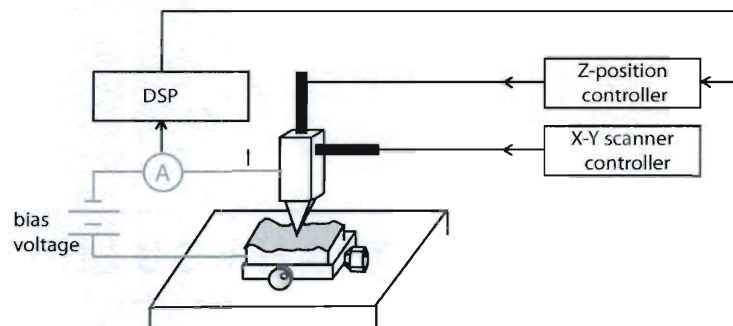


**Figure 1.4:** STM working principle

For small gaps, an electric current starts to flow. The magnitude of the current is extremely sensitive to the separation distance. As a result, the STM can be used to image individual atoms. Stroscio and Eigler demonstrated for the first time in 1991 that the STM can also be used to manipulate atoms [21]. A pulse voltage applied via an STM tip was used

to move and place $Xe$ atoms onto an orderly patterned structure in Ultra High Vacuum (UHV) (Figure 1.5). This technique was demonstrated using different combinations of materials. Atom manipulation requires UHV and a low temperature environment. The main drawback of an STM is that it can only be used for conductive samples. As a result of the need for a more versatile microscope, the AFM was invented by Binnig et al. [22]. The AFM is in fact able to image conductive and non-conductive samples in UHV and ambient conditions.
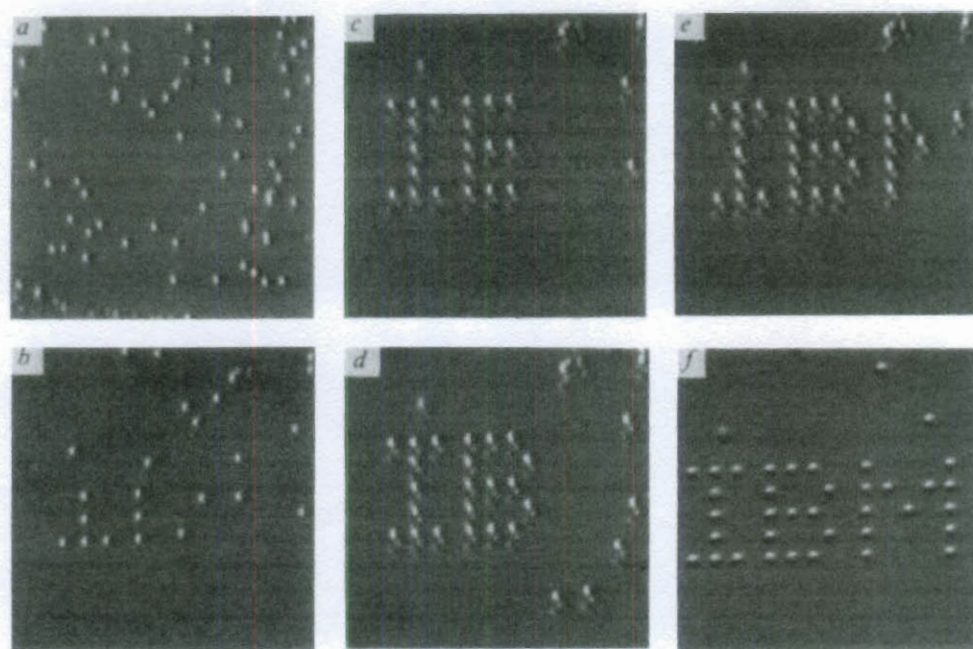


**Figure 1.5:** First STM-based manipulation conducted by Stroscio and Eigler

## 1.3.2    AFM-Based Nanomanipulation

The main element of an Atomic Force Microscope (AFM) is a probe that is scanned over a sample. A typical AFM probe consists of a micro-cantilever with a sharp perpendicular diamond-based tip at its free-end as shown in Figure 1.6 taken with a Scanning Electron

Microscope (SEM) at Rice University.
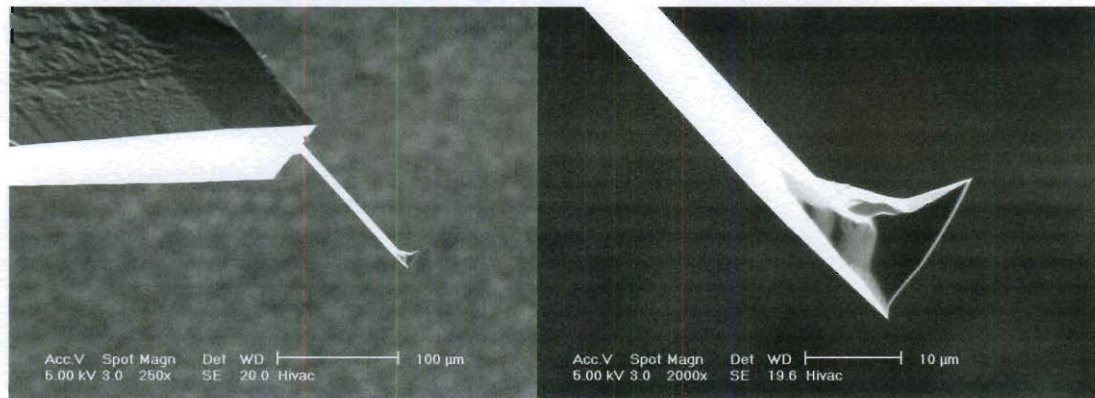


**Figure 1.6:** SEM image of an AFM probe

The deflection of the cantilever, resulting from the atomic force interactions, is monitored using photodetection techniques. A piezotube is generally employed to adjust the relative position between probe and sample (Figure 1.7). Using this setup, images with atomic resolution can be obtained under certain conditions.
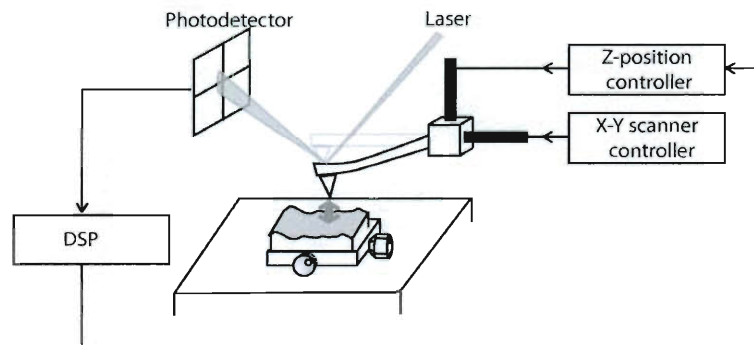


**Figure 1.7:** AFM working principle

Besides its original use as a high resolution microscope, the AFM is evolving into a nanomanipulation tool. Shortly after its invention, it was realized that the AFM cantilever can be used to push and position particles at the nanoscale. The first nano-pushing

experiment using an AFM cantilever reported in the literature was achieved by Shaffer et al. [23] in 1995. Nanometer-size *Au* clusters deposited on atomically smooth substrates were arranged according to predefined patterns at room temperature. Several groups demonstrated successful pushing of different spherical samples (*Au, Ag, GaAs...*) with diameters ranging from $20nm$ to $100nm$ [24, 25, 26, 27, 28]. Pushing nano-particles onto other particles and over steps using an AFM cantilever were also investigated [29, 30]. Falvo et al. [16, 17] used an AFM probe to push CNTs and study their frictional properties. Recent progress includes the use of the AFM along with haptic devices to manipulate samples at the nanoscale and gather feedback information about the fabrication process [31, 32, 33, 34]. Postma et al. [35] constructed Single Electron Transistors (SETs) by pushing and inducing local barriers in a CNT. Repeatable and controllable fabrication of SETs will revolutionize the information and communication industries. Despite these promising results, AFM-based nanomanipulation is still challenging and suffers a lack of repeatability and ease of maneuverability.

## 1.4 AFM-Based Nanomanipulation: Challenges and Limitations

Current implementations of AFM-based nanomanipulation suffer from two major issues. The first one is related to the complexity of the relevant physics and mechanics at the nanoscale. The second shortcoming is the lack of controlled maneuverability of the AFM probe and its tip.

### 1.4.1 AFM Probe and Sample Interaction

As the size of interacting bodies and the corresponding separating distances decrease, surface forces become more significant. These forces play a major role in the manufacturability, operating performance, and reliability of micro and nanoscale systems. Due

to their structural design, nanoscale entities have large surface-to-volume ratios and as a result are highly susceptible to surface forces. This dimension dependence has important consequences on the dynamics of nanoscale objects in contact and non-contact configurations. The most important surface forces acting during manipulation include frictional forces, and tip-sample interactions (adhesion and intermolecular interactions).

**Frictional Forces**: The laws of nano-friction differ drastically from those of macroscopic friction. For instance, friction at the nanoscale has a non-trivial velocity dependence in contrast with its macroscale counterpart [36]. Recent experiments have made important contributions to our understanding of the atomic scale friction, both qualitatively and quantitatively [37]. With the introduction of the Friction Force Microscope (FFM), it became possible to produce a single asperity contact and study friction at the atomic scale [38]. The main result confirmed by several experiments [39, 40, 41, 42] is that the friction force at the nanometer scale exhibits a sawtooth behavior commonly known as atomic stick-slip. The stick-slip behavior can lead to a zigzag motion of the end-effector during manipulation. Better understanding of friction at the atomic scale will enable the design of more sophisticated control to compensate it and thus tracking more accurately desired trajectories.

**Tip-Sample Interactions**: In addition to accurate nano-friction modeling, a deep understanding of the tip-sample interactions is required to improve the repeatability of the manipulation. Adhesion and intermolecular interactions are very versatile in the way the same force can have different effects at short and long range [43]. In the field of nanomanipulation, short range refers to distances close to molecular contacts while long range is around 100 nm. Furthermore, the interaction forces involved during nanomanipulation are both attractive and repulsive. Under proper electrical grounding and UHV conditions, the van der Waals forces are the dominant intermolecular interactions. Transitions from contact and non-contact phases between the tip and sample involve a change in the characteristics of these interactions.

## 1.4.2   Probe Maneuverability

Another major shortcoming of current AFM-based nanomanipulators is the inability of the tip to describe controlled paths and to manipulate relatively large and sticky samples. In fact, the majority of AFM probes are made of $Si$ using semiconductor techniques. These passive cantilevers have a predefined stiffness that cannot be tuned in-situ. Standard AFM systems suffer also related problems leading to small working areas and low operating speeds. Indeed, the positioning systems used in AFMs cannot induce fast and accurate local motion of the tip required to achieve basic nano-fabrication tasks. In addition, the lack of simultaneous real time feedback on the tip and sample motions, during pushing manipulation for instance, imposes real constraints on the operation. In offline AFM-based nanomanipulation, every single operation is carried out based on a static AFM image [13, 29]. This procedure is time consuming and does not allow intermediate control to improve the manipulation accuracy. To address this problem, AFM-based nanomanipulation combined with haptic techniques were proposed [34, 44]. A virtual reality interface was used to help the operator. However, the majority of these models display a static virtual environment and a dynamic tip position. Thus, an accurate model that can calculate the real-time changes of the environment and the tip-sample contact is a must have.

## 1.4.3   Existing AFM-Based Nanomanipulation Models

Researchers have proposed models for AFM-based nanomanipulation [45, 46, 27]. Most of these models manage to represent steady sliding of the manipulated object that is commonly observed in macromanipulation. They are not able, however, to reproduce the stick-slip characteristic of nano-friction. This is mainly due to the use of conventional static friction models such as discretized friction cone models. Although some other researchers managed to construct continuous static friction models that explain nano-friction phenomena [47, 48, 49], static friction models still have inherent shortcomings such as the inability to account for the pre-sliding condition [50], the improper assumption of rapid relaxation

processes in the lubrication film [51], and the undesired creeping sample movement under a nonzero external force. In addition, existing AFM manipulation models either impose very restrictive conditions or make use of momentum analysis to address the tip-sample collision process. But, those approaches are ineffective in describing the complete collision process that may be of interest to study other possible dynamic contact deformation profiles. The dynamic model in [46, 27] does not explain the initial impact characteristics because of the assumption of a constant contact deformation between the tip and the sample during manipulation. Despite the introduction of momentum analysis along with the coefficient of restitution to help estimate the resulting impulse magnitude, the model in [45] remains unable to describe the transient collision process as well. Moreover, both Coulomb switching and momentum analysis require an accurate (and computationally expensive) zero-crossing detection to be well-implemented in numerical simulation. Indeed, the atomic scale friction and the tip-sample interactions affect both sample and nanomanipulator dynamics and should be taken into account for accurate nanomanipulation. Thus, a more insightful understanding of the physics and mechanics involved during manipulation is needed.

In summary, the physics and mechanics of the probe-sample interaction and the maneuverability of the AFM tip remain the main obstacles in fully exploiting AFMs for nanomanipulation.

## 1.5 Motivation and Outline of the Thesis

In this thesis, we propose to advance the area of mechanical nanomanipulation which is defined in this work as *using mechanical forces generated by AFM-type probes to manipulate nanoscale entities in a controlled and repeatable manner in order to produce novel nano-devices and nano-systems.* The present work deals with critically considering the challenges of modeling the physics and mechanics of mechanical probe and sample interactions, and offers new ideas for the design of smart mechanical probes. We use the term

smart to emphasize the active nature of the probe (as opposed to passive) and its ability to generate arbitrary tip trajectories. The main components of a successful Mechanical Nanomanipulator, according to the present research, consist of three main building blocks and their integration:

1. **Building Block 1:** Full consideration of the **mechanics of probe and nano-sample interaction**. This entails detailed consideration of (a) nanoscale friction, (b) tip-sample interaction, and (c) cantilever-sample dynamics.

2. **Building Block 2:** Design and fabrication of **Smart Mechanical Probes**. The probes need to adapt their structural properties in-situ and generate arbitrarily controlled tip trajectories.

3. **Building Block 3: Nanomanipulation**. Integrating Building Block 1 and Building Block 2 to propose effective manipulation schemes at the nanoscale will guarantee accurate and fast nanomanipulation.

Developing Building Blocks 1, 2, and 3 is expected to yield unprecedented repeatability and control of the nanomanipulation processes. In addition, new nanomanipulation schemes exploiting the obtained results will open the door for new possibilities in fabrication and assembly of nano-devices and nano-systems. The remainder of this thesis is organized as follows: Chapter 2 presents an in-depth analysis of the relevant physics and mechanics at the nanoscale including friction force and surface forces interactions. In Chapter 3, we present two new designs of advanced probes suitable for nanomanipulation. The proposed probes allow for simultaneous actuation and sensing of the tip trajectories allowing the implementation of advanced motion control. Next, nanomanipulation schemes exploiting the improved understanding of the nanoscale physics and the advanced capabilities of the proposed end-effectors are presented in Chapter 4. Finally, Chapter 5 includes the conclusions and a discussion of this work.

# Chapter 2

# Mechanics of Probe and Nano-Sample Interaction

The dynamics at the nanoscale are governed by surface forces arising from intermolecular interactions. A typical manipulation task dynamics can be subdivided into three main subsystems: (a) nanoscale friction, (b) tip-sample interaction, and (c) cantilever-sample dynamics (Figure 2.1). These different subsystems are highly coupled due to the nature of the interactions at the nanoscale. Next, we will discuss these subsystems in depth and propose improved modeling suitable for developing nanomanipulation schemes.
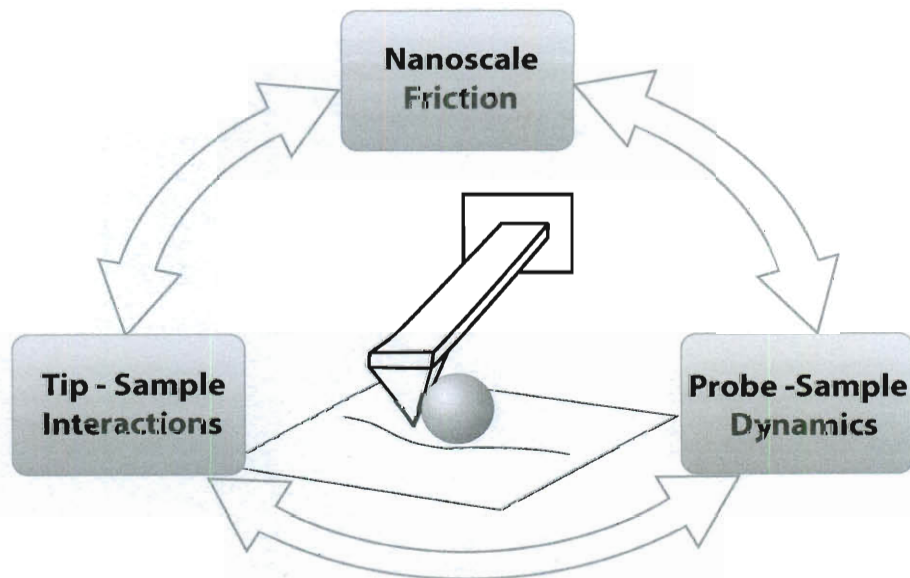


**Figure 2.1:** Mechanics of probe-sample interactions

## 2.1   Nanoscale Friction

With the increasing interest in the miniaturization of moving components and the intro-
duction of the FFM in 1987, the study of friction has acquired a new dimension [52]. It
became possible to study friction at the atomic scale by analyzing single asperity contacts
[53, 54, 55]. Although some similitudes were found, it was revealed by FFM measurements
that the friction laws for a single asperity are different from those at the macroscopic
scale. Nanoscale friction, that we will refer to as nano-friction in the rest of the text,
affects both sample and nanomanipulator dynamics and should be taken into account for
accurate nanomanipulation modeling.

### 2.1.1   Nano-Friction Characteristics

The nano-tribolgical behavior of materials cannot be simply related to their bulk tri-
bological properties due to the different wear and friction processes [36]. FFM experi-
ments showed that the values of the coefficients of friction measured at the nano and the
macroscale are different [52]. In addition, friction at the atomic scale can occur without
wear and is an intrinsic property of the interface [37]. The main characteristic of nano-
friction is a re-occuring stick-slip phenomenon different from its macroscale counterpart
[56, 41, 40, 42]. In fact, the stick-slip behavior at the macroscale is only detected for cer-
tain configurations unlike the sawtooth characteristic of nano-friction that is reproducible
for different kinds of materials and different contact conditions.

In 1987, Mate et al. [57] reported the observation of stick-slip behavior of a tung-
sten tip on graphite samples. After this pioneering work, friction on ionic crystals was
systematically studied by Meyer and coworkers under UHV conditions [58, 59, 60]. These
investigations made possible the detection of the atomic stick-slip behavior on $NaF$, $NaCl$,
$AgBr$ and $KBr$ with standard $Si$ tips. The sawtooth characteristic was also detected on
$Cu(111)$ surface [61] and on the hard diamond (100) and (111) surfaces [62]. Fujisawa et al.
[63, 39] demonstrated through a set of experiments that this phenomenon has a periodicity

correlated with the sample lattice and depends on the direction of the scan. In fact, at low velocities the FFM tip is confined to periodically move and snap on discrete sticking points (Figure 2.2). These jumps can have a zigzag motion and induce a two dimensional (2D) motion of the probe tip. Interestingly, a reverse stick-slip behavior was recently observed for Vertically Aligned Multi-Wall Carbon Nanotubes (VAMWCNTs) [64, 65].
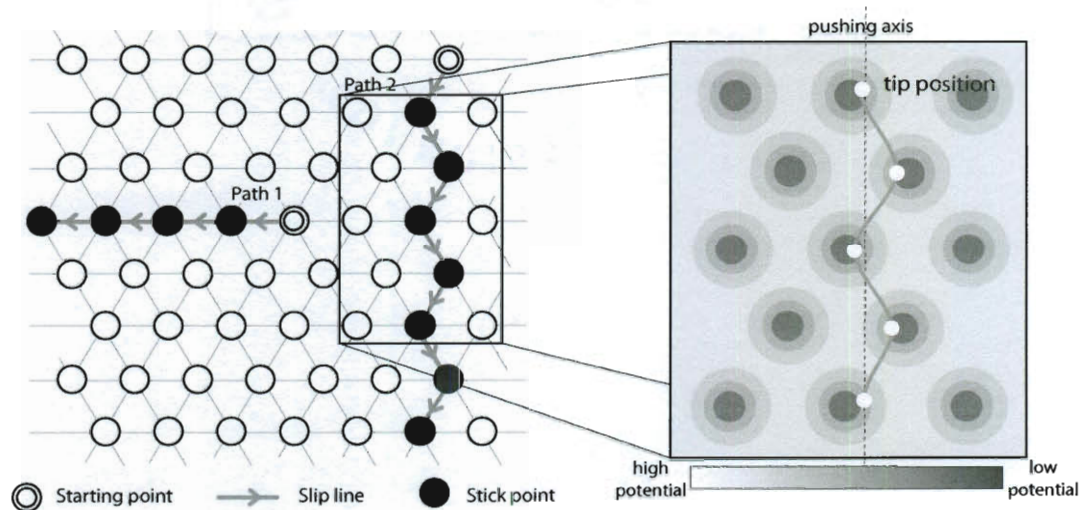


**Figure 2.2:** 2D stick-slip phenomenon

The regular stick-slip characteristic of nano-friction is represented by Figure 2.3-a. Initially, the FFM tip sticks to the neighboring sample atoms because of the attractive interactions. During the scan, the FFM cantilever base is uniformly moved. The cantilever twists as a result of its tip being fixed and base being moved. As long as the lateral force is lower than the force needed to shear the tip-sample junction, the friction force increases linearly with the scanned distance: this phase is called the initial sticking phase. However, at a certain critical force, namely static friction, the junction is broken, the tip instantaneously slips into a new equilibrium position. This process repeats itself periodically during the scan where stick is gradual and slip is abrupt. By measuring the two components of the friction force, Fujisawa and coworkers concluded that the stick points have the periodicity of the substrate. FFM experiments allowed the detection of the zigzag motion

of the tip. Subsequent works [40, 63, 42] reported that this type of motion is dominant at low scan speeds. Recently, Lou and Kim [64] reported a reverse stick-slip pattern for VAMWCNT samples. In fact, for this material stick phases are abrupt and slipping phases are gradual (Figure 2.3-b). The reverse stick-slip behavior is reproducible using both regular FFM tips and cantilever-bead assemblies with and without *Al* coating. Experiments and atomistic simulations revealed a correlation between the surface topography, elastic deformations of CNTs and the shape of this interesting sawtooth behavior [65]. VAMWC-NTs have many potential applications in nanotechnology, including field emission displays and super-capacitors. In addition, their nano-tribological properties make them a material of choice for many nanomanipulation applications [66, 67, 68].
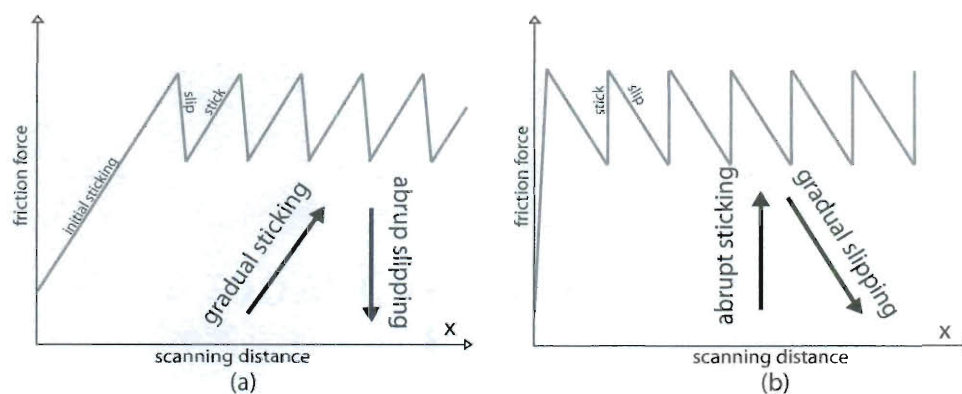


**Figure 2.3:** Stick-slip phenomenon (a) regular (b) reverse characteristics

The most significant impediment to friction modeling at the nanoscale is that the relevant mechanics and physics are very complicated [52]. Nano-friction is highly dependent on the scan velocity [69, 70]. In addition, the physics underlying the sticking and the slipping phases are different [40]. A robust friction compensator is a must have for nanomanipulator path planning. In fact, a continuous nanoscale friction model able to capture the dynamics of the stick-slip phenomenon will allow the design of more accurate nanomanipulation schemes.

## 2.1.2 Review of Nano-Friction Models

A variety of nano friction models are proposed in the nano-tribology literature. These models were developed to reproduce the stick-slip behavior commonly observed during FFM experiments. Stick-slip on the atomic scale has been studied theoretically by various groups. The majority of the proposed models assume that during frictional contact of two bodies, the atoms of the lower body form a periodic energy profile with energy barriers that should be overcome by atoms of the upper body during sliding. It has also been proposed that the stick-slip of two surfaces in relative motion can be modeled as the propagation of a dislocation.

### 2.1.2.1 Interaction potential-based models

This type of models use the notion of potential distribution barriers which originated from the pioneering work of Tomlinson [71]. In 1929, Tomlinson suggested that the dissipation in friction is due to a stick-slip mechanism which can be modeled by assuming a sinusoidal shape for the potential interactions between the two contacting bodies (Figure 2.4). Later, the Tomlinson model was successfully applied to interpret the frictional data of FFM experiments [36].
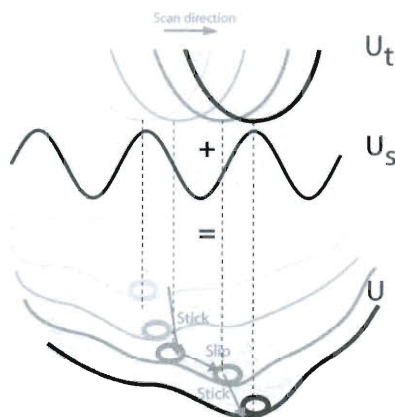


**Figure 2.4:** Potential based interpretation of stick-slip

Two-dimensional Tomlinson friction models were also proposed [72, 73]. Systematic analysis of FFM data aiming to clarify the effects of cantilever stiffness, scan direction and surface topography were conducted [53]. The majority of these models use an adiabatic potential $V(r)$ which has the symmetry of the substrate and rely on a static modeling of the tip-sample system.

### 2.1.2.2 Dislocation-based models

The second family of models proposed in the literature to explain the stick-slip behavior at the nanoscale uses the notion of dislocation propagation [74, 75, 76] (Figure 2.5). According to this type of models, the magnitude of the friction force at the nanoscale is of the same order as the Peierls force needed to move a dislocation on a plane of closed-packed atoms. In the framework of dislocation models, the stick-slip behavior is predicted as a dislocation glide that occurs at multiples of the Burgers vector which represents the magnitude of the lattice distortion caused by a dislocation in a crystal lattice. This is in agreement with FFM experiments that also show a correlation between the stick-slip motion and the lattice of the substrate.
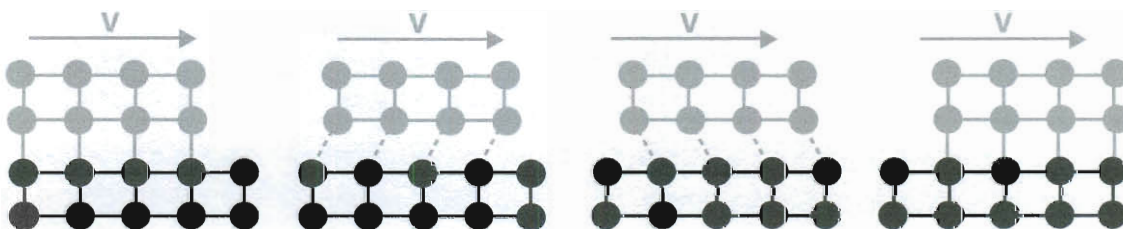


**Figure 2.5:** Dislocation based interpretation of stick-slip

Whether interaction potential based or dislocation based, the majority of the proposed nanoscale stick-slip models rely on a static description of the tip-sample system or are difficult to implement in simulation studies. Recent investigations showed that static considerations alone cannot predict uniquely the properties of the slip events making the aforementioned models not suitable for nanomanipulation modeling purposes [77].

Next, we will review some dynamic friction models from the macro-tribology literature in order to select the best one that can be turned into a nano-friction model reproducing all the dynamic characteristics observed during FFM experiments.

## 2.1.3 Review of Macroscale Friction Models Describing Stick-Slip Behavior

Friction models introducing state variables and able to describe stick-slip motion were proposed in the macro-tribology literature. Some of these models (e.g. Carlson-Batista [78] and Persson [51] models) assume that microscopic forces can be averaged to give rise to global force laws which depend on macroscopic variables only. Thus, these models cannot describe the case of single asperity contact. Other macroscale dynamic friction models can be applied to this limiting case. In the present section, we will review some of these models in order to find a good candidate that can be turned into a nanoscale dynamic friction model.

**Bliman and Sorine Models [79, 80]** Bliman and Sorine have developed a family of dynamic models which can be seen as a generalization of the Dahl model [81]. They defined a new space variable $s$ given by

$$s = \int_0^t |V(\tau)| d\tau. \qquad (2.1)$$

According to the Bliman and Sorine models, the magnitude of the friction force is only a function of $s$ and the sign of the relative sliding velocity $V$. The friction is then a function of the path only. It does not depend on how fast the system moves along the path. In fact, according to their models the friction force depends only on the distance traveled after a velocity zero crossing. Thus, these models cannot be applied to the case of atomic scale friction which depends on the scan velocity. The Bristle model [82] however includes implicitly a velocity dependence.

**Bristle Model [82]** The Bristle Model was introduced by Haessig and Friedland to describe the behavior of the microscopical contact points between two surfaces. The contact points are modeled as flexible bristles which deflect due to the relative motion between the surfaces in contact. The friction force is assumed to be a function of the stiffness of the $N$ contacting bristles according to:

$$F = \sum_{i=1}^{N} \sigma_0(x_i - b_i),$$ (2.2)

where $\sigma_0$ is the stiffness of the bristles, $(x_i - b_i)$ is the difference between the relative position of the bristles $x_i$ and the location $b_i$ where the bond was formed. As this difference equals an upper limit, the bond snaps and a new bristle is formed at a random location relative to the previous one. The Bristle model is a local model that can be applied in the case of one asperity contact. However, it is inefficient in simulations because it introduces a random choice of the deflected bristle and may lead to undesired oscillating behavior for small sliding velocities.

**LuGre Model [83]** The LuGre model is also related to the bristle interpretation of friction. It can be thought of as an extension of the Dahl model to include the Stribeck effect. This effect can be defined as a continuous decrease of the friction force with increasing velocities at the beginning of the relative motion. The state variable $z$, representing the deflection of the bristles, is given by:

$$\frac{dz}{dt} = V - z\frac{|V|}{g(V)},$$ (2.3)

$$g(V) = \frac{1}{\sigma_0}\left[F_c + (F_s - F_c)e^{-(V/V_s)^2}\right].$$ (2.4)

$g(V)$ is introduced to describe the Stribeck effect where $V_s$ is the Stribeck velocity. According to the LuGre model, the friction force is given by:

$$F = \sigma_0 z + \sigma_1\frac{dz}{dt} + F_\nu V,$$ (2.5)

where $\sigma_0$ and $\sigma_1$ are the bristles' stiffness and damping coefficients. $F_s$, $F_c$ and $F_\nu$ represent the static friction, kinetic friction and viscous friction coefficients, respectively.

The LuGre model is flexible with regard to the choice of its different parameters. In addition, the LuGre model is continuous and Lipchitz resulting in a well-posed set of differential equations amenable to analysis and simulation. This friction model includes an explicit dependence on the sliding velocity $V$. As a result, the LuGre model is a good candidate to be turned into a nanoscale friction model. Next, we will modify the LuGre model to be able to reproduce the main characteristics of nano-friction.

## 2.1.4   Our Dynamic Nano-Friction Model

In this section, we will propose a dynamic nano-friction model based on the bristle interpretation of single asperity contacts adopted in the LuGre friction model. Jumping mechanisms will be incorporated in the model to reflect the lattice dependence of the stick-slip behavior at the nanoscale.

### 2.1.4.1   Jumping Mechanism

The 2D stick-slip displacements can be thought of as the result of an additional velocity component $V_{ss}$ or an additional force $F_{ss}$ that tends to move the tip out of the scan axis. These induced driving terms result from the interactions existing between the tip and the sample. Their amplitude and direction vary during time. Thus, additional state variables are needed to describe their dynamics. The tip motion can be divided into sticking and slipping phases. The physics underlying each phase are different. The effect of $V_{ss}$ is negligible when the scan speed $V$ is relatively high as shown in Figure 2.6-c. For relatively low velocities, $V_{ss}$ acts mainly against $V$ during sticking phases (Figure 2.6-a). During slipping phases, $V_{ss}$ behaves as an off-axis term (Figure 2.6-b). In order to implement this jumping criterion it is essential to be able to describe the dynamics of $V_{ss}$ or $F_{ss}$, which is generally difficult to do. A possible simplification is to model the effect of these additional driving terms as a dependence of the friction model on the lattice parameter $a$ and on the angle $\gamma$ between the scan direction and the main sample lattice axis (Figure 2.7).
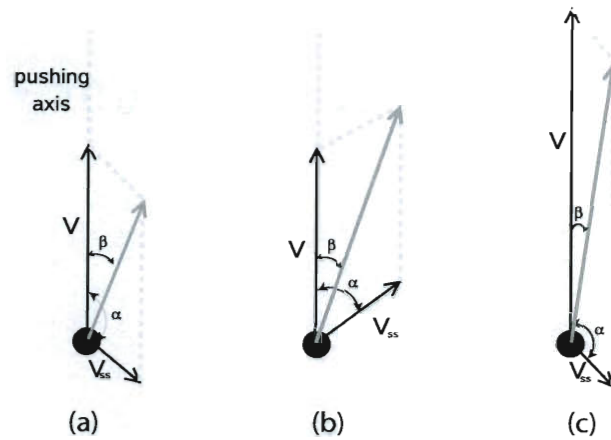
**Figure 2.6:** Jumping criterion based on additional velocity component (a) stick phase (b) slip phase (c) relatively high scan velocity

In fact, during slipping phases the effect of $V_{ss}$ or $F_{ss}$ can be traduced as a dependence of the kinetic friction coefficient on $a$ and $\gamma$. Whereas, this effect during sticking phases will be included through modeling it as a variation in the static and viscous friction terms:

$$F_c = F_c(a, \gamma), \quad F_s = F_s(a, \gamma), \quad F_\nu = F_\nu(a, \gamma). \tag{2.6}$$
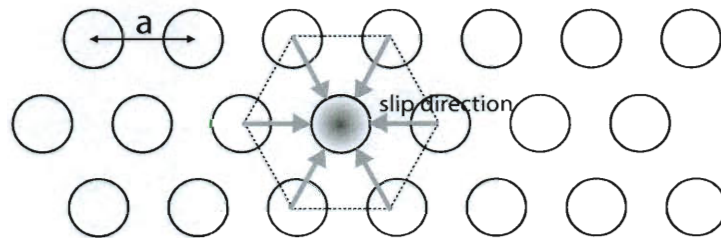


**Figure 2.7:** Jumping directions for an hexagonal lattice

The viscous friction coefficient reflects the damping resulting from the operation in air conditions. However, its contribution to the sawtooth behavior is negligible specially in UHV conditions. As a result, the dynamics of the stick-slip motion are mainly governed

by the periodic transitions between static and kinetic friction regimes reflecting stick and slip phases, respectively. Next, we will present the formulation of our proposed dynamic nano-friction model.

### 2.1.4.2 Proposed Friction Model

According to our proposed nanoscale dynamic friction model, the friction force $F = [ \begin{array}{cc} F_x & F_y \end{array} ]^T$ is given by the following set of equations:

$$F_x = \sigma_{0x} z_x + F_{\nu x}(a) V_x, \tag{2.7}$$

$$\dot{z}_x = \max(V_i)_{i=x,y} - z_x \frac{\|V\|_\infty}{g_x}, \tag{2.8}$$

$$g_x = \frac{1}{\sigma_{0x}} \left[ F_{cx}(a) + (F_{sx}(a) - F_{cx}(a)) e^{-((V_x+V_y)/2V_s)^2} \right], \tag{2.9}$$

$$F_y = \sigma_{0y} z_y + F_{\nu y}(a) V_y, \tag{2.10}$$

$$\dot{z}_y = \max(V_i)_{i=x,y} - z_y \frac{\|V\|_\infty}{g_y}, \tag{2.11}$$

$$g_y = \frac{1}{\sigma_{0y}} \left[ F_{cy}(a) + (F_{sy}(a) - F_{cy}(a)) e^{-((V_x+V_y)/2V_s)^2} \right], \tag{2.12}$$

where $V$ and $V_s$ denote the scan and the Stribeck velocities, respectively. $\sigma_{0x}$ and $\sigma_{0y}$ are the bristle's stiffnesses in the $x$ and $y$ directions. The proposed friction model is based on the dynamics of the LuGre friction model and the bristle interpretation of asperities. However, in the framework of nanoscale friction bristles represent the ultimate single asperity contacts (Figure 2.8). In addition, we introduce the notion of generalized bristle deflection (equation (2.8) and equation (2.11)).

According to the proposed model, the deflection of the bristles in one direction can be the result of a relative velocity in the transverse direction. This reflects the nature of the interactions created by the 2D atom pattern of the sample surface on the probe tip. Furthermore, in order to reflect the effect of sign changes, the Stribeck functions $g_x$ and $g_y$ are calculated using the average of the velocity components instead of the norm of the velocity vector. The coupling between the $x$ and $y$ components of the friction force is achieved through the $g_x$, $g_y$ terms and also the bristle dynamics unlike the Velenis et

al. [84] 2D LuGre friction model where the coupling is only introduced by the $g$ term. The previously discussed jumping mechanism is also included in the formulation of the proposed model.
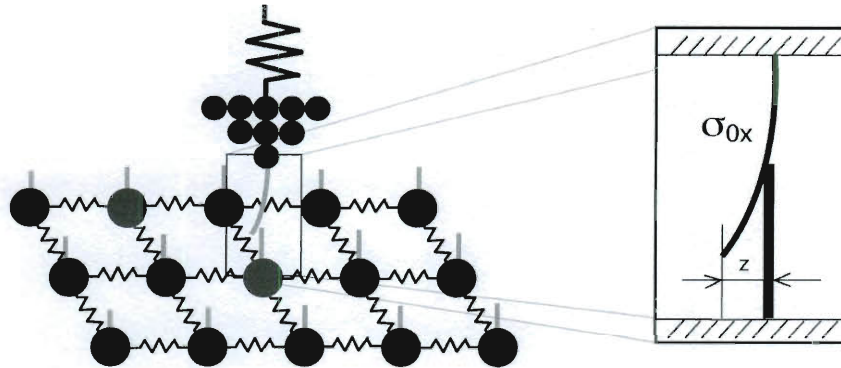


**Figure 2.8:** Bristle interpretation of single asperity contact

Experimental investigations showed that the effect of the angle $\gamma$ on the friction co-efficients is negligible compared to the effect of the lattice parameter $a$. In addition, measuring the angle between the scan direction and the main axis of the sample during FFM experiments is difficult. As a result, the proposed model assumes that $F_s = F_s(a)$ and $F_c = F_c(a)$. The static friction and the kinetic friction coefficients correspond respectively to the highest and lowest values of the periodic portion of the friction curve. In addition, the slope of the initial sticking portion is proportional to the stiffness of the bristles and inversely proportional to the stiffness of the FFM probe. This agrees with experimental observations showing that higher initial sticking and slower transition from sticking to slipping phases are obtained using compliant FFM cantilevers [52]. Atomistic simulations of the friction in VAMWCNTs [65] showed that the interesting reverse stick-slip behavior results from the elastic deformations of the CNTs during the scan. In the framework of the bristle interpretation of single asperity contacts, the nanoscale friction in VAMWCNT arrays can be modeled by stiff bristles (Figure 2.9).
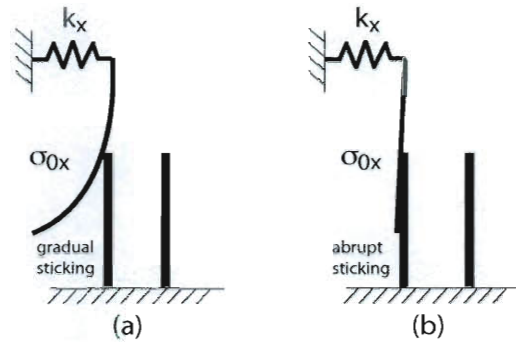
**Figure 2.9:** Effect of the bristles stiffness (a) compliant bristle corresponds to gradual sticking and (b) stiff bristle corresponds to abrupt sticking

The increased stiffness reflects the fact that the bristle base moves and is not fixed as assumed in the previous state equations. The different parameters of the model are material dependent and need to be determined from FFM experiments. The static and kinetic friction $F_{sx}$ and $F_{kx}$ are read directly from the frictional data whereas the bristles' stiffness $\sigma_{0x}$ is chosen such that the slope of the initial sticking phase matches the experimental results. Increased values of $\alpha = \frac{\sigma_{0x}^2}{k_x}$ lead to steeper initial sticking and smoother slipping phases (Figure 2.10). As a result, our model is able to represent both regular and reverse stick-slip characteristics by tuning the parameter $\alpha$.
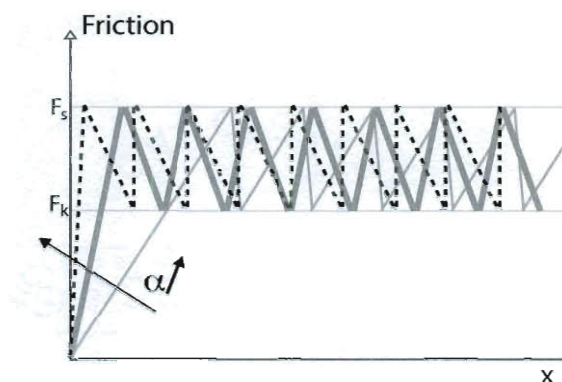


**Figure 2.10:** Transition from regular to reverse stick-slip behavior for increasing values of $\alpha$

In the following section, we will demonstrate the ability of our proposed friction model to reproduce experimentally observed nanoscale friction characteristics.

## 2.1.5  Case Studies

The proposed dynamic friction model will be included into a simplified FFM experiment model. The parameters of the friction model will be obtained from FFM scans. The simulation and experimental results will be compared in order to show the efficacy of the proposed formulation. In an FFM experiment, a sharp tip mounted on a micro-cantilever scans the sample surface at a constant height or normal force [63]. When the tip is moved with respect to the sample, the cantilever undergoes bending and twisting. The motion of the cantilever is controlled using piezoelectric elements that enable high positioning accuracy. The deformations of the cantilever can be measured by detecting the variations in a laser beam reflected from the back of the cantilever (Figure 2.11). The normal and lateral forces acting on the cantilever can be deduced from the normal and lateral signals acquired with the photodetector. The corresponding friction force is calculated from the measured lateral signals. Good measurements require that the FFM cantilever stiffness and the photodetector sensitiveness be known with an adequate precision.
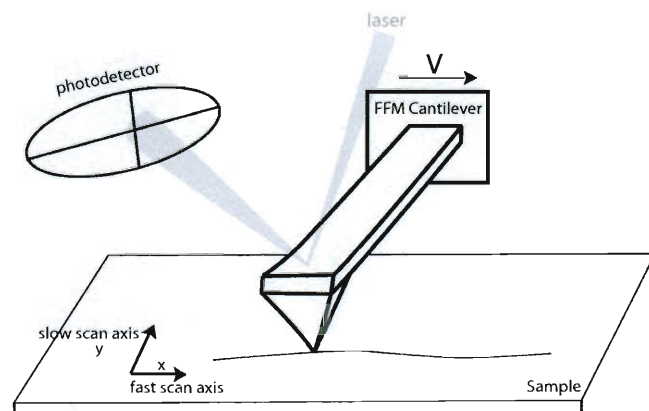


**Figure 2.11:** FFM experiment

The FFM cantilever is modeled as a 2 d.o.f spring and mass system. This model is shown to yield good results especially when the FFM cantilever is excited around its first natural frequency [85]. One advantage of this simple model is that it is independent of the cantilever geometry. The relevant forces involved during scanning the sample surface are the driving force $D = [ \ D_x \quad D_y \ ]^T$, the probe-sample interaction force $I = [ \ I_x \quad I_y \ ]^T$ and the friction force $F = [ \ F_x \quad F_y \ ]^T$. Under proper electrical grounding, the interaction force between the FFM cantilever and the sample can be represented by the Derjaguin interaction model [85]. Using the above assumptions, the FFM cantilever dynamics can be described by:

$$m_x \ddot{x} \ + \ c_x \dot{x} + k_x x = D_x - I_x - F_x, \tag{2.13}$$

$$m_y \ddot{y} \ + \ c_y \dot{y} + k_y y = D_y - I_y - F_y, \tag{2.14}$$

where $m_i$, $c_i$ and $k_i$ $(i = x, y)$ are the corresponding masses, damping and stiffness coefficients. We apply a driving term consisting of a ramped position input in the $x$ direction of the FFM cantilever base with a constant velocity $V$. Thus, $D$ is given by:

$$D_x \ = \ c_x V + k_x V t, \tag{2.15}$$

$$D_y \ = \ F_y - F_{cy}. \tag{2.16}$$

The $D_x$ component, in the pushing direction, is the result of the FFM cantilever base controlled motion. Whereas, the $D_y$ term models the effect of the additional stick-slip velocity component.

### 2.1.5.1  Regular Stick-Slip Behavior: Muscovite Mica

In order to validate the proposed friction model, FFM studies were performed on freshly cleaved Mica sample in ambient conditions. A Pico-plus AFM (Agilent AFMs, Tempe, Arizona) with a silicon probe (Budget sensor, Contact) was used in this study. In-situ calibrations of the AFM probe in both normal and lateral directions were done to convert the voltage output signals to normal and lateral forces experienced by the cantilever during scanning process according to the procedures developed by Lou and Kim [64]. The

experiments were conducted under constant normal load $F_n = 141.75nN$ and the fast scan velocity was set to $V = 2000nm/s$ along the $x$ axis. The scan range is $10nm \times 10nm$ and the obtained image represented by Figure 2.12 is the result of 512 serial scans along the slow scan axis $y$.
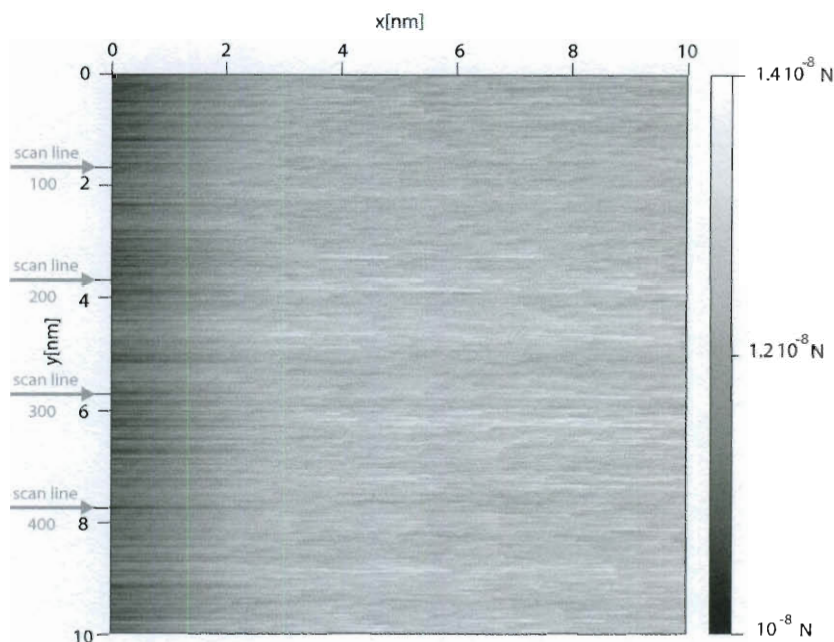


**Figure 2.12:** Experimental frictional data of a Mica sample

The Experimental results exhibit the commonly observed sawtooth characteristic of nanoscale friction. In fact, despite the noise introduced by the experimental conditions, the stick-slip behavior is dominant and easily observed at relatively slow scan speeds. Figure 2.13 represents frictional data corresponding to the four line scans 100, 200, 300 and 400. As it is clear from the aforementioned figure, although the Mica can be cleaved into flat surfaces the effect of the topography cannot be totally eliminated. In order to **determine the different parameters** of the friction model, we consider the scan with the highest initial sticking which is a common practice in FFM experiments. This corresponds to the scan line 179 in our case.
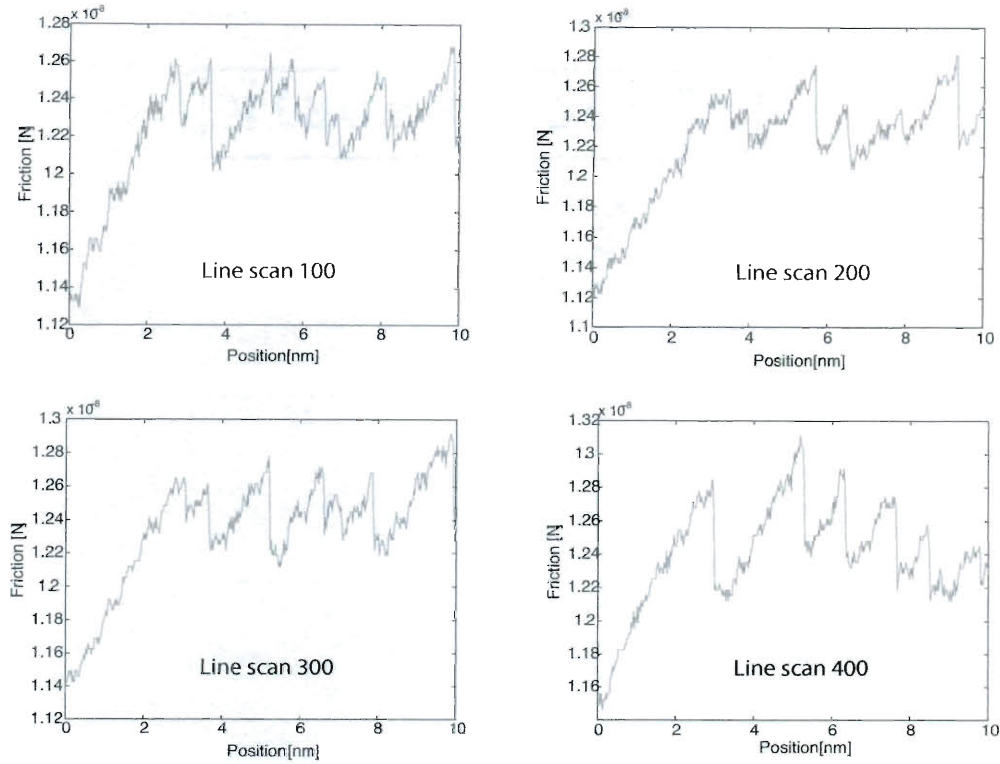
**Figure 2.13:** Four arbitrary scans representing the frictional characteristics of Mica

The static friction is obtained by averaging the highest values of the friction curve and the kinetic friction by averaging the lowest values of the periodic part of the friction curve. The values of the bristle stiffnesses are calculated such that the slope and the initial sticking match the experimental values. The model implementation was realized using the MATLAB solver *ode23tb*. The relative and absolute tolerances of the solver were set to 1e−2 and 1e−15 respectively. The initial conditions including the initial velocities and the initial bristle deflections in the $x$ and $y$ directions were set to zero. The parameters used for the simulation are given in Table 4.4. These include the parameters deduced from the considered scan line and those obtained from the geometrical and material properties of the FFM cantilever. The simulation and experimental results are then superimposed in Figure 2.14.

**Table 2.1:** Mica sample friction model parameters

| PARAMETER | VALUE | PARAMETER | VALUE | PARAMETER | VALUE |
|-----------|-------|-----------|-------|-----------|-------|
| $m_x$ | $1.98e{-}18$ kg | $m_y$ | $1.98e{-}18$ kg | $F_{sx}$ | $12.95e{-}9$ N |
| $c_x$ | $7e{-}9$ N.s/m | $c_y$ | $7e{-}9$N.s/m | $F_{sy}$ | $12.95e{-}9$ N |
| $k_x$ | $0.2$ N/m | $k_y$ | $0.1$N/m | $F_{cx}$ | $12.45e{-}9$ N |
| $\sigma_{0x}$ | $1e4$N/m | $\sigma_{0y}$ | $1e4$N/m | $F_{cy}$ | $12.45e{-}9$ N |
| $V_s$ | $1e{-}5$ m/s | $F_{\mu y}$ | $1e{-}7$ N | $F_{\mu x}$ | $1e{-}7$N |

Figure 2.14 shows clearly that the proposed model succeeded in describing the stick-slip characteristic of nano-friction. Adjusting the different parameters of the model lead to a good agreement with the experimental results.
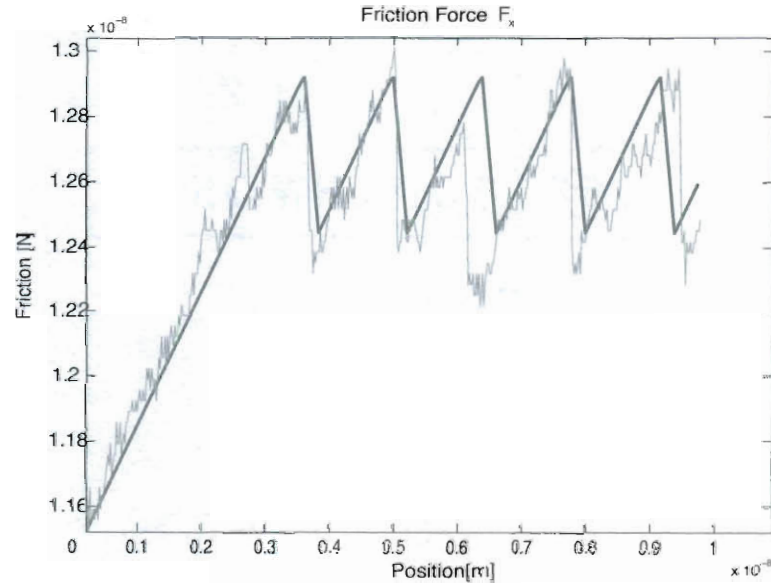


**Figure 2.14:** Simulated versus experimental friction of a Mica sample for one line scan

Next, the ability of our model to represent the reverse stick-slip behavior will be investigated.

### 2.1.5.2 Reverse Stick-Slip behavior: VAMWCNT Array

Highly ordered arrays of Multi-Walled Carbon Nanotubes embedded in a hexagonal close-packed alumina template were grown by Chemical Vapor Deposition (CVD) [64]. The VAMWCNTs are then partially exposed by etching the alumina matrix to desired depth. For the sample used in the present study, VAMCWNT arrays with 30 nm protruded length were prepared (Figure 2.15-a). The diameter of these nanotubes is about $25 \sim 40$ nm with $\sim 50$ nm inter-channel distance.

In order to determine the frictional properties of the VAMWCNT array sample, a borosilicate glass micro-sphere (Duke Scientific Corporation, Diameter of $14.5\mu m \pm 1.0\mu m$) was attached to a regular AFM tip using Devcon 5-Minute Epoxy adhesive. The scan range is $1\mu m \times 1\mu m$ and the obtained image is shown in Figure 2.15-b. The different parameters of the friction model are calculated from the scan with the highest initial sticking which corresponds to the scan line 124 in our case. The deduced simulation parameters are grouped in Table 2.2.



(a)    (b)
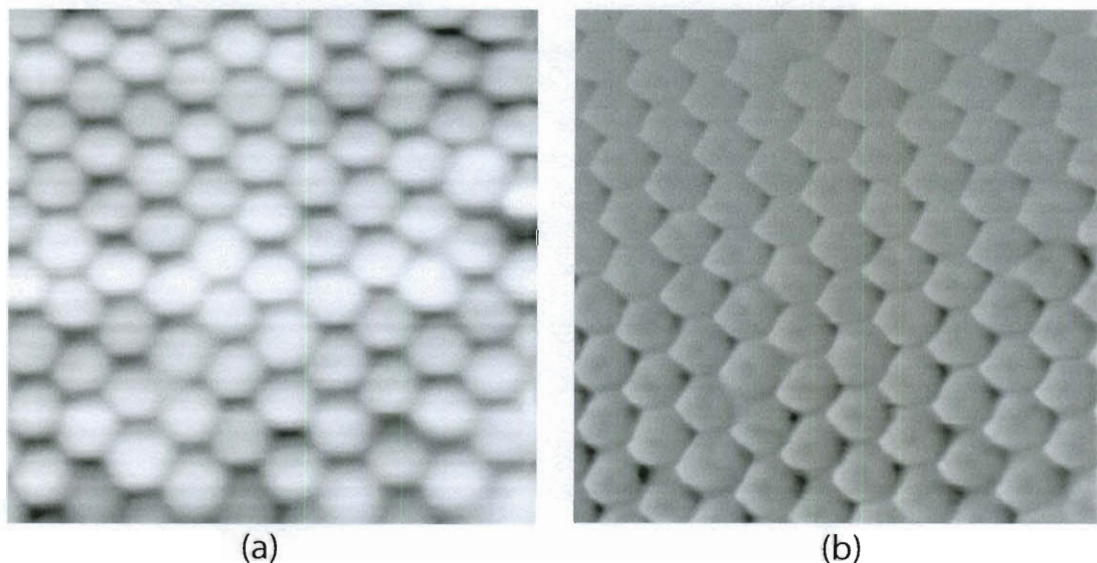
**Figure 2.15:** VAMWCNT sample (a) topography (b) frictional data

Table 2.2: VAMWCNT sample friction model parameters

| Parameter | Value | Parameter | Value | Parameter | Value |
|-----------|-------|-----------|-------|-----------|-------|
| $m_x$ | $2.25e{-}17$ kg | $c_x$ | $7e{-}9$ N.s/m | $k_x$ | $0.1$ N/m |
| $m_y$ | $2.25e{-}17$ kg | $c_y$ | $7e{-}9$ N.s/m | $k_y$ | $0.05$ N/m |
| $F_{si}$ | $1.5e{-}7$ N | $F_{ki}$ | $0.6e{-}7$ N | $F_{\nu i}$ | $1e{-}7$ N.s/m |
| $\sigma_{0x}$ | $3e^5$ N/m | $\sigma_{0y}$ | $3e^5$ N/m | $V_s$ | $1e{-}5$ m/s |

The Experimental results exhibit a reverse stick-slip characteristic (Figure 2.16). Despite the noise introduced by the experimental conditions, the stick-slip behavior is dominant and easily observed at relatively slow scan speeds. It is clear from Figure 2.16 that the proposed model succeeded in capturing the main features of the reverse stick-slip characteristic of the VAMWCNT sample. Adjusting the different parameters of the model lead to acceptable agreement with the experimental results.
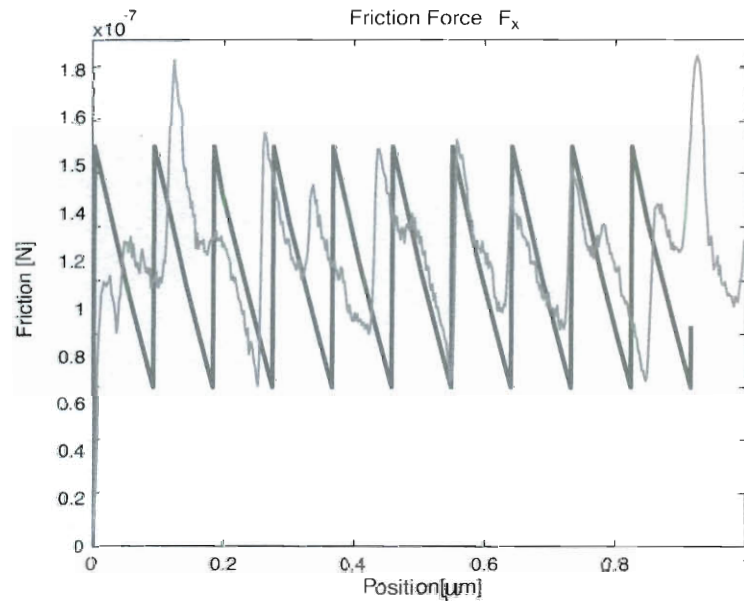


Figure 2.16: Simulated versus experimental one line FFM scan of a VAMWCNT sample

Next, we will adopt an improved modeling of the relevant tip-sample interactions. In addition, we will investigate the coupling between the interactions and the friction at the nanoscale.

## 2.2  Tip-Sample Interaction

Interaction forces between the sample and the probe's tip can be attractive or repulsive depending on different proximity conditions. Many nanomanipulation models proposed in the literature adopt restrictive initial contact conditions and thus cannot describe the complete tip-sample collision process [46, 27]. A deeper understanding of the tip-sample interactions during nanomanipulation is needed.

### 2.2.1  Intermolecular Interactions

At the macroscale, volume forces form the major contribution to the interaction between bodies. For instance, gravity is the determinant factor of the interactions between planets. The contribution of surface forces can be generally neglected for large scales. As the size of the interacting bodies and the separating distances decrease, surface forces become more significant. This dimension dependence has important consequences on the dynamics of bodies during nanomanipulation. At the nanoscale, volume forces can be neglected with respect to intermolecular surface forces. These intermolecular interactions are very versatile in the way the same force has different effects at short and long range [43]. In the field of nanomanipulation, short range refers to distances close to molecular contacts while long range is around 100 nm. Under proper electrical grounding and UHV, the van der Waals forces are the dominant intermolecular interactions.

The van der Waals forces consist of dipole-dipole, dipole-non polar and non polar-non polar interactions. Those three types of interactions are known as Keesom, Debye, and London interactions, respectively (Figure 2.17). The London dispersion interaction is mostly responsible for the entire van der Waals interaction although the Keesom interaction

becomes considerable or even greater than the London's in highly polar molecules such as water. Each van der Waals interaction is proportionally related to its corresponding Hamaker's constant [43]. The theoretical interaction energy of each type of van der Waals forces is respectively given by:

$$E_K(r) = -\frac{u_1^2 u_2^2}{3(4\pi\epsilon_0)^2 kTr^6},$$ (2.17)

$$E_D(r) = -\frac{u^2\alpha}{(4\pi\epsilon_0)^2 r^6},$$ (2.18)

$$E_L(r) = -\frac{3}{4}\frac{h\nu\alpha^2}{(4\pi\epsilon_0)^2 r^6},$$ (2.19)

where $\epsilon_0$, $k$, $T$, $\nu$, $\alpha$, $u$ represent the permittivity constant, the Boltzman constant, the Planck's constant, the temperature, the electronic absorption frequency, the polarizability constant and the dipole moment, respectively.
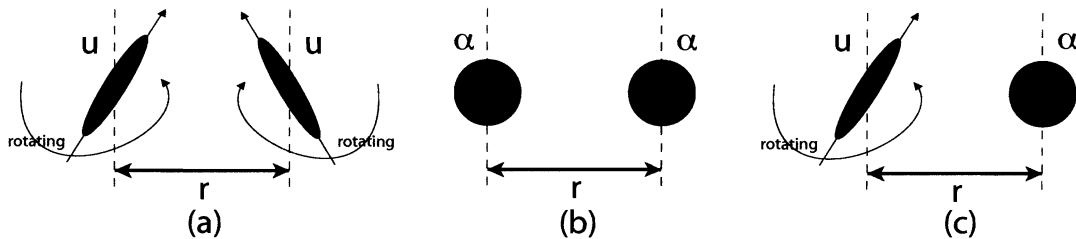


**Figure 2.17:** Van der Waals interactions (a) Keesom (b) London (c) Debye

Generally, van der Waals forces between identical molecules across any medium are attractive. On the other hand, dissimilar molecules may experience either attractive or repulsive interactions depending on the nature of the intermediate medium. In the case of AFM-based manipulation, beside attractive forces, the probe and sample may experience a repulsive force as they press against each other that results in a contact deformation. Since the tip and the sample are made of many atoms, contact models that take into account the superposition of the van der Waals forces are needed.

## 2.2.2 Nanoscale Contact Models

Several theories have been proposed to model the interactions between systems at micro and nanoscale. At the nanoscale, the effects of adhesion cannot be neglected. The Derjaguin-Muller-Toporov (DMT) [86] and the Johnson-Kendall-Roberts (JKR) [85] models are examples of classical contact models that were successfully applied to describe interactions at the nanoscale.

### 2.2.2.1 Derjaguin-Muller-Toporov (DMT) Contact Model

This model applies to low adhesion systems. The tip-sample geometry is constrained to remain Hertzian. In other words, the DMT model corresponds to an Hertz interaction model with an offset due to surface forces. The model does not consider hysteresis between loading and unloading but it accounts for long-ranged attraction around the periphery of the contact area (Figure 2.18-a). It is assumed that the deformed geometry can be given by the Hertz problem solution. One shortcoming of this model is that it underestimates the true contact area. According to the DMT model, the interaction force takes the following form:

$$F = \begin{cases} \frac{-HR}{6(x_s-(R_s+R_t))^2} & if \ (x_s-(R_s+R_t)) \geq \zeta_0, \\ \frac{-HR}{6\zeta_0^2} + \frac{4E^*\sqrt{R}(\zeta-(x_s-(R_s+R_t)))^{3/2}}{3} & if \ (x_s-(R_s+R_t)) \leq \zeta_0, \end{cases} \tag{2.20}$$

where $H$ is the Hamaker's constant [43] and $\zeta_0$ is the inter-atomic separation distance introduced in [87] to avoid numerical divergence of the interaction forces. The effective tip-sample elastic modulus $E^*$ and the reduced tip-sample curvature $R$ are given by:

$$E^* = \left[\frac{1-\nu_t^2}{E_t} + \frac{1-\nu_s^2}{E_s}\right]^{-1} \quad ; \quad R = \left[\frac{1}{R_t} + \frac{1}{R_s}\right]^{-1}, \tag{2.21}$$

where $\nu_t$, $\nu_s$, $E_t$, $E_s$, $R_t$ and $R_s$ are the Poisson ratios, the elastic moduli and the radii of the tip and the sample, respectively.

### 2.2.2.2 Johnson-Kendall-Roberts (JKR) Contact Model

In the JKR analysis, short-ranged attractive forces are considered to operate within the contact area. The model accounts only for the influence of van der Waals forces within

the contact zone (Figure 2.18-b). The tip-sample geometry is not constrained to remain Hertzian. Thus, JKR is well suited for strongly adhesive systems. In addition, the model assumes that there are no forces between the surfaces when they are not in contact, upon contact short-ranged attractive forces suddenly operate within the contact area. The corresponding interaction force can be expressed by:

$$
F = \begin{cases} fR\left[\frac{-\sigma^2}{(x_s-(R_s+R_t))^2} + \frac{\sigma^8}{30(x_s-(R_s+R_t))^8}\right] & if\ (x_s-(R_s+R_t)) \geq z_0, \\ \frac{8}{3}E^*\sqrt{2R}(z_0-(x_s-(R_s+R_t)))^{(3/2)} & if\ (x_s-(R_s+R_t)) \leq z_0, \end{cases} \quad (2.22)
$$

where $z_0$ is the zero point of the Lennard-Jones potential and $\sigma$ is the spherical approximation of the molecule diameter [86].



DMT

JKR

(a)                                           (b)
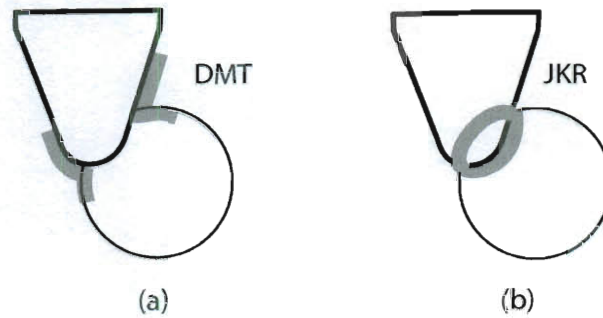
**Figure 2.18:** Domain of action of surface forces according to the (a) DMT and (b) JKR models

The AFM operation falls into the transition zone between the DMT and JKR adhesion regimes [88], for which Maugis [89] provided a good analysis. In fact, The MD theory can be seen as a continuous transition between the DMT and the JKR models. In the adopted interaction model, presented in the next section, the MD formulation will be used to describe contact phases during manipulation.

## 2.2.3   Adopted Tip-Sample Interaction Model

Assuming that the manipulation is conducted in UHV with proper electrical grounding, the significant interactions between the tip and sample during non-contact phases result from

the attractive van der Waals forces. The corresponding attraction force can be written in the form [87]:

$$I_{nc} = \frac{-HR}{6(d - \zeta_0)^2},$$ (2.23)

where $H$ and $R$ are the Hamaker constant and the effective system radius, respectively. The parameter $\zeta_0$ is the inter-atomic distance introduced to prevent the singularity of the attraction force [87] and $d$ is the separation distance. Taking into account the attractive van der Waals forces will allow the description of the jump-into contact phenomenon through the use of non-contact initial configurations.

We propose that the contact phase between the AFM tip and the sample be described using the MD contact mechanics. This choice is motivated by the fact that the aforementioned model approximates well both cases of strong and weak adhesion. Thus, it is able to model a wide range of AFM-based nanomanipulation experiments. The MD contact model introduces a non-dimensional transition parameter $\lambda$ given by [89]:

$$\lambda = \frac{2.06}{\zeta_0} \left( \frac{W^2 R}{\pi K^2} \right)^{1/3},$$ (2.24)

where $W$ represents the work of adhesion and $K$ is the elastic modulus of the tip-sample system. Large values of $\lambda$ correspond to large contact radii and small adhesion contacts, while small values are for small contact radii with high adhesion. The MD model can be seen as a continuous transition from DMT ($\lambda = 0$) to JKR ($\lambda = \infty$) contact models (Figure 2.19). The non-dimensional equations defining the model are given by [89]:

$$1 = \frac{\lambda \bar{A}^2}{2} \left[ \sqrt{m^2 - 1} + (m^2 - 2)atan(\sqrt{m^2 - 1}) \right]$$
$$+ \frac{4\lambda^2 \bar{A}}{3} \left[ 1 - m + \sqrt{m^2 - 1}atan(\sqrt{m^2 - 1}) \right],$$ (2.25)

$$\bar{\Delta} = \bar{A}^2 - \frac{4\lambda}{3}\sqrt{m^2 - 1},$$ (2.26)

$$\bar{I}_c = \bar{A}^3 - \lambda \bar{A}^2 \left[ \sqrt{m^2 - 1} + m^2 atan(m^2 - 1) \right],$$ (2.27)

where $\bar{A}$, $\bar{\Delta}$ and $\bar{I}_c$ are the non-dimensional contact radius, penetration depth and contact load, respectively.

The corresponding dimensionalized variables can be obtained using:

$$A = \left(\frac{\pi W R^2}{K}\right)^{1/3} \bar{A}, \tag{2.28}$$

$$I_c = \pi W R \bar{I}_c, \tag{2.29}$$

$$\Delta = \left(\frac{\pi^2 W^2 R}{k^2}\right)^{1/3} \bar{\Delta}. \tag{2.30}$$

The parameter $m$ represents the ratio of the annular region width to the radius of the contact area. In order to obtain the contact force, equations (2.25) and (2.26) can be solved simultaneously for a given value of $\lambda$ and $\bar{\Delta}$. The obtained value of $m$ and $\bar{A}$ are then substituted into equation (2.27) to determine $\bar{I}_c$.
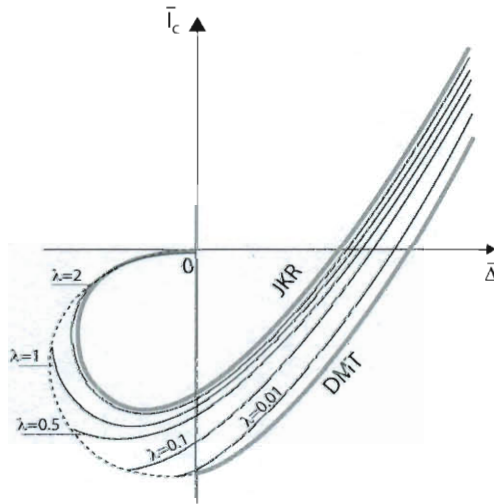


**Figure 2.19:** Relation between $\bar{I}_c$ and $\bar{\Delta}$ for various $\lambda$

The transition from non-contact to contact is very important. In fact, the corresponding interaction forces must be continuous. Maugis [89] showed that when $\bar{A} \rightarrow 0$ and $m \rightarrow \infty$, we have:

$$\bar{I}_c = \bar{I}_0 = -2 + \frac{8\lambda(\pi-2)^2}{9\pi}\left[\sqrt{4\lambda^4 + \frac{9\pi\lambda}{(\pi-2)^2}} - 2\lambda^2\right], \tag{2.31}$$

$$\bar{\Delta} = \bar{\Delta}_0 = -\frac{8(\pi-2)}{9\pi}\left[\sqrt{4\lambda^4 + \frac{9\pi\lambda}{(\pi-2)^2}} - 2\lambda^2\right]. \tag{2.32}$$

Thus in order to assure continuity, we propose that the attraction force during non-contact phases be given by:

$$\bar{I}_{nc} = \frac{-\bar{I}_0(\bar{\Delta}_0 - \bar{\zeta}_0)^2}{(\bar{\Delta} - \bar{\zeta}_0)^2}.$$ (2.33)

As a result, the complete non-dimensional interaction model can be written as:

$$\bar{I} = \begin{cases} -\bar{I}_c & for \ \bar{\Delta} < \bar{\zeta}_0, \\ \frac{-\bar{I}_0(\bar{\Delta}_0 - \bar{\zeta}_0)^2}{(\bar{\Delta} - \bar{\zeta}_0)^2} & for \ \bar{\Delta} > \bar{\zeta}_0, \end{cases}$$ (2.34)

and the corresponding dimensional interaction force obtained using:

$$I = \pi W R \bar{I}.$$ (2.35)

It is well known from experimental investigations that many parameters affect the nature of the interactions during AFM-based nanomanipulation. Some of these parameters are the tip and sample geometries and the stiffness of the AFM cantilever. The adopted interaction model includes those effects through the $H$, $K$ and $R$ terms. In addition, higher tip-sample adhesion is expected to affect their relative motion and lead to higher friction. In the next section, we will investigate the coupling between the adhesion and nano-friction based on the adopted modeling. The simulation results are expected to improve our understanding of the physics and dynamics at the nanoscale.

## 2.2.4    Adhesion-Friction Coupling at the Nanoscale

In order to investigate the coupling between the adhesion and the friction, a line scan of the FFM experiment will be simulated for different values of the adhesion between the tip and sample surface. Different values of adhesion correspond to different values of $\lambda$ in the adopted interaction model. However in order to isolate the effect of the adhesion, it is essential to use the same effective radius when comparing the results of these simulations. Figure 2.20 shows two simulated FFM scans of the same region of a Muscouvite Mica sample corresponding to two different values of the tip radius, namely $R_t = 100nm$ and $R_t = 200nm$.
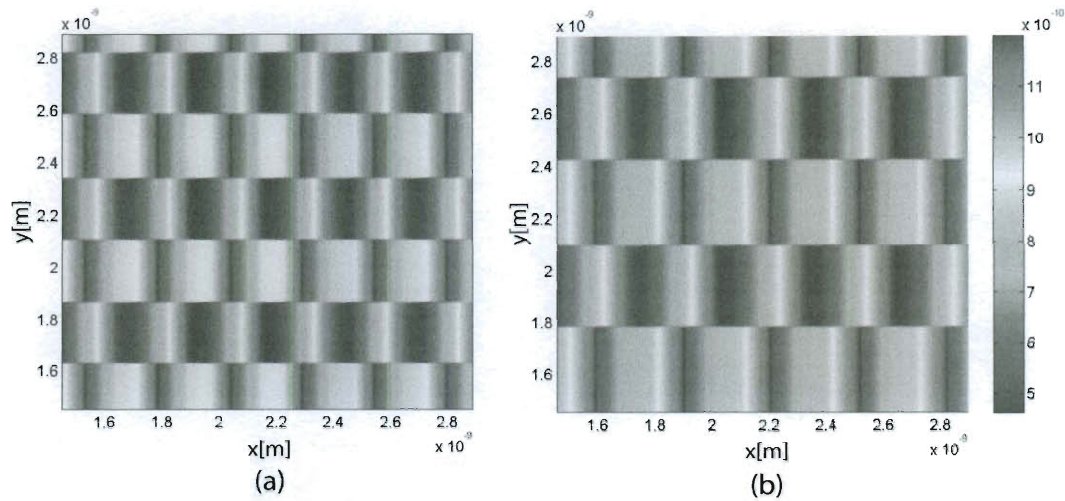
**Figure 2.20:** Simulated FFM image of a sample for (a) $R_t = 100$ nm and (b) $R_t = 200$ nm

Clearly, varying the value of the tip radius leads to a change in the size of the pattern forming the FFM image. This behavior is referred to as the convolution phenomenon [24] where for non-sharp tips more topographic details are missed (Figure 2.21). In order to avoid the convolution phenomenon, the value of the tip radius will be unchanged when comparing the friction characteristics for different values of $\lambda$.
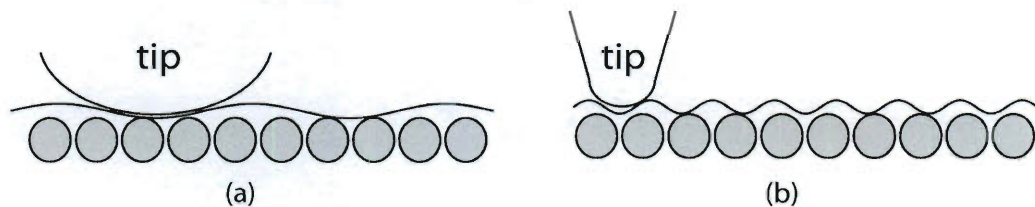


**Figure 2.21:** Convolution effect (a) large tip radius (b) small tip radius

A line scan of an FFM experiment was simulated for different values of $\lambda$ ranging from 0 to $\infty$. The resulting friction plots are shown in Figure 2.22. The model predicts the sawtooth characteristic of nano-friction for all values of $\lambda$. The frictional data present a sawtooth shape where the friction oscillates periodically between the static and the kinetic

friction values. The periodicity of the pattern is correlated with the periodicity of the substrate lattice. For very low tip-sample adhesion, the sticking positions correspond to the minima of the potential distribution created by the atoms of the substrate. However, as $\lambda$ is increased the pattern is shifted and the initial sticking values are increased. Moreover, higher adhesion values correspond to larger periods of the sawtooth characteristic.
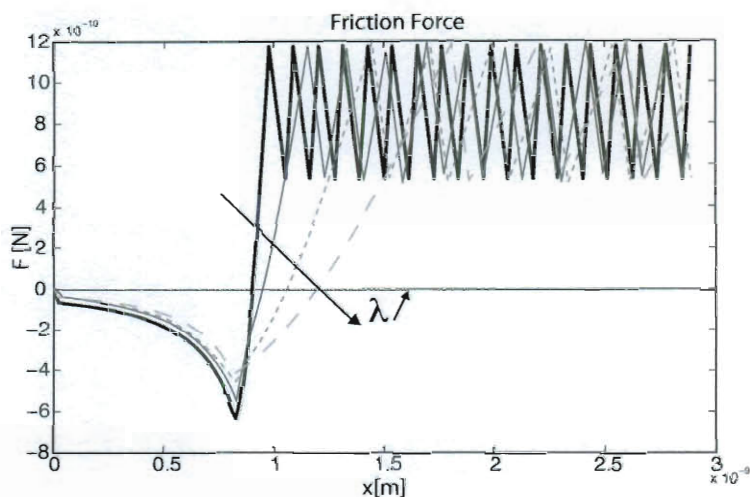


**Figure 2.22:** Effect of adhesion on nanoscale friction

The results of the simulations demonstrate that the different nanoscale interactions are highly coupled. A proper choice of the probe material is essential to improve the manipulation of different types of samples. In addition, the probe-sample dynamic modeling needs to take those physics into account to predict accurately the sample motion.

## 2.3 Cantilever-Sample Dynamics

There are two major techniques used to model AFM probes. The first one treats the cantilever as a continuous system. External forces acting on the cantilever are prescribed in the appropriate boundary conditions. The second approach considers the cantilever as a point mass with properties directly derived from the first vibration mode. External

forces are assumed to be applied to the point mass. This technique corresponds practically to using a lumped parameter representation of the continuous structure. This section is not meant to be extensive, many comparative works between distributed and lumped-parameter modeling techniques can be found in the literature [90].

### 2.3.1 Distributed Parameter Model

In this model, the probe is treated as a continuous medium interacting with the sample on its free-end. The continuous model theoretically considers infinite harmonics of the cantilever vibrations. The flexural vibrations of a cantilever beam are governed by:

$$\frac{\partial^2 M(x,t)}{\partial x^2} = -m_x(x)dx\frac{\partial^2 y(x,t)}{\partial t^2}, \tag{2.36}$$

where $M$, the flexural moment, is defined by:

$$M(x,t) = EI(x)\frac{\partial^2 y(x,t)}{\partial x^2}. \tag{2.37}$$

Substituting equation (2.37) into equation (2.36), the resulting governing equation of the probe motion is given by:

$$\frac{\partial^2}{\partial x^2}\left[EI(x)\frac{\partial^2 y(x,t)}{\partial x^2}\right] = -m_x\frac{\partial^2 y(x,t)}{\partial t^2}, \tag{2.38}$$

where $E$ is the cantilever elastic modulus, $I(x)$ the cantilever moment of inertia and $m_x(x)$ the mass per unit length. The equation is subjected to two initial conditions and the following four BCs:

$$\begin{cases} y(0,t) = 0, \\ \dot{y}(0,t) = 0, \\ \ddot{y}(L,t) = 0, \\ \dddot{y}(L,t) = 0. \end{cases}$$

The method of separation of variables can be used to solve equation (2.38). The cantilever modeshapes can be expressed by [91]:

$$Y(x) = \sum_{r=1}^{\infty} c_0\left[(\cos\beta_r x - \cosh\beta_r x) - \frac{\cosh\beta_r L + \cos\beta_r L}{\sinh\beta_r L + \sin\beta_r L}(\sin\beta_r x - \sinh\beta_r x)\right]. \tag{2.39}$$

$\beta_r$ satisfies the following condition:

$$\cosh \beta_r L \cos \beta_r L + 1 = 0, \tag{2.40}$$

and is related to the natural frequency of the cantilever through $\beta_r^4 = \frac{\omega_{n,r}^2 m_x}{EI}$. The first harmonic of the vibration of a cantilever with a uniform cross-section is found to be [92]:

$$\omega_{n,1} = \sqrt{\frac{1.875^4}{3} \frac{3EI}{(m_x L)L^3}} = \sqrt{\frac{1.875^4}{3} \frac{3EI}{mL^3}}, \tag{2.41}$$

In addition, the cantilever effective bending spring stiffnesses due to normal force and bending moment can be defined by $k_f = \frac{3EI}{L^3}$ and $k_m = \frac{2EI}{L^3}$, respectively.

Rayleigh's method can also be used to obtain an estimate of the first natural frequency [93]. The method is very useful for a continuous system with varying cross sectional area, density, or elastic modulus. Rayleigh method is based on energy considerations leading to $T_{max} = V_{max}$ for conservative systems [92]. In the case of flexural vibrations of a cantilever, the kinetic and potential energies are defined by:

$$T(t) = \frac{1}{2} \int_0^L m_x(x) \left[ \frac{\partial y(x,t)}{\partial t} \right]^2 dx, \tag{2.42}$$

$$V(t) = \frac{1}{2} \int_0^L EI(x) \left[ \frac{\partial y(x,t)}{\partial x^2} \right]^2 dx. \tag{2.43}$$

Let $y(x,t) = Y(x)f(t)$ then:

$$T(t) = \frac{1}{2}\dot{f}^2(t) \int_0^L m_x(x)Y^2(x)dx, \tag{2.44}$$

$$V(t) = \frac{1}{2}f^2(t) \int_0^L EI(x) \left[ \frac{\partial Y(x)}{\partial x^2} \right]^2 dx, \tag{2.45}$$

and the natural frequencies given by:

$$\omega_n^2 = \frac{V_{max}}{T^*} = \frac{\int_0^L EI(x) \left[ \frac{d^2Y(x)}{dx^2} \right]^2 dx}{\int_0^L m_x(x)Y^2(x)dx}. \tag{2.46}$$

Estimating the first natural frequency and modeshape is essential to define the lumped-parameter model if the infinite-mode continuous model is not needed or is difficult to compute. This is the case for systems excited around their first natural frequency.

### 2.3.2 Lumped Parameter Model

Using a lumped parameter model for AFM probes in scanning applications has been extensively studied [94, 87, 95, 96] and a comparison between continuous and point-mass models has been addressed in [90] for tapping mode microscopy. As the mechanical probe becomes more complex in structure, and the requirements on the accuracy of the probe tip are higher, continuous models will become more relevant. This is very important especially for advanced cantilever designs incorporating smart structures where continuity conditions and geometrical compatibility conditions must be satisfied. This approach will be followed and illustrated in our preliminary results for the proposed new probe designs.

## 2.4 Conclusions

An improved modeling of the nanoscale physics and mechanics is an important milestone towards more accurate and repeatable nanomanipulation. These physics are governed by surface forces. In the present chapter, new modeling of nano-friction and adhesion were proposed. Moreover, different approaches of modeling the probe dynamics were quickly reviewed at the end of the chapter. A new dynamic nanoscale friction model introducing the notion of generalized bristle deflection was proposed to model single asperity contacts. The model was shown to represent the most important characteristics of nano-friction, mainly the stick-slip behavior and the pre-sliding conditions. In addition, an improved modeling of the adhesion was adopted using the MD mechanics to describe the probe-sample contact characteristics. The effects of long distance van der Waals attractions were also taken into account. The model is able to describe the interactions for a large range of probe-sample material and geometrical properties. Conducted simulations show also the important cou-

pling between the friction and adhesion at the nanoscale. The developed modeling of the physics and obtained results are expected to help develop more accurate control strategies that improve the manipulation accuracy. However, the restricted maneuverability of available probes will remain a main obstacle towards achieving useful nanomanipulation tasks. In the next chapter, we will address this limitation by introducing two smart probes that will allow for true tip maneuverability and simultaneous actuation and sensing of its motion.

# Chapter 3

# Smart Mechanical Probes

Prototyping and fabrication of nano-devices require sub-nanometer tolerances and highly accurate sensing and actuation. A major limitation of existing nanomanipulation systems is the constrained motion and maneuver of the end-effector. In this chapter, we will propose new designs of AFM probes suitable for nanomanipulation. The designs rely on active elements that improve the sensing and actuation capabilities of the AFM as a nanomanipulator.

## 3.1  Available Works on Modified Probes

The original design of the AFM includes a passive probe made of $Si$ that is scanned in a raster pattern (serial scan) over a sample during imaging. Researchers proposed modified probes to improve the imaging and manipulation capacities of the AFM.

### 3.1.1  Improved Probes for Imaging

Naturally, the first modified probes proposed in the literature focused on improving the functioning of the AFM as a microscope. Minne et al. [97] fabricated and operated two cantilevers in parallel in a new AFM imaging mode. The design includes both an integrated piezoresistive $Si$ sensor and an integrated piezoelectric $ZnO$ actuator on each cantilever. The integration of a sensor and an actuator on a single cantilever allowed to simultaneously record two independent AFM images in the constant force mode. Using this design, they were able to remove the photodetection system and increase the speed

and range of imaging.

More advanced designs were recently proposed to further increase the imaging speed during tapping mode. Onaran et al. [98] probe is an example of such an advanced design. The probe has a sharp tip placed on a micromachined membrane with an integrated displacement sensor and a diffraction-based optical interferometer. The design offers the unique capability of measuring dynamic interaction forces at high speeds. The probe was used to directly measure the transient interaction forces between the probe tip and the sample when operating in a dynamic mode. Images related to viscoelasticity and adhesion of the samples were formed by recording salient features of individual tap signals.

### 3.1.2 Improved Probes for Manipulation

Because of the limited manoeuvrability of AFM probes, researchers tried to improve the AFM use as a nanomanipulator through modifying its probe. Some works focused on using passive techniques to modify the AFM tip trajectories. For instance, Muraoka et al. [99, 100] proposed a concentrated-mass probe, which consisted of an AFM probe with a significant tip-mass, to achieve controlled nanoscale rubbing (Figure 3.1).
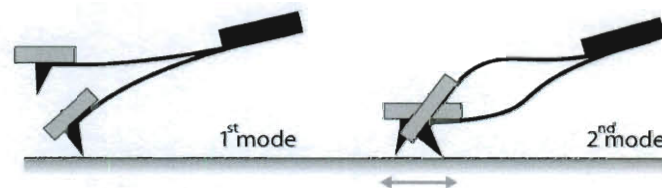


**Figure 3.1:** Concentrated mass probe proposed by Muraoka et al.

The probe design was developed so that the second vibrational modeshape was modified to move the second node to the free-end of the beam. As a result, the tip moved horizontally when the system **was excited near** the structure's second natural frequency providing the means to horizontally scratch the sample surface. The linear trajectories which depended on the configuration of the device were utilized to accomplish different nano-machining

processes. However, relying only on passive modifications of the probe cannot guarantee the desired maneuverability needed for nanomanipulation.

Researchers proposed also incorporating active elements to improve the use of AFM cantilevers in nanomanipulation. For example, Zhang et al. [101] developed a smart probe that allows to control the cantilever stiffness. The simple design includes a piezopatch that is actuated in order to overcome the tip slipping over nano-samples during manipulation. The probe is fabricated from bulk $Si$ with a $ZnO$ piezoelectric film patterned on the bottom of the cantilever (Figure 3.2). The design was originally developed to improve the tapping mode imaging rate than tested in the framework of nanomanipulation. The initial results are promising, however, the cantilever is not able to achieve controlled motion of the tip.
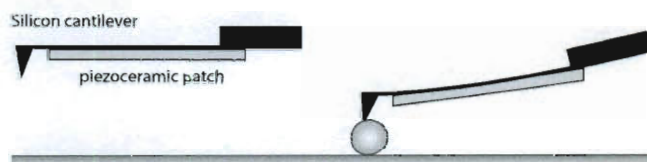


**Figure 3.2:** Active probe proposed by Zhang et al.

Despite that many groups proposed incorporating smart elements in AFM probes to improve their operation, few studies have focused on studying the tip trajectories of AFM probes modified using piezoelectric actuators. In a recent publication, Chen et al. [102] studied the tip trajectories of an AFM-type probe augmented with a piezopatch (Figure 3.3-a). Two independent inputs were applied to the probe: an actuation voltage and a probe base excitation. The forced vibration of this model with respect to these two independent inputs was analyzed. The trajectory of the tip was obtained from the motion of the free-end of the cantilever beam. Based on the resonant response to harmonic inputs at the second dynamic mode, nanoscale elliptical and linear tip trajectories were predicted (Figure 3.3-b). The lengths of the linear trajectories can be changed within a large nanometer range by adjusting the magnitude of the base excitation. Furthermore,

through varying the magnitudes of the base excitation and the piezoelectric actuator independently, the semi-minor axis, the semi-major axis and the rotational angle of the elliptical trajectories can be adjusted in-situ. This work showed how a smart beam could produce nanoscale curved tip trajectories that can be used in nanomanipulation.
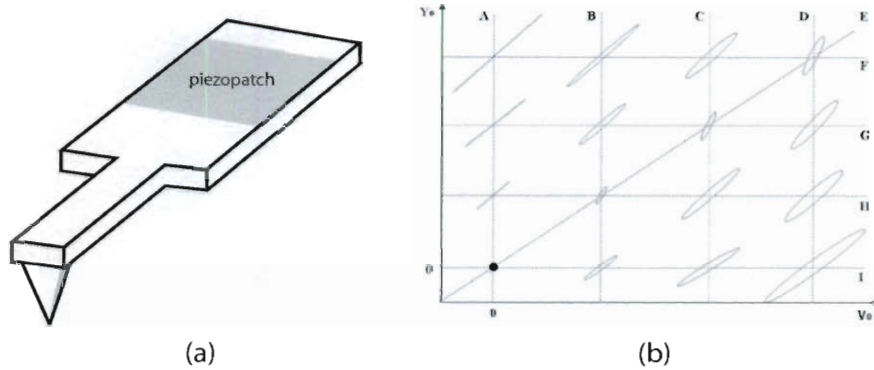


**Figure 3.3:** Active probe proposed by Chen et al. (a) design (b) tip trajectories

Building on these initial results, we propose two new probe designs, namely the duo-biomorph based and the piezotube based probes, that allow for more accurate local tip displacements and stiffness adjustment in-situ. The duo-bimorph probe guarantees two directional local tip motion and includes a frontal bimorph to tune the cantilever stiffness. The design is ideal for the nano-machining of vertical surfaces but cannot be used to push nano-particles in three dimensions. This limitation motivated the development of the second design that uses a piezotube base for three dimensional tip motion. Next, we will present these two new probes and derive the dynamics of their tip motion.

## 3.2   Duo-Biomorph Based Probe

In order to ensure increased control on the tip position during fast manipulation, we propose a new design of a smart cantilever that is based on a duo-bimorph to allow for local accurate vertical and horizontal tip motion.

## 3.2.1 Design Details

The main component of the proposed design is a duo-bimorph that is used to generate accurate transverse and lateral displacements of the AFM tip (Figure 3.4). The duo-bimorph actuator was first used in micro-gripper design and shown to generate adequate forces [103]. The smart element includes two piezolayers whose polarities are carefully arranged (Figure 3.5).
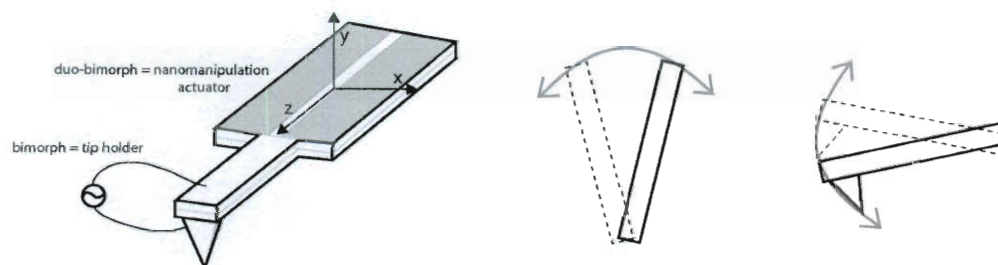


**Figure 3.4:** Details of the duo-biomorph probe design and corresponding tip motion
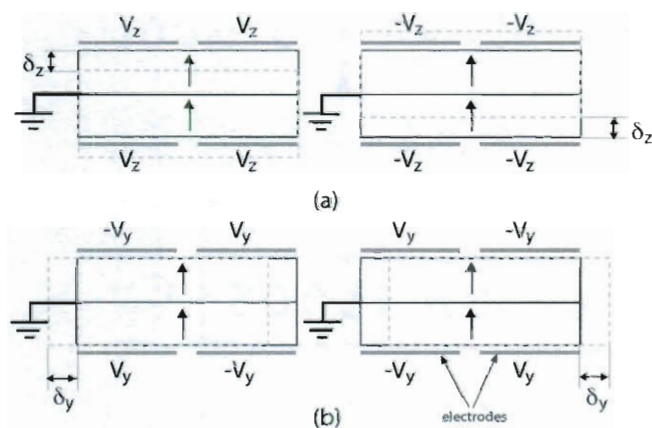


**Figure 3.5:** Duo-biomorph actuation principle (a) vertical motion (b) lateral motion

The arrangement of the electrodes allows for transverse and lateral tip motion. The transverse displacement or bending of the actuator is achieved by setting the four electrodes at the same voltage (Figure 3.5-a). As a result, the upper layer stretches along $x$ and the

lower layer contracts proportionally to the material piezoelectric strain/charge coefficient. The lateral motion of the tip is achieved by setting the voltages on two adjacent or two opposite electrodes as $V$ and $-V$. This results in a stretch and contraction of the upper and lower layers respectively along $y$ and leads to the lateral tip motion (Figure 3.5-b).

AFM-based nanomanipulation generally involves repeated switching between the imaging and manipulation modes (Figure 3.6). A known dilemma in AFM-based fabrication is that a stiff cantilever is needed to manipulate samples, whereas a compliant cantilever is required to enhance imaging [52]. In fact, AFMs often employ compliant cantilevers to avoid compressing the sample surface and to improve force resolution during force sensing phases. Stiff cantilevers are however needed to enable pushing relatively large and sticky samples. A piezolayer attached to the tip-holder is used to address this problem by controlling the cantilever's rigidity in-situ during nanomanipulation.
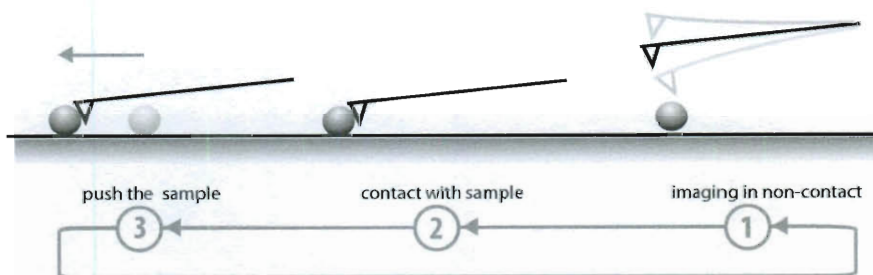


**Figure 3.6:** Typical nano-pushing task phases

Actuating the duo-biomorph allows for accurate transverse and lateral positioning of the tip. The same smart element can be used to obtain feedback information about the tip motion. In addition, the sensing capability can be explored to detect loosing contact with the sample during nanomanipulation. Simultaneous actuation and sensing could be achieved using two opposite electrodes for actuation and the remaining two for sensing. Different electrode patterns would allow for improved deflection range for combined actuation and sensing. The design is adequate for different types of machining and manipulation tasks at the nanoscale. For instance, the bending motion and the stiffening of the can-

tilever would allow for cutting and controlled load nano-lithography. The swing motion can be used in nano-pushing manipulation.

## 3.2.2   Probe Dynamics

The dynamics of the AFM tip according to the proposed design are the result of the lateral and vertical extensions of the piezolayers. We will adopt a lumped-parameter approach to analyze the dynamics of the proposed nanomanipulator (Figure 3.7).
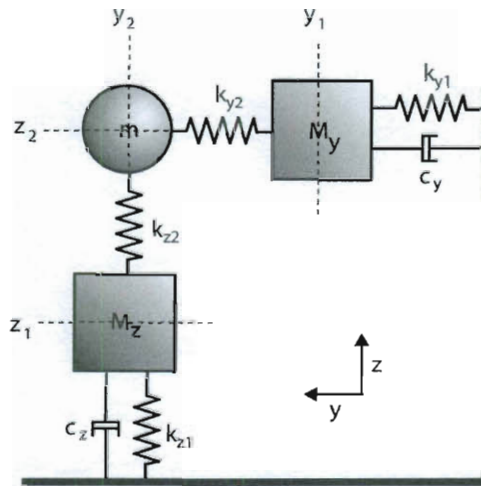


**Figure 3.7:** Lumped-parameter model of the combined lateral and longitudinal dynamics

The corresponding parameters are obtained from the first natural mode $(\omega^i, \phi^i)$ of the lateral and vertical vibrations. The choice of this method is motivated by the fact that the proposed cantilever is intended to be used in contact mode manipulation where the effects of higher order dynamics can be neglected. The lumped masses $M_i$, damping $c_i$ and stiffness coefficients $k_{i1}$ $(i \in \{y, z\})$ are given by:

$$M_i = \rho A \int_0^L (\phi^i(x))^2 dx, \tag{3.1}$$

$$c_i = \mu \int_0^L (\phi^i(x))^2 dx, \tag{3.2}$$

$$k_{i1} = M_i(\omega^i)^2, \tag{3.3}$$

where $L$, $A$ and $\rho$ represent the length, the cross-sectional area and the material density of the duo-biomorph. $\mu$ denotes the environment damping factor.

### 3.2.2.1 Lateral Motion

According to the proposed design, the tip can describe controlled motion as a result of the two-axes actuation of the nanomanipulation duo-biomorph. The magnitude of these displacements depends on the cantilever dimensions and the applied voltages. The lateral dynamics of the smart cantilever can be described by the following set of equations:

$$\begin{cases} M_y\ddot{y}_1 = k_{y2}(y_2 - y_1) - c_y\dot{y}_1 - k_{y1}y_1 + F_y, \\ m\ddot{y}_2 = -k_{y2}(y_2 - y_1). \end{cases} \tag{3.4}$$

$y_1$ and $y_2$ represent the coordinates of the center of mass of the duo-biomorph and the coordinate of the AFM tip, respectively. $m$ is the mass of the header component of the cantilever and $k_{y2}$ is its stiffness in the $y$ direction. $M_y$, $c_y$ and $k_{y1}$ are the corresponding lumped model parameters given by equations (3.1), (3.2) and (3.3). In order to evaluate these parameters, it is essential to determine the expression of $\phi_1^y$.

Using the constitutive equations of a duo-biomorph derived in [104], the governing equation corresponding to the lateral displacements of the cantilever can be written in the form:

$$\rho A \frac{\partial^2 v}{\partial t^2} + \mu \frac{\partial v}{\partial t} + \frac{hw^3}{12s_{11}^E} \frac{\partial^4 v}{\partial x^4} = \frac{\partial}{\partial x}\left(\frac{d_{31}(w^2 - w_0^2)}{s_{11}^E}V_y\delta(x - L)\right), \tag{3.5}$$

where $v$ denotes the displacement in the $y$ direction. $w$, $h$ and $w_0$ are the duo-bimorph width and thickness and the electrodes' separation distance, respectively. $\rho$, $s_{11}^E$ and $d_{31}$ represent the density, the long-axis elastic compliance and the strain/charge coefficient of the piezoelectric material. $V_y$, the applied voltage, is the main actuation parameter. The corresponding BCs that take into account the presence of the tip holder at the duo-bimorph free-end are given by:

$$v|_{x=0} = 0, \tag{3.6}$$

$$\frac{\partial v}{\partial x}\Big|_{x=0} = 0, \tag{3.7}$$

$$m\frac{\partial^2 v}{\partial t^2}\Big|_{x=L} + \mu\frac{\partial v}{\partial t}\Big|_{x=L} = \frac{hw^3}{12s_{11}^E}\frac{\partial^3 v}{\partial x^3}\Big|_{x=L}, \tag{3.8}$$

$$\frac{hw^3}{12s_{11}^E}\frac{\partial^2 v}{\partial x^2}\Big|_{x=L} = 0. \tag{3.9}$$

For analytical convenience, the BCs are derived assuming that a very thin virtual piezo-electric slice exists between the biomorph and the tip so that the edge itself is moment free and merely connected to the mass $m$ as it was done in [105] to derive the governing equations of a piezotube with a mass at its end. The corresponding eigenvalue problem yields the following transcendental equation:

$$\lambda_n L(cos(\lambda_n L)cosh(\lambda_n L) + 1) +$$
$$\frac{m}{\rho AL}(cos(\lambda_n L)sinh(\lambda_n L) - cosh(\lambda_n L)sin(\lambda_n L)) = 0. \tag{3.10}$$

Solving the above equation for $\lambda_n$, we obtain the corresponding natural frequencies using $\omega_n^y = \sqrt{\frac{hw^3}{12\rho As_{11}^E}}\lambda_n^2$. The modeshapes of the lateral dynamics of the duo-bimorph are given by:

$$\phi_n^y(x) = (cos(\lambda_n x) - cosh(\lambda_n x)) + \frac{cos(\lambda_n L) + cosh(\lambda_n L)}{sin(\lambda_n L) + sinh(\lambda_n L)}(sinh(\lambda_n x) - sin(\lambda_n x)). \tag{3.11}$$

Substituting the obtained values of $\omega^y = \omega_1^y$ and $\phi^y = \phi_1^y$ in equations (3.1), (3.2) and (3.3) yields the model parameters corresponding to the cantilever lateral dynamics. In addition, the actuation force $F_y$ is obtained from the applied voltage $V_y$ as [106]:

$$F_y = \int_0^L \phi^y(x)\frac{\partial}{\partial x}\left(\frac{d_{31}(w^2 - w_0^2)}{s_{11}^E}V_y\delta(x - L)\right) dx. \tag{3.12}$$

### 3.2.2.2  Transverse Motion

Using the same assumptions with respect to the contact between the duo-biomorph and the tip holder, the vertical dynamics of the probe are governed by:

$$\rho A\frac{\partial^2 u}{\partial t^2} + \mu\frac{\partial u}{\partial t} - \frac{h^3 s_{11}^E}{12}\frac{\partial^2 u}{\partial x^4} = \frac{\partial}{\partial x}\left(\frac{d_{31}(w - w_0)h}{2s_{11}^E w}V_z\delta(x - L)\right). \tag{3.13}$$

The corresponding BCs are given by:

$$u|_{z=0} = 0, \tag{3.14}$$

$$\frac{\partial u}{\partial x}|_{z=0} = 0, \tag{3.15}$$

$$m\frac{\partial^2 u}{\partial t^2}|_{z=L} + \mu\frac{\partial u}{\partial t}|_{z=L} = \frac{h^3 s_{11}^E}{12}\frac{\partial^3 u}{\partial x^3}|_{z=L}, \tag{3.16}$$

$$\frac{h^3 s_{11}^E}{12}\frac{\partial^2 u}{\partial x^2}|_{z=L} = 0. \tag{3.17}$$

Solving the eigenvalue problem leads to eigenvectors that have the same expression as those corresponding to the lateral dynamics (equation (3.11)). However, the natural frequencies of the vertical dynamics are given by:

$$\omega_n^z = \sqrt{\frac{h^3}{12\rho A s_{11}^E}}\lambda_n^2. \tag{3.18}$$

The corresponding model lumped parameters ($M_z$, $c_z$ and $k_{z1}$) are obtained in a similar manner using equations (3.1), (3.2) and (3.3). The vertical displacement actuation force is given by:

$$F_z = \int_0^L \phi^z(x)\frac{\partial}{\partial x}\left(\frac{d_{31}(w - w_0)h}{2s_{11}^E w}V_z\delta(x - L)\right)dx. \tag{3.19}$$

Next, we will use the developed model to investigate the effectiveness of path tracking using the proposed smart probe. The obtained expressions of the actuation forces will be used to evaluate the actuation input.

### 3.2.3   Path Tracking

In order to achieve accurate path tracking, the system is actuated with two voltages: $V_y$ and $V_z$. The actuation allows to describe trajectories in the $(y, z)$ plane. The corresponding tip motion can be used to achieve basic machining tasks at the nanoscale (creating nano-trenches, polishing vertical surfaces ...). The system of equations (3.4) is used to determine the relations between the voltage inputs and the position of the tip. A proper selection of the inputs will allow describing desired trajectories. To illustrate this property, Figure 3.8 represents three different trajectories of the tip and the corresponding voltage inputs.
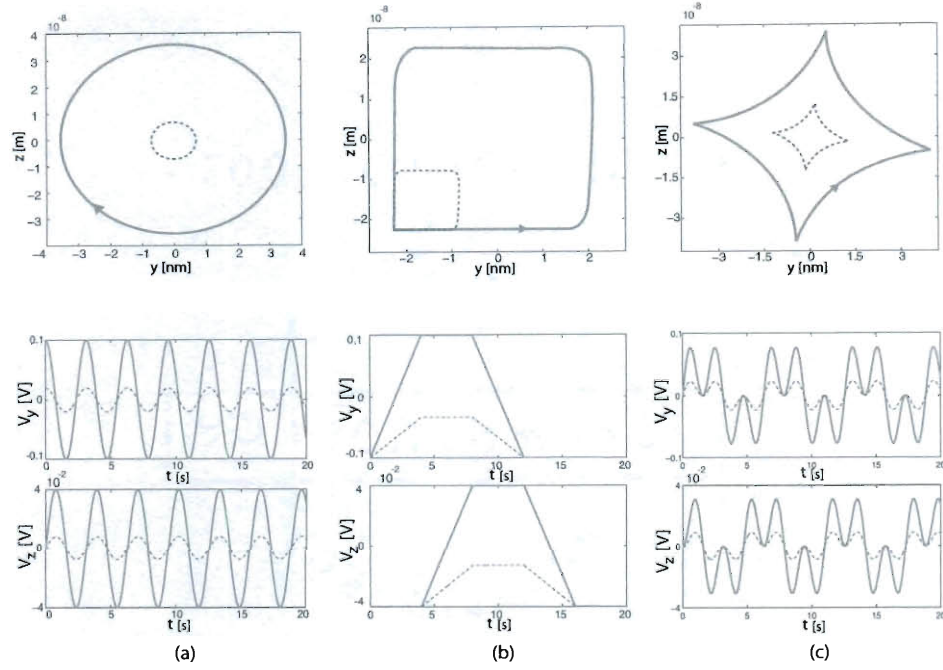
**Figure 3.8:** Duo-bimorph probe tip trajectories and corresponding actuation voltages

Table 4.4 includes the parameters used for the simulations. The cantilever geometrical dimensions are common values of cantilevers used in AFM contact mode. Next, we will present the piezotube based design that allows for controlled tip motion in the $x$ direction in addition to the $(y, z)$ axes.

**Table 3.1:** Path tracking parameters of the duo-biomorph based probe

| PARAMETER | VALUE | PARAMETER | VALUE | PARAMETER | VALUE |
|---|---|---|---|---|---|
| $m_h$ | $2e{-}7$ kg | $m$ | $0.5e{-}7$ kg | $L_h$ | $50e{-}6$ m |
| $k_{y2}$ | $0.1$ N/m | $k_{z2}$ | $10$ N/m | $L$ | $300e{-}6$ m |
| $w$ | $30e{-}6$ m | $w_0$ | $5e{-}6$ m | $\rho$ | $7800\ kg/m^3$ |
| $h$ | $10e{-}6$ m | $d_{31}$ | $185e{-}12$ C/N | $s_{11}^E$ | $20.7e{-}12$ m/N |

## 3.3 Piezotube Based Probe

### 3.3.1 Design Details

Commercial AFMs generally contain a vertical positioning piezotube that is used to move the probe or the sample in a raster pattern during imaging scans [107]. In order to increase the control on the tip position and allow it to describe fast and controlled 3D motion, we propose augmenting the cantilever with a horizontal piezotube, that we will refer to as nanomanipulation piezotube. The actuation base is mounted to the AFM cantilever using a holder. The proposed design includes also a piezolayer, attached to the tip-holder, used to tune the cantilever stiffness during the nanomanipulation (Figure 3.9).
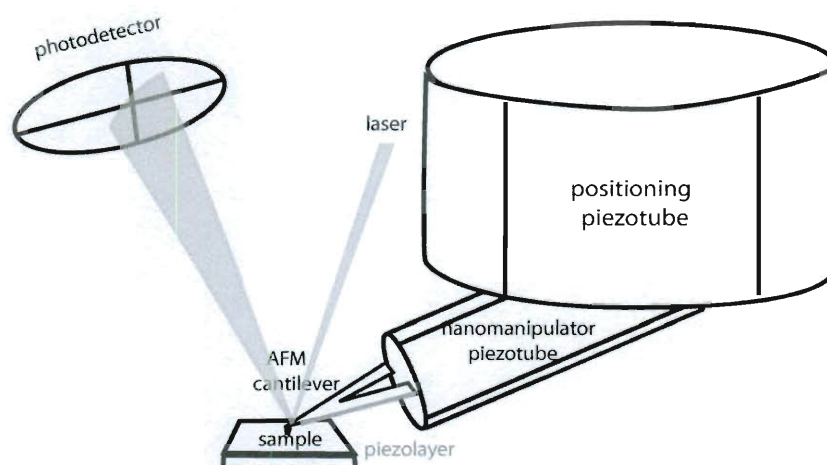


**Figure 3.9:** Proposed nanomanipulator design

According to the proposed design the nanomanipulator tip can describe controlled 3D motion resulting from the three axes actuation of the nanomanipulation piezotube. Lateral extensions correspond to vertical and horizontal displacements of the tip in the $x$ and $y$ directions, respectively. Whereas, the $z$-dynamics of the nanomanipulator are driven by the longitudinal extension of the piezotube (Figure 3.10). The magnitude of these displacements depends on the piezotube dimensions and the applied voltages.
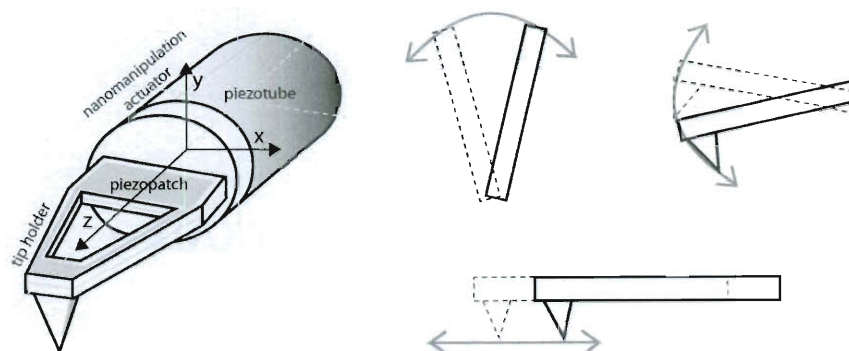
**Figure 3.10:** Details of the piezotube based design and corresponding tip motion

Piezotubes comprise a tube of radially poled piezoelectric material, four external and one internal electrodes to allow for lateral and longitudinal motions, respectively. They have many advantages such as three axes control capability, compact design and high frequency response. In addition, piezotubes have a good noise profile and allow for sub-nanometer actuation. The symmetry of the piezotube structure reduces thermal problems during high speed operation. New advances in piezotube manufacturing and design make them more attractive for nanomanipulation applications. In fact, piezotubes with smaller diameters down to $1mm$ were recently fabricated and tested [108]. New electrode patterns that improve their operating range were also designed (Figure 3.11).
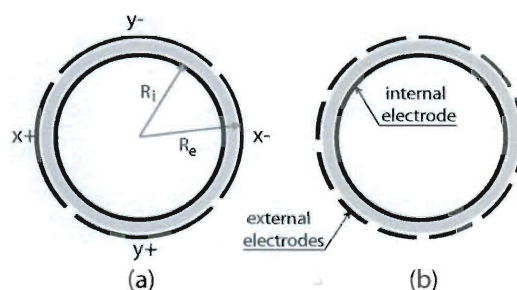


**Figure 3.11:** Piezotube electrode pattern (a) quartered electrodes design (b) 12 equal sector electrodes

For example, Moheimani and Yong [109] proposed segmenting the external electrode into 12 equal sectors of 30° allowing for combining simultaneous actuation and sensing with symmetric operation. Incorporating these advances into AFM-based nanomanipulators opens the door for size optimization and the possibility of implementing more advanced control schemes.

As a result of the three axes actuation, the smart probe can in principle perform different fabrication tasks at the nanoscale including lithography, controlled pushing and basic nanomachining tasks (Figure 3.12). Using the sensing capability of the proposed design will enable real-time feedback and validation of the manipulation outcome. This capability is essential to increase the manipulation accuracy and makes the proposed design easily incorporated into haptic interface systems.
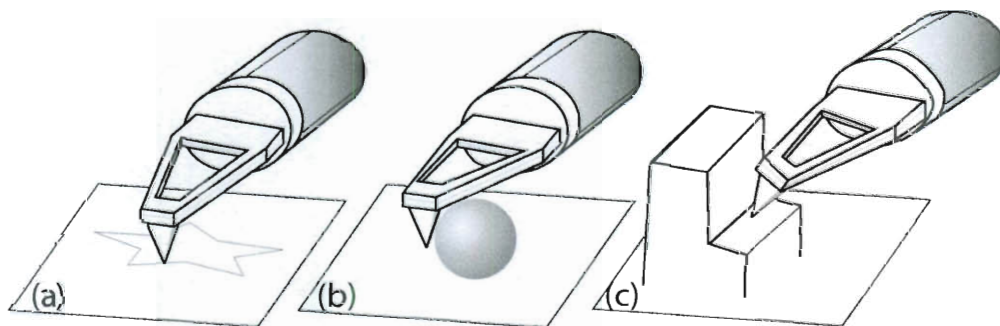


**Figure 3.12:** Nanomanipulation tasks (a) lithography (b) nano-pushing (c) nano-machining

Next, we will analyze the 3D dynamics of the nanomanipulator's end-effector corresponding to the lateral and longitudinal extensions of the nanomanipulation piezotube.

## 3.3.2 Probe Dynamics

In order to derive the end-effector governing equations, a lumped-parameter modeling approach is used. The cantilever tip is modeled as a concentrated mass $m$ positioned at $(x_t, y_t, z_t)$ and attached to the holder characterized by a stiffness $k_t$ and mass $m_h$ (Figure 3.13). The nanomanipulation piezotube dynamics will be represented by their first lateral

and longitudinal modes. The adopted approximation is reasonable for nanomanipulation applications where the smart cantilever is not expected to be driven at high oscillating frequencies. The resulting dynamics can be described by:

$$
\begin{cases}
M_x \ddot{x}_p = k_{tx}(x_t - x_p) - c_{px}\dot{x}_p - k_{px}x_p + u_x, \\
M_y \ddot{y}_p = k_{ty}(y_t - y_p) - c_{py}\dot{y}_p - k_{py}y_p + u_y, \\
M_z \ddot{z}_p = k_{tz}(z_t - z_p) - c_{pz}\dot{z}_p - k_{pz}z_p + u_z, \\
m\ddot{x}_t = -c_{tx}(\dot{x}_t - \dot{x}_p) - k_{tx}(x_t - x_p), \\
m\ddot{y}_t = -c_{ty}(\dot{y}_t - \dot{y}_p) - k_{ty}(y_t - y_p), \\
m\ddot{z}_t = -c_{tz}(\dot{z}_t - \dot{z}_p) - k_{tz}(z_t - z_p).
\end{cases}
\tag{3.20}
$$

$(x_p, y_p, z_p)$ represents the position of the center of mass of the nanomanipulation piezo-tube. The lumped masses $M_i$, damping $c_{pi}$ and stiffness coefficients $k_{pi}$, representing the piezotube dynamics, are defined by equations (3.1), (3.2) and (3.3). $\phi^i$ and $\omega^i$ denote the piezotube first modeshape and natural frequency in the $i$ direction ($i \in \{x, y, z\}$). $\mu$ is the environment damping factor.
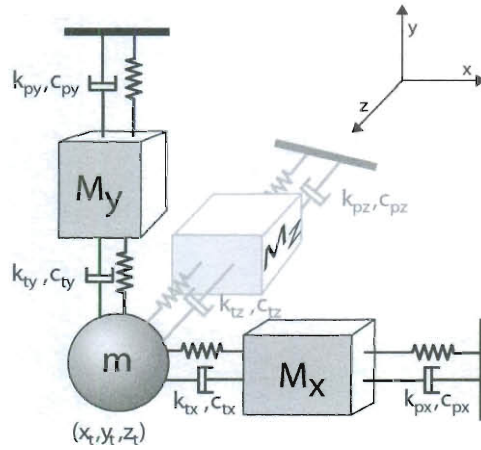


**Figure 3.13:** Lumped parameter model of the combined lateral and longitudinal dynamics of the piezotube based probe

### 3.3.2.1 Lateral Motion

In order to evaluate the end-effector's $x - y$ dynamics, it is essential to define the first mode corresponding to the lateral extensions of the nanomanipulation piezotube. These are given by [105]:

$$\rho A \frac{\partial^2 v}{\partial t^2} + \mu \frac{\partial v}{\partial t} + \frac{\pi R^3 (R_e - R_i)}{s_{11}^E} \frac{\partial^4 v}{\partial z^4} = \frac{\partial}{\partial z} \left( \frac{2\sqrt{2} R^2 d_{31}}{s_{11}^E} V_d \delta(z - L) \right), \tag{3.21}$$

where $v$ denotes the displacement in the $d$ direction ($d \in \{x, y\}$). $R_e$ and $R_i$ are the outer and inner radii of the piezotube and $R = (R_e + R_i)/2$. The parameters $s_E$ and $d_{31}$ represent the long-axis elastic compliance and the piezoelectric strain/charge coefficient of the piezotube, respectively. $V_d$, the applied voltage, is the main actuation parameter. The corresponding BCs that take into account the presence of the tip holder at the end of the piezotube are given by:

$$v|_{z=0} = 0, \tag{3.22}$$

$$\frac{\partial v}{\partial z}|_{z=0} = 0, \tag{3.23}$$

$$m_h \frac{\partial^2 v}{\partial t^2}|_{z=L} + \mu \frac{\partial v}{\partial t}|_{z=L} dz = \frac{\pi R^3 (R_e - R_i)}{s_{11}^E} \frac{\partial^3 v}{\partial z^3}|_{z=L}, \tag{3.24}$$

$$\frac{\pi R^3 (R_e - R_i)}{s_{11}^E} \frac{\partial^2 v}{\partial z^2}|_{z=L} = 0. \tag{3.25}$$

The resulting transcendental equation and modeshapes have the same expression as the corresponding ones of the duo-biomorph design. However, in the present case the natural frequencies are given by $\omega_n^d = \sqrt{\frac{\pi R^3 (R_e - R_i)}{\rho A s_{11}^E}} \lambda_n^2$. In addition, the actuation force $F_d$ is obtained from the applied voltage as:

$$F_d = \int_0^L \phi^d(z) \frac{\partial}{\partial z} \left( \frac{2\sqrt{2} R^2 d_{31}}{s_{11}^E} V_d \delta(z - L) \right) dz. \tag{3.26}$$

### 3.3.2.2 Transverse Motion

The $z$-dynamics and the corresponding actuation force $F_z$ are obtained in a similar manner using the longitudinal piezotube extension governed by [105]:

$$\rho A \frac{\partial^2 u}{\partial t^2} + \mu \frac{\partial u}{\partial t} - \frac{A}{s_{11}^E} \frac{\partial^2 u}{\partial z^2} = \frac{A d_{31}}{s_{11}^E (R_o - R_i)} V_z \delta(z - L). \tag{3.27}$$

The corresponding BCs are given by:

$$u|_{z=0} = 0, \tag{3.28}$$

$$m_h \frac{\partial^2 u}{\partial t^2}|_{z=L} + \mu \frac{\partial u}{\partial t}|_{z=L} = -\frac{A}{s_{11}^E} \frac{\partial u}{\partial z}|_{z=L}. \tag{3.29}$$

Using the method of separation of variables, we obtain the corresponding natural frequencies $\omega_n^z$ defined by $\frac{\omega_n^z L}{a} \tan\left(\frac{\omega_n^z L}{a}\right) = \frac{\rho A L}{m_h}$ and modeshapes $\phi_n^z = sin(\frac{\omega_n^z z}{a})$. The corresponding actuation force $F_z$ is obtained from the first modeshape $\phi^z(z) = \phi_1^z(z)$ through:

$$F_z = \frac{A d_{31}}{s_{11}^E (R_e - R_i)} V_z \phi^z(L). \tag{3.30}$$

### 3.3.3 Path Tracking

The simulation parameters used in this section are summarized in Table 4.4. The piezotube material and geometrical properties were taken from [108].

**Table 3.2:** Path tracking parameters of the piezotube based probe

| PARAMETER | VALUE | PARAMETER | VALUE | PARAMETER | VALUE |
|---|---|---|---|---|---|
| $m_h$ | $0.02e{-}3$ kg | $\rho$ | $7800$ $kg/m^3$ | $\mu$ | $0.1$ |
| $R_e$ | $0.5e{-}3$ m | $R_i$ | $0.3e{-}3$ m | $s_{11}^E$ | $20.7e{-}12$ m/N |
| $L$ | $5e{-}3$ m | $d_{31}$ | $185e{-}12$ C/N | | |

In order to achieve accurate path tracking, the system is actuated with three voltages: $V_x$, $V_y$ and $V_z$. $V_x$ and $V_z$ are used to describe plane paths. However, $V_y$ is used to compensate for rough substrates or to create cuts by applying a normal force. The combination of the three axes actuation allows for highly accurate nanofabrication and nanomachining tasks. The system of equations (3.20) presents the relations between the voltage inputs and the position of the probe tip. A proper selection of the input will allow describing desired trajectories. To illustrate this property, Figure 3.14 represents two different trajectories of the tip and the corresponding voltage inputs.
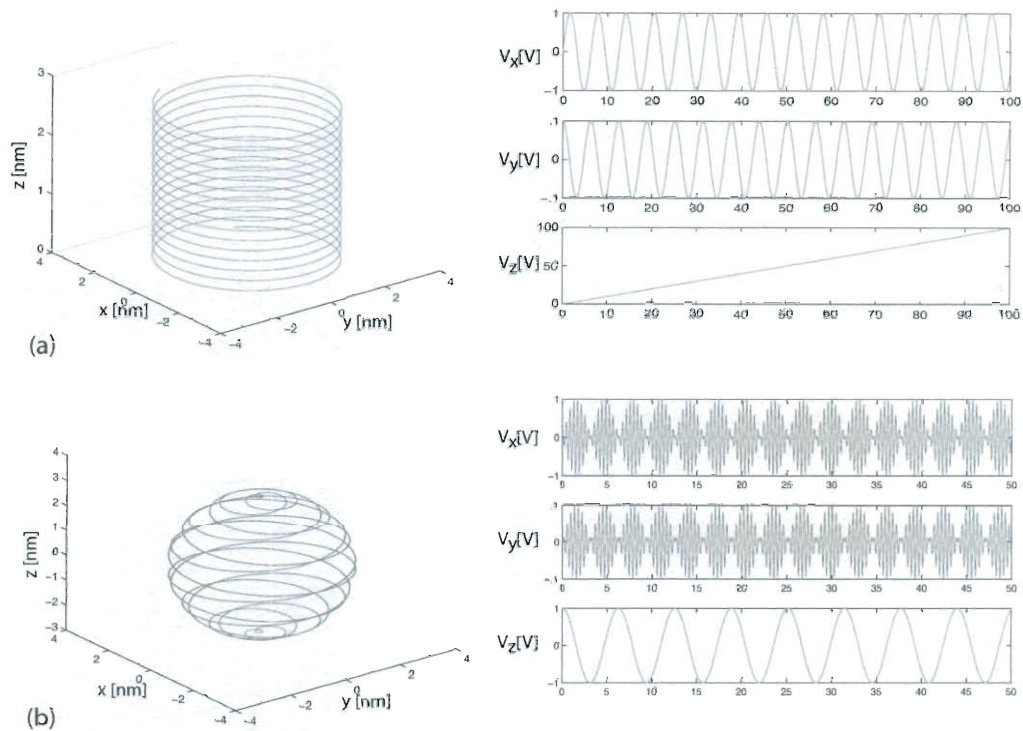
**Figure 3.14:** Examples of tip trajectories and corresponding actuation voltages (a) cylindrical path (b) spherical path

In the next section, we will analyze the effects of key parameters on the performance of the proposed probes. The results of the analysis can be used to further optimize the designs for nanomanipulation applications.

## 3.4   Design Considerations

Aforementioned simulations show clearly the ability of the proposed designs to describe controlled trajectories at the nanoscale. However, the effects of key parameters of the proposed designs, namely the probe stiffness and the characteristic dimensions, on the tracking performance should be investigated.

## 3.4.1 Effect of Probe Stiffness

As mentioned previously, the AFM cantilever stiffness plays a major role in the success of the nanomanipulation. Stiff cantilevers are, for instance, needed to avoid losing contact with samples during nano-pushing. For both duo-bimorph and piezotube based designs, Finite Element Analysis (FEA) using COMSOL Multiphysics show that the largest displacements are experienced by the tip and tip holder (Figure 3.15).
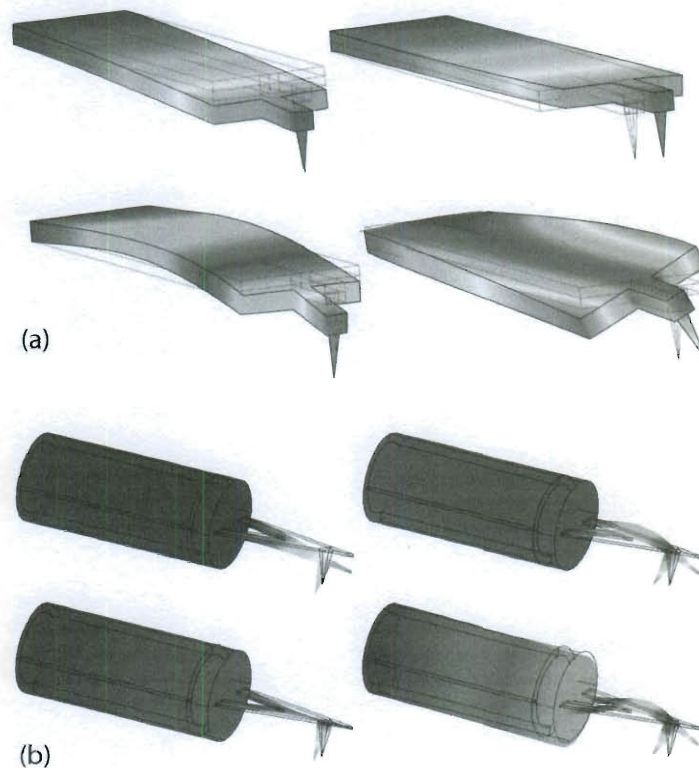


**Figure 3.15:** First four modeshapes of the (a) duo-biomorph and (b) piezotube based probes

The distortion of the probe base takes place only for high frequencies that are generally not excited in contact mode manipulation. The obtained modeshapes and the corresponding frequencies imply that a compliant tip holder may be unable to apply required forces to move the manipulated samples. In addition, it may undergo undesired oscillations during

path tracking. Simulation results clearly illustrate this point for the two proposed probes.

Figure 3.16-a represents simulated tracking of a circular trajectory, as an example of a 2D path, using the duo-biomorph probe for different values of the cantilever stiffness. A similar experiment is simulated for the piezotube probe consisting of tracking a trajectory around a predefined sphere for increased values of the probe stiffness (Figure 3.16-b). Cantilevers with stiffness of the order of $1N/m$ are generally used in imaging, whereas a stiffness from $10N/m$ to $50N/m$ is generally selected for manipulation. Simulations show that the more compliant the cantilever is, the more undesired oscillations are present. This is true for both probes. Acceptable results are obtained for stiff cantilevers with stiffness in the order of $100N/m$. One way to have such stiff cantilevers is to employ a piezolayer to tune the cantilever stiffness in-situ. The main advantage of this approach is that the same cantilever can provide accurate force sensing [110].
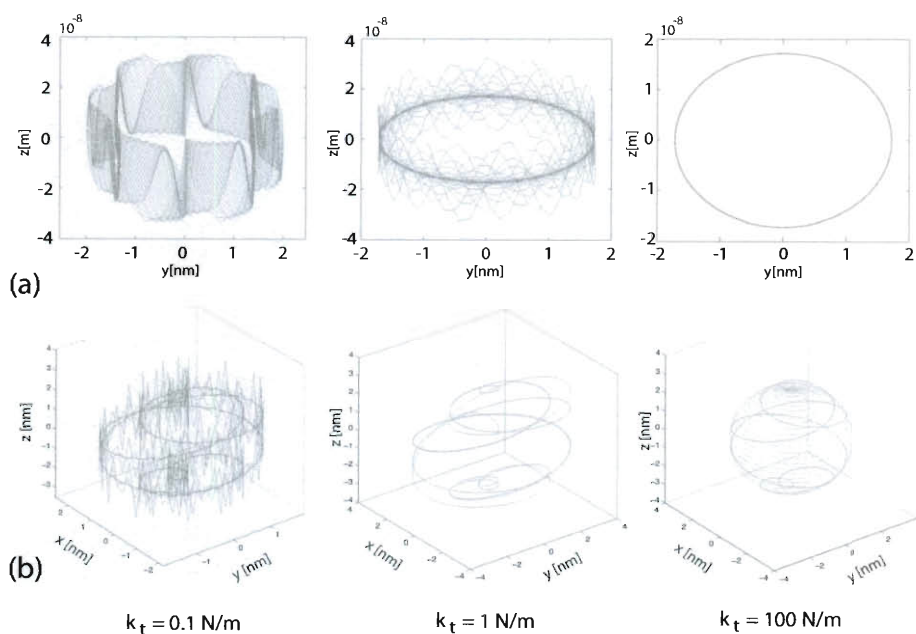


**Figure 3.16:** Effect of tip holder stiffness on path tracking for the (a) duo-biomorph and (b) piezotube based probes

## 3.4.2 Effect of Probe Dimensions

In any design, the selection of the dimensions must obey criteria that optimize the desired performance. In the present case, the measure of performance is the accuracy with which the nanomanipulator moves along a desired path.

### 3.4.2.1 Duo-biomorph based probe

Plane trajectories of the proposed design correspond to lateral and vertical displacements of the duo-bimorph. These displacements are related to the applied voltages through [103]:

$$\Delta_y = \frac{3d_{31}L^2(w^2 - w_0^2)}{hw^3}V_y, \tag{3.31}$$

$$\Delta_z = \frac{3d_{31}L^2(w - w_0)}{h^2w}V_z. \tag{3.32}$$

Assuming that the same magnitude of the displacements is required in the $y$ and $z$ directions ($\Delta_y = \Delta_z$), we have:

$$V_z = \frac{h(w + w_0)}{w^2}V_y. \tag{3.33}$$

which simplifies to $V_z \simeq \frac{h}{w}V_y$ for very small values of the electrode gap $w_0$. Thus, the required voltage in the $y$ direction is higher than in the $z$ direction since $w > h$ in general (Figure 3.17).
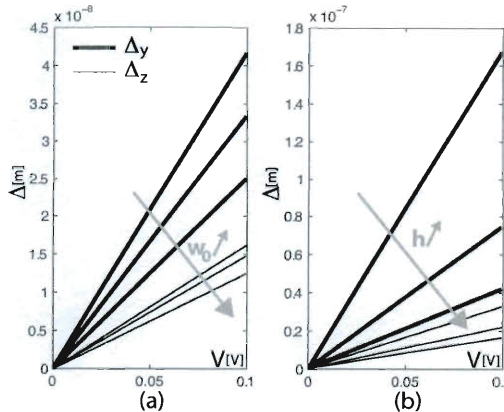


Figure 3.17: Effects of varying $w_0$ and $h$ on the duo-biomorph range

The aforementioned figure represents also the effects of increasing $w_0$ and $h$ on the range of a PZT-5H duo-biomorph. The results show that a range of the order of a few nanometers corresponds to reasonable voltage inputs in both $y$ and $z$ directions.

### 3.4.2.2 Piezotube based probe

Approximate relations exist that relate the piezotube extensions ($\Delta_x$, $\Delta_y$ and $\Delta_z$) to the applied voltages [107]:

$$\Delta_i = \frac{2\sqrt{2}d_{31}L^2}{\pi R_e(R_e - R_i)}V_i; \quad i \in \{x, y\}, \tag{3.34}$$

$$\Delta_z = \frac{d_{31}L}{(R_e - R_i)}V_z. \tag{3.35}$$

The proposed design implies that $V_x$ and $V_z$ are the main actuation parameters for path tracking allowing to describe plane paths in the substrate surface. Using equations (3.34) and (3.35), we obtain the following relation:

$$V_z \approx 0.9\frac{L}{R_e}V_x. \tag{3.36}$$

Since $L > R_e$ generally, the above equation shows that the required voltage in the $z$ direction is higher than in the $x$ direction. Figure 3.18 represents the effects of varying $L$ and $R_e$ on the range of a PZT-5H piezotube. Similarly to the case of the duo-biomorph probe, the simulations show that a reasonable voltage in both $x$ and $z$ directions lead to relatively large displacements of the tip.

The simulation results present an important validation of the feasibility of using the proposed designs for sub-nanometer path tracking. The difference between the magnitudes of the applied voltages can be reduced if needed through a proper selection of the probe dimensions. Next, we will investigate implementing advanced control schemes to monitor the motion of the tip during manipulation. The control schemes will take advantages of the advanced actuation and sensing capacities of the probes. The piezotube based probe will be used to illustrate that suitable control can be developed to reduce the effects of coupling and stick-slip interactions on the tip positioning accuracy.
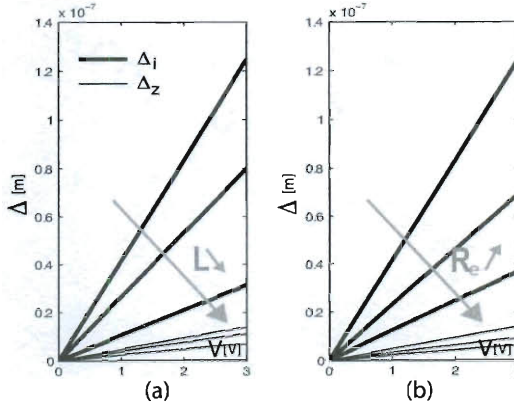
**Figure 3.18:** Effect of varying (a) $L$ and (b) $R_e$ on the piezotube range

## 3.5 Probe Control and Disturbance Rejection

In this section, a perturbation based control scheme will be devised. The main role of the control is to compensate for the inevitable actuation coupling and the disturbances at the nanoscale. The developments will show clearly the possibility of devising advanced control strategies for the proposed end-effectors based on their improved sensing and actuation capabilities. The piezotube based probe will be used for the simulations. However, the same developments can be applied to the duo-biomorph probe.

Let $q_1 = [x_t \quad y_t \quad z_t]^T$ and $q_2 = [x_p \quad y_p \quad z_p]^T$ be the tip and piezotube center of mass positions, respectively. The nanomanipulator dynamics can be expressed in the form:

$$\begin{cases} D\ddot{q}_1 + C\dot{q}_1 + K_1(q_1 - q_2) = F_d, \\ J\ddot{q}_2 - K_1(q_1 - q_2) + K_2 q_2 = U, \end{cases} \tag{3.37}$$

where the disturbance force is denoted by $F_d = [F_{dx} \quad F_{dy} \quad F_{dz}]^T$. $U = [U_x \quad U_y \quad U_z]^T$ represents the control effort. The different matrices are given by:

$$D = \begin{bmatrix} m & 0 & 0 \\ 0 & m & 0 \\ 0 & 0 & m \end{bmatrix}; \quad J = \begin{bmatrix} M_x & 0 & 0 \\ 0 & M_y & 0 \\ 0 & 0 & M_z \end{bmatrix}; \quad C = \begin{bmatrix} c_{tx} & 0 & 0 \\ 0 & c_{ty} & 0 \\ 0 & 0 & c_{tz} \end{bmatrix};$$

$$K_1 = \begin{bmatrix} k_{tx} & 0 & 0 \\ 0 & k_{ty} & 0 \\ 0 & 0 & k_{tz} \end{bmatrix} ; \quad K_2 = \begin{bmatrix} k_{px} & 0 & 0 \\ 0 & k_{py} & 0 \\ 0 & 0 & k_{pz} \end{bmatrix} ;$$

Due to inevitable fabrication errors, some eccentricity is always present in piezotubes. The eccentricity, which is typically of the order of 1% of the piezotube radius [111], leads to inevitable coupling between the $x$, $y$ and $z$ tube extensions. This relatively small eccentricity has significant implications for sub-nanometer positioning applications. Thus, its effects must be taken into account in our proposed nanomanipulator dynamics.

### 3.5.1 Control Effort

Rifai and Youcef-Toumi [111] developed a model that describes the effect of the eccentricity on the piezotube extensions coupling. Taken into account the eccentricity of the piezotube, the actuation force can be expressed as:

$$U = \begin{bmatrix} \sum\limits_{i \in \{x,y,z\}} \gamma_{xi} u_i \\ \sum\limits_{i \in \{x,y,z\}} \gamma_{yi} u_i \\ \sum\limits_{i \in \{x,y,z\}} \gamma_{zi} u_i \end{bmatrix} , \tag{3.38}$$

or in the compact form $U = \Gamma u$. The voltage input vector $u = [u_x \quad u_y \quad u_z]^T$ is the main actuation parameter. However as a result of the coupling, a voltage input in one direction may result in undesirable extensions in other directions. The entries of the $\Gamma$ matrix depend on the piezotube geometry and electrode pattern. For a quartered electrode pattern, the $\Gamma$ matrix is given by:

$$\Gamma = [\gamma_{ii}] = \begin{bmatrix} \int_{-\pi/4}^{\pi/4} f_1 d\theta - \int_{3\pi/4}^{5\pi/4} f_1 d\theta & \int_{\pi/4}^{3\pi/4} f_1 d\theta - \int_{5\pi/4}^{7\pi/4} f_1 d\theta & \int_0^{2\pi} f_1 d\theta \\ \int_{-\pi/4}^{\pi/4} f_2 d\theta - \int_{3\pi/4}^{5\pi/4} f_2 d\theta & \int_{\pi/4}^{3\pi/4} f_2 d\theta - \int_{5\pi/4}^{7\pi/4} f_2 d\theta & \int_0^{2\pi} f_2 d\theta \\ \int_{-\pi/4}^{\pi/4} f_3 d\theta - \int_{3\pi/4}^{5\pi/4} f_3 d\theta & \int_{\pi/4}^{3\pi/4} f_3 d\theta - \int_{5\pi/4}^{7\pi/4} f_3 d\theta & \int_0^{2\pi} f_3 d\theta \end{bmatrix} , \tag{3.39}$$

where functions $f_1$, $f_2$ and $f_3$ are defined by:

$$f_1 = \frac{(R_1^3 - R_2^3)\cos(\theta + \theta_\delta)}{3(R_1 - R_2)}, \tag{3.40}$$

$$f_2 = \frac{(R_1^3 - R_2^3)\sin(\theta + \theta_\delta)}{3(R_1 - R_2)}, \tag{3.41}$$

$$f_3 = R_o + \sqrt{\delta_x^2 + \delta_y^2}\cos(\theta - \theta_\delta) + \sqrt{R_i^2 - (\delta_x^2 + \delta_y^2)\sin^2(\theta - \theta_\delta)}. \tag{3.42}$$

The relevant geometrical parameters of the piezotube are defined in Figure 3.19.
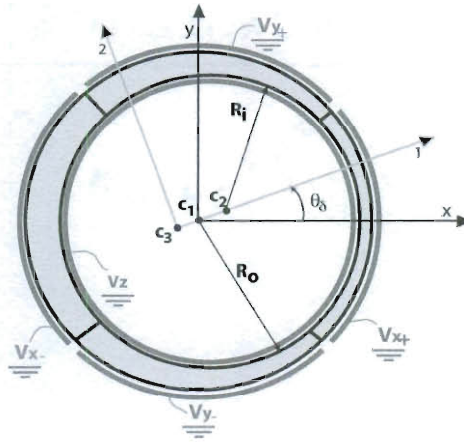


**Figure 3.19:** Piezotube geometrical properties

The tube eccentricities in the $x$ and $y$ directions are denoted by $\delta_x$ and $\delta_y$, respectively. The eccentricity angle is given by $\theta_\delta = \tan^{-1}(\delta_y/\delta_x)$. The radii $R_1$ and $R_2$ are given by:

$$R_1 = \bar{R}_o\cos(\theta - \theta_\delta) + \sqrt{R_o^2 - \bar{R}_o\sin^2(\theta - \theta_\delta)}, \tag{3.43}$$

$$R_2 = \bar{R}_i\cos(\theta - \theta_\delta) + \sqrt{R_i^2 - \bar{R}_i\sin^2(\theta - \theta_\delta)}, \tag{3.44}$$

where $\bar{R}_o = \sqrt{(\bar{x} + \bar{y})^2}$ and $\bar{R}_i = \sqrt{(\bar{x} - \delta_x)^2 + (\bar{y} - \delta_y)^2}$. $\bar{x}$ and $\bar{y}$ are the coordinates of the centroid of the tube relative to $c_1$.

In order to assess the properties of the $\Gamma$ matrix, we calculated its eigenvalues for a relevant range of the main parameters of the piezotube, namely the eccentricities and the internal and external radii. The proposed design implies a relatively small piezotube

diameter of the order of $1mm$ and thus eccentricities of the order of $5\mu m$. Varying these different parameters, we verified that the $\Gamma$ matrix is positive definite for the considered range. Figure 3.20 is a representative plot of the variation of the smallest eigenvalue of the $\Gamma$ matrix $\lambda_{min}$ for a range of the piezotube eccentricities from $1\mu m$ to $5\mu m$ for $R_i = 0.45mm$ and $R_o = 0.5mm$.
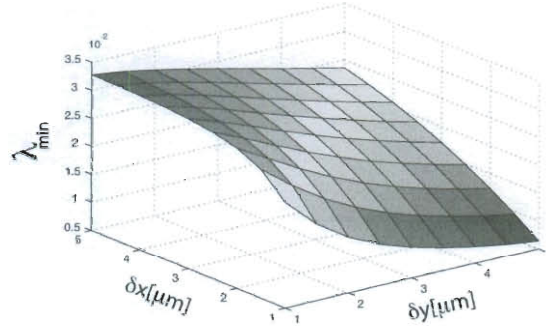


**Figure 3.20:** Effect of varying the tube eccentricities on $\lambda_{min}$

## 3.5.2 Disturbance Force

During manipulation tasks, the main disturbance force that affects the tip motion arises from the interactions with the substrate ever present at the nanoscale [43]. These interactions, due mainly to van der Waals forces, create a periodic potential distribution. The tip-substrate interactions can be described by an adiabatic potential $P(x,y)$ which has the symmetry of the surface [73]. Expanded in a two-dimensional Fourier series to the first order, $P$ is given by:

$$P = p_1[\cos(\frac{2\pi}{a}x) + \cos(\frac{2\pi}{a}y)] + p_2 \cos(\frac{2\pi}{a}x) \cos(\frac{2\pi}{a}y), \tag{3.45}$$

where $a$ is the substrate lattice constant. $p_1$ and $p_2$ are parameters that reflect the amplitude of the interactions that mainly depend on the material properties and the tip-substrate separation distance. The disturbance force is the gradient of the interaction potential.

Next, we will develop a singular perturbation model of the proposed probe dynamics. In addition, we will propose the use of composite control to improve the accuracy of the manipulation.

### 3.5.3    Singular Perturbation Model of The Probe

For the purposes of this section, we will neglect the effects of the disturbances ($F_d = 0$) and develop a singular perturbation model of the nanomanipulator [112, 113, 114]. We define a new variable $z = K_1(q_2 - q_1)$ that represents the oscillations transmitted through the tip holder. As discussed previously, it is realistic to assume that the tip-holder and the piezotube stiffnesses are large relative to the other parameters of the system during manipulation phases. We idealize this assumption by assuming that $K_1$ and $K_2$ are $O(1/\epsilon^2)$ where $\epsilon$ is a small parameter, so that we may write:

$$K_1 = \frac{K_1^*}{\epsilon^2}; \quad K_2 = \frac{K_2^*}{\epsilon^2}. \tag{3.46}$$

The choice of the proportionality constants is dictated by design considerations. It is well known in singular perturbation theory that the proper scaling of parameters is crucial to the successful implementation of the theory [115]. Roughly speaking, $\epsilon$ should be so that the proportionality constants are in the same range as other parameters in the system. At the same time, $\epsilon$ should be small enough to ensure that the transient response of the boundary-layer system, defined in the following analysis, is sufficiently rapid.

Under the preceding assumptions, the dynamic equations (3.37) are modified as follows:

$$\begin{cases} D\ddot{q}_1 + C\dot{q}_1 = z, \\ \epsilon^2 J\ddot{z} + (K_1^* + K_2^*)z = K_1^*(\Gamma u - K_2 q_1 - J\ddot{q}_1). \end{cases} \tag{3.47}$$

In this form, we clearly see how the piezotube dynamics drive the tip-holder system, and how the holder motion can excite the piezotube. The end-effector's position and velocity $(q_1, \dot{q}_1)$ are the "slow" variables while the piezotube's applied displacements and displacements rates $(z, \dot{z})$ are the "fast" variables. The second equation of the singularly

perturbed model (3.47) represents the fast system. When $\epsilon = 0$, which corresponds to an infinitely rigid probe, the aforementioned equation becomes:

$$\bar{z} = K^*(\Gamma u - K_2 q_1 - J\ddot{q}_1),\tag{3.48}$$

where $K^* = (K_1^* + K_2^*)^{-1}K_1^*$. It is important to mention that $K_1^*$, $K_2^*$ and $K_1^* + K_2^*$ are invertible by construction. Thus in addition to being dimensionless, matrix $K^*$ is invertible. From the first equation in (3.47), we obtain the slow reduced-order system:

$$(D + K^*J)\ddot{q}_1 + C\dot{q}_1 + K^*K_2 q_1 = K^*\Gamma u,\tag{3.49}$$

which is just the rigid model in terms of $q_1$.

Analyzing equation (3.49) without control, we observe that the tip-holder resonant modes are purely oscillatory and this, in fact, is largely the source of the problem associated with the cantilever flexibility for the proposed nanomanipulator design. Our control approach can be explained intuitively then as follows: a fast feedback control law is first designed to damp the oscillations of the fast variables $(z, \dot{z})$. Once the fast transients have decayed, the slow part of the system $(q_1, \dot{q}_1)$ should appear nearly like the dynamics of a rigid cantilever (3.49), which can then be controlled using any number of techniques. The idea of composite control is to set:

$$u = u_s(q_1, \dot{q}_1, t) + u_f(z, \dot{z}).\tag{3.50}$$

The term $u_s$ is the slow control, and $u_f$ is the fast control.

Based on the previous decomposition of the end-effector's dynamics, a reasonable choice for the fast control is

$$u_f = K_v(\dot{q}_1 - \dot{q}_2).\tag{3.51}$$

We choose $K_v$ as a constant matrix such that $K_v = O(1/\epsilon)$, that is:

$$K_v = \frac{1}{\epsilon}\Gamma^{-1}(K_1^*)^{-1}C^*,\tag{3.52}$$

where $C^*$ is O(1). The previous choice is legitimate since $\Gamma$ is positive definite, and thus invertible for the considered range of parameters. Substituting the composite control (3.51) and the expression (3.52) into (3.47), we obtain:

$$\begin{cases} D\ddot{q}_1 + C\dot{q}_1 = z, \\ \epsilon^2 J\ddot{z} + \epsilon C^*\dot{z} + (K_1^* + K_2^*)z = K_1^*(\Gamma u_s - K_2 q_1 - J\ddot{q}_1). \end{cases} \quad (3.53)$$

It is important to note that the addition of the fast control does not alter the slow system since at $\epsilon = 0$ the singularly perturbed system (3.47) reduces to (3.49). Thus, the design of the slow control $u_s$ is independent of the fast control. To control the slow reduced order system, we can use any number of techniques for the control of rigid cantilevers that guarantee exponential stability [112, 113, 114]. For the present problem, a reasonable choice is:

$$u_s = \Gamma^{-1}(K^*)^{-1}\left[K_p(q_1 - q_d) + K_d(\dot{q}_1 - \dot{q}_d)\right]. \quad (3.54)$$

Using Tikhonov's theorem [115], we may approximate the system of equations (3.53) by using a quasi-steady-state and a boundary layer system. The theorem assumptions require that matrices $C^*$ and $K_1^* + K_2^*$ be positive definite (which can be insured by construction as $K_1$ and $K_2$ are positive definite). As a result, the piezotube force $z(t)$ and the tip position $q_1(t)$ satisfy:

$$z(t) = \bar{z}(t) + \eta(\tau) + O(\epsilon), \quad (3.55)$$

$$q_1(t) = \bar{q}_1(t) + O(\epsilon), \quad (3.56)$$

for $t > 0$, where $\tau = t/\epsilon$ is the fast time scale, $O(\epsilon)$ denotes terms of order $\epsilon$ and higher, and $\eta$ satisfies the boundary layer equation:

$$J\frac{d^2\eta}{d\tau^2} + C^*\frac{d\eta}{d\tau} + (K_1^* + K_2^*)\eta = 0. \quad (3.57)$$

It follows that the nanomanipulator's governing equations can be written up to $O(\epsilon)$ as:

$$\begin{cases} D\ddot{q}_1 + C\dot{q}_1 = K_1^*\Gamma u_s + \eta(t/\epsilon), \\ J\frac{d^2\eta}{d\tau^2} + C^*\frac{d\eta}{d\tau} + (K_1^* + K_2^*)\eta = 0, \end{cases} \quad (3.58)$$

where $u_s$ is given by equation (3.54).

Next, we will simulate path tracking experiments of the probe to investigate the performances of the design and the proposed control.

## 3.5.4 Simulation Results

Crucial to all types of nanomanipulation tasks is the ability to accurately position the end-effector. In this section, we will simulate path tracking experiments of the proposed probe to assess the control performances. Figure 3.21 represents simulated tracking of a predefined conic path. The results show clearly the ability of the probe to describe controlled trajectories. The piezotube internal and external radii were set to $0.45mm$ and $0.5mm$, respectively. In addition, we assumed that $\delta_x = \delta_y = 5\mu m$.
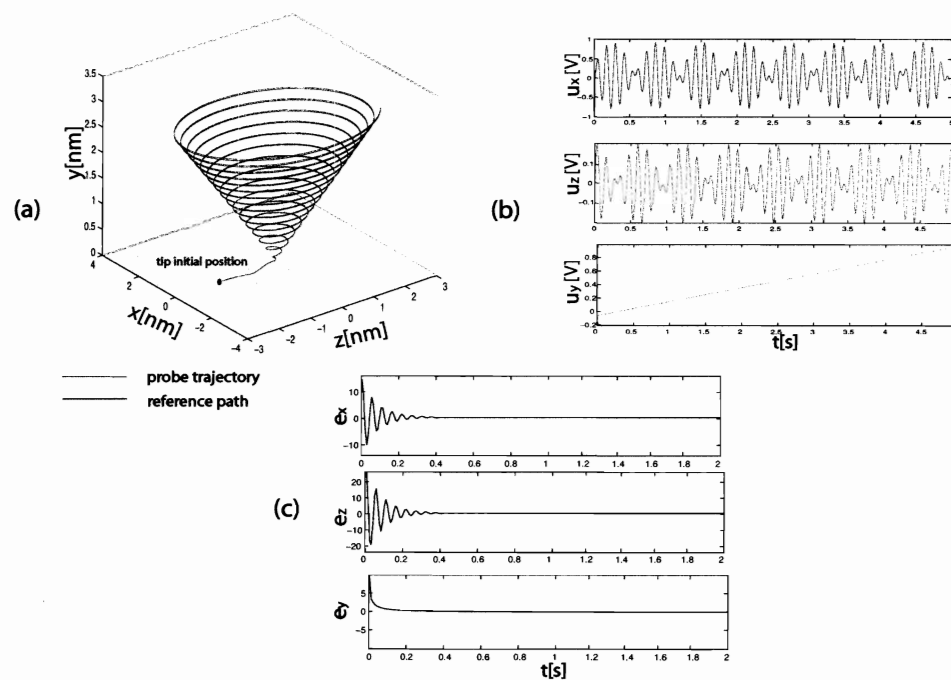


**Figure 3.21:** Conic path tracking (a) desired versus simulated trajectories (b) control effort (c) tracking errors

In order to achieve controlled motion, the system is actuated with three voltages: $u_x$, $u_y$ and $u_z$. The $u_x$ and $u_z$ voltage inputs actuate the horizontal motion of the tip, whereas $u_y$ causes its vertical displacements. Analyzing the tracking error plots, we conclude that the tracking performance is satisfactory. After a quick transient phase, the tracking error stays within 1% in the three directions. However, vertical displacements of the tip, corresponding to piezotube extensions along the $y$ axis are more accurate than displacements in the $x$ or $z$ directions.

To investigate the effects of the disturbances on the tracking performance, we run additional simulations that take into account the existence of the tip-substrate interactions. The simulation scenario consists of tracking a cylindrical trajectory where the axis of the cylinder is parallel to the substrate. We assumed that $KBr(100)$ is used as a substrate. The disturbance is given by equation (3.45) with $p_1 = 5.28e - 9Nm$, $p_2 = 1.056e - 9Nm$ and $a = 0.66nm$ taken from [73]. Simulation results with and without the disturbance effects are represented in Figure 3.22.
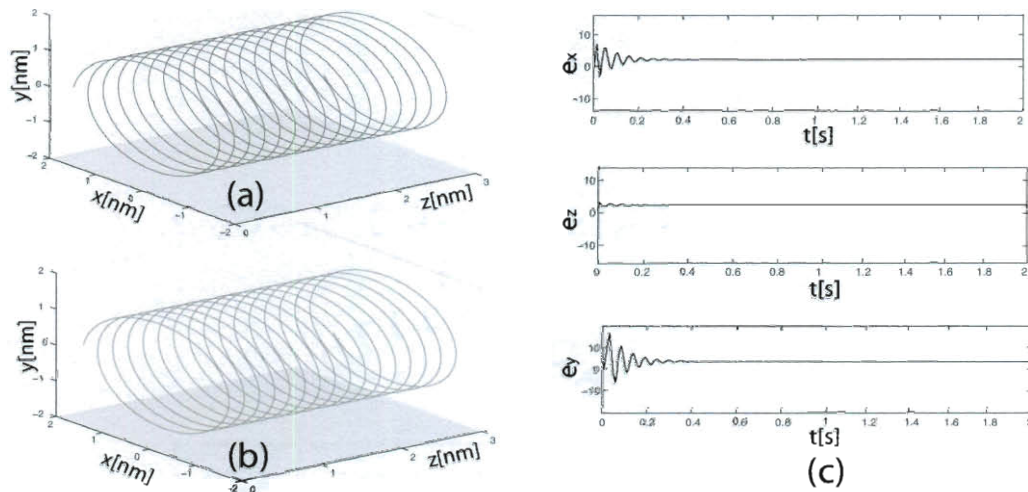


**Figure 3.22:** Cylindrical path tracking (a) without and (b) with disturbances (c) corresponding tracking error

Clearly, the tracking performance is satisfactory even when we take the disturbances into account. However, it is expected that more severe disturbances, arising from higher surfaces forces, can cause larger deviation and will require additional control to compensate for.

## 3.6   Conclusions

In the present chapter, two new designs of active probes suitable for manipulation were proposed. The first probe is based on a duo-biomorph to allow for local tip motion in the vertical and lateral directions. The design is perfect for nanomachining vertical surfaces and controlled load nano-lithography. The second design employs a horizontal piezotube to allow for true maneuverability and 3D motion of the tip. Both proposed probes include a frontal piezolayer used to tune the cantilever stiffness in-situ. This feature is essential as stiff probes are needed for effective manipulation tasks, while complaint cantilevers are required for increased force sensitivity. The probes are also capable of simultaneous actuation and sensing of the tip motion insuring true maneuverability. Using the adopted modeling of the physics and the advanced capabilities of the new probes, improved nanomanipulation schemes can be developed.

# Chapter 4

# Mechanical Nanomanipulation Schemes

In the previous chapters, throughout analysis and modeling of the relevant nanoscale physics and mechanics were conducted. In addition, new smart probes allowing for simultaneous actuation and sensing of the tip motion were introduced. The integration of the improved modeling and tools into nanomanipulation schemes is expected to yield unprecedented accuracy and repeatability. In the present chapter, we will analyze the following probe-based schemes that can be used to manipulate matter at the nanoscale:

- **Nano-Pushing:** It consists of applying mechanical forces by the tip to move and position nano-samples in desired locations. The gained knowledge on path tracking can be exploited to perform controlled load lithography using relatively hard tips (made of diamond for instance).

- **Nano-Placing:** Nano-pushing is slow and requires atomically flat substrates. We propose a new manipulation scheme that we will refer to as vibrational nano-placing. In nano-placing, adhesion and sticking effects are used to capture nano-samples. The vibration of the probe is then explored to achieve controlled release of the sample. The advantages of this manipulation scheme include fast speeds, parallel operation and reduced effect of substrate topography.

Combining nano-pushing and nano-placing techniques can decrease dramatically the time required to arrange nano-samples into useful devices. Next, we will analyze these manipulation schemes and use the previously adopted physics and mechanics to develop corresponding advanced modeling.

79

# 4.1 Nano-Pushing

## 4.1.1 Description

In a typical nano-pushing task, a spherical nano-sample is pushed on a flat substrate (Figure 4.1). The relevant physics are the friction with the substrate and the tip-sample interactions. In order to represent these physics, the advanced modeling developed in Chapter 2 will be used. The efficacy of the resulting nano-pushing model will be investigated through simulation. The adopted manipulation scenario is as follows: a nano-sample is deposited on an atomically flat substrate. The probe tip is then aligned near the sample along the pushing axis $x$. Since the tip diameter is smaller than the sample diameter, there will be a gap between the tip and the substrate. The nanomanipulation is assumed to be carried out in UHV with proper electrical grounding.
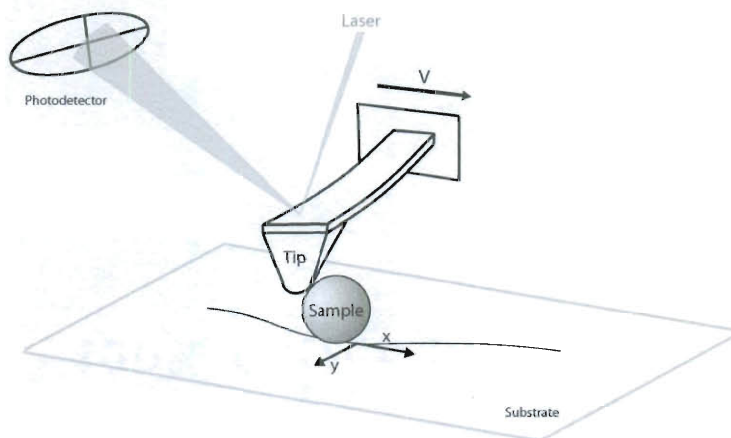


**Figure 4.1:** Probe-based nano-pushing

The model implementation was realized using the MATLAB solver *ode23tb*. The relative and absolute tolerances of the solver were set to $1e-2$ and $1e-15$, respectively. We choose the arbitrarily tip and sample initial positions $(x_t, y_t) = (0, 0)$ and $(x_s, y_s) = (4e-10, 4e-10)$. The remaining initial conditions including the initial velocities and the initial bristle deflections were set to zero. In addition, the AFM probe base pushing speed

is assumed to be constant and equal to $V = 3\mu m/s$. The material and geometrical probe properties, used to deduce the simulations parameters listed in Table 4.1, are common values of contact mode experiments.

**Table 4.1:** Nano-pushing simulations parameters

| PARAMETER | VALUE | PARAMETER | VALUE | PARAMETER | VALUE |
|---|---|---|---|---|---|
| $\sigma_0$ | 1e4 N/m | $m_s$ | $4e-17$ kg | $k_{tx}$ | 30N/m |
| $m_{tx}$ | $1.98e-18$ kg | $m_{ty}$ | $1.98e-18$ kg | $k_{ty}$ | 10 N/m |
| $\nu_t$ | 0.33 | $E_t$ | 200 GPa | $R_t$ | $50e-9$ m |
| $\nu_s$ | 0.33 | $E_s$ | 0.27 GPa | $R_s$ | $160e-9$ m |
| $H$ | $1.452e-20$ J | $c_t$ | $7e-9$ N.s/m | $V_s$ | $1e-5$ m/s |

The substrate materials used in the simulations are the Muscovite Mica and the Highly Ordered Pyrolytic Graphite (HOPG). Both materials have an hexagonal lattice structure, but different lattice parameters $a$. Mica and HOPG are widely used as substrates in nano-pushing experiments because they can be cleaved into atomically flat surfaces. FFM experiments for both materials were conducted to determine the different parameters of the friction model (Table 4.2). The simulation results reported in the next section correspond to two main scenarios. In the first one, the case where the pushing axis coincides with the main axis of the substrate is investigated. In the second scenario, we focus on the general case of 2D tip motion.

**Table 4.2:** Substrate properties used in nano-pushing simulations

|  |  | MICA | HOPG |
|---|---|---|---|
| LATTICE PARAMETER | $a$ | $5.19\mathring{A}$ | $2.55\mathring{A}$ |
| FRICTION MODEL PARAMETERS |  |  |  |
|  | $F_{si}$ | $2.2e-9$ N | $1.2e-9$ N |
|  | $F_{ci}$ | $6e-10$ N | $5e-10$ N |

## 4.1.2 Simulations

The lumped-parameter approach is used to model the probe. The complete nano-pushing model includes also the tip-sample interactions and the sample-substrate friction. It is expected that the resulting friction force possesses a sawtooth characteristic with the periodicity of the lattice and that the sample motion presents periodic jumps.

### 4.1.2.1 1D stick-slip phenomenon

In this case, the pushing axis coincides with the main lattice axis of the substrate. The simulation results describe the sample motion as series of straining and relaxing events. The sample motion consists in fact of instantaneous jumps between respective sticking points (Figure 4.2-a). This corresponds to a stairs-like characteristic where individual step length is around $a$. Figure 4.2-b shows clearly that the developed model predicts the sawtooth property of nano-friction. Comparing the results corresponding to Mica and HOPG substrates, we conclude that, through the implementation of the proposed jumping criterion, the nano-pushing model succeeded in reproducing the 1D stick-slip behavior with the periodicity of the substrate lattice.
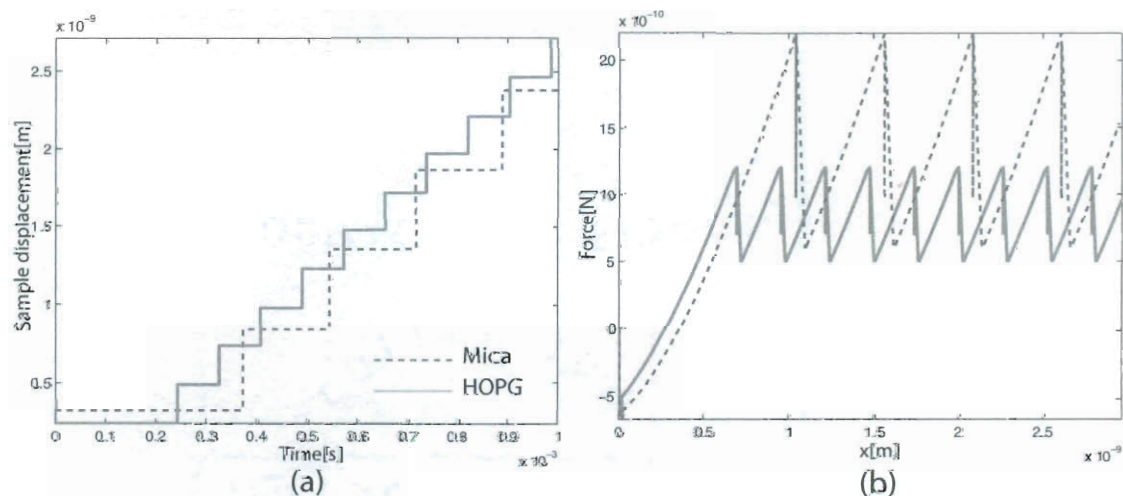


**Figure 4.2:** 1D stick-slip phenomenon (a) sample motion (b) friction force

The obtained results are in agreement with experimental observations reporting that the stick-slip behavior is dominant at low pushing speeds. However, for relatively high velocities the sample motion is expected to become continuous. In order to investigate the transition from discontinuous to continuous motion, we rerun the simulations for a relatively high pushing velocity $V = 150\mu m/s$. As shown in Figure 4.3, our model succeeded in describing the continuous motion of the sample and reproducing a constant friction force. According to Figure 4.3-b when the static friction value is reached, the friction becomes constant and equal to the kinetic friction. The regime of continuous sample motion is interesting from a practical point of view as it reduces the effects of undesired oscillations on the manipulation outcome. However, the majority of current implementations of AFM-based nano-pushing operate in a speed range where stick-slip is dominant due to hardware limitations.
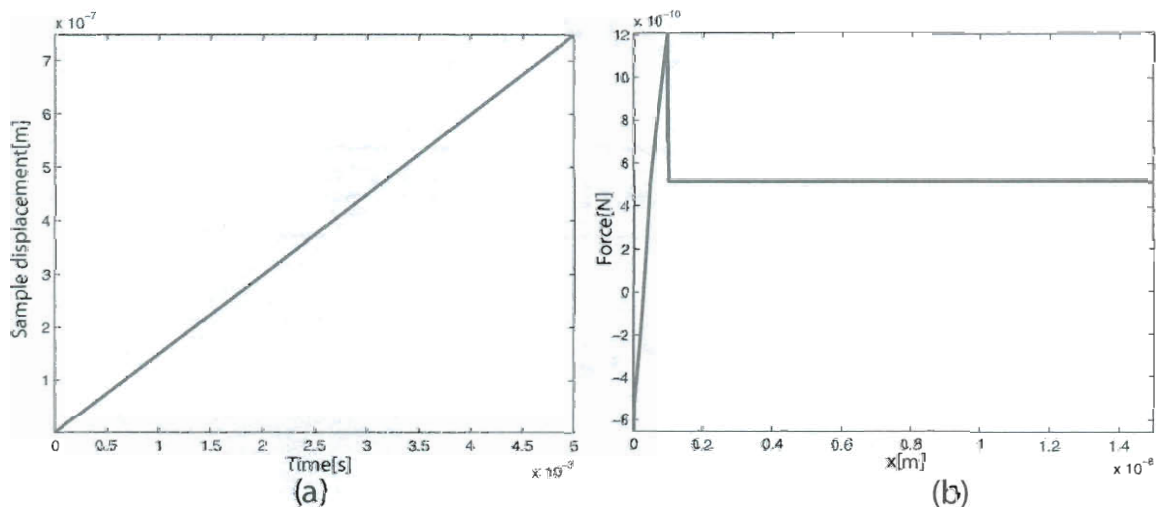


**Figure 4.3:** High speed nano-pushing (a) sample motion (b) friction force

As our model does not impose restrictive contact conditions, it is interesting to analyze the obtained characteristics of the initial collision impact. All the conducted simulations reflect the existence of an initial sticking phase where the applied forces cannot move the sample until the static friction value is reached. This phenomenon is commonly referred

to as the pre-sliding condition. Additional simulations show that changing the value of the effective inter-atomic distance **affects** the pre-sliding condition (Figure 4.4). This result can be explained by the fact that the pre-sliding regime characterizes the magnitude of the interactions between the **sample and substrate** materials.
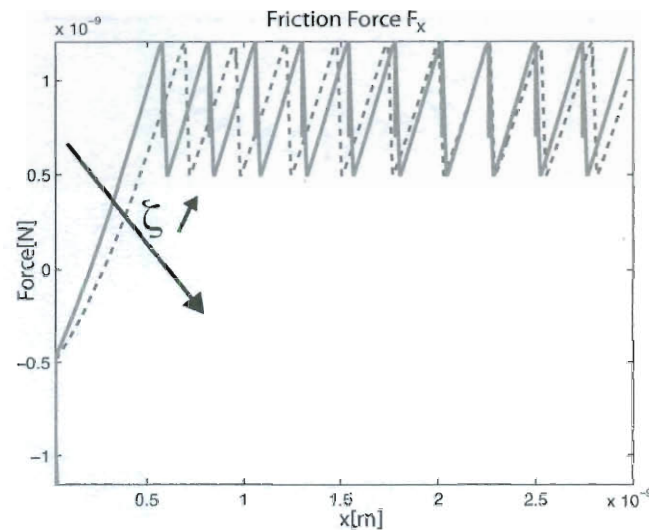


**Figure 4.4:** Effect of the inter-atomic distance

### 4.1.2.2  2D stick-slip phenomenon

In the following simulations the complete 2D nanomanipulation model is used. The pushing speed is set to $V = 3\mu m/s$. The simulations will focus on the case where the interactions between the tip, sample and substrate induce a 2D motion of the sample. This generally occurs if the scan axis does not coincide with the main substrate lattice axis. In Figure 4.5, we plot the obtained $x$ and $y$ coordinates of the sample displacements. The results show that the sample undergoes a zigzag motion. This motion is driven by the instantaneous jumps of the probe tip between sticking positions. Being able to describe and monitor the 2D motion of the sample is essential towards building more advanced haptic interfaces for manipulation.
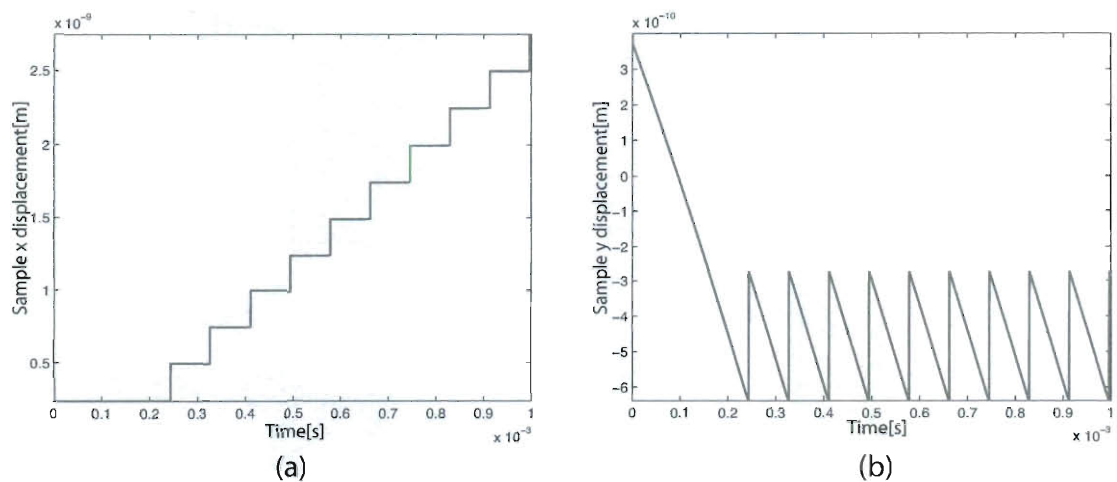
**Figure 4.5:** Nano-sample displacements in the (a) $x$ and (b) $y$ directions

All the previous simulations were conducted assuming that the manipulation is achieved in UHV. Experimental investigations in ambient conditions show that the main properties of nano-friction are conserved. However, the operation in air leads to more irregularities in the sample motion and sawtooth characteristic. The adopted nano-pushing model can accommodate the effects of capillary forces through the viscous friction terms (Figure 4.6).
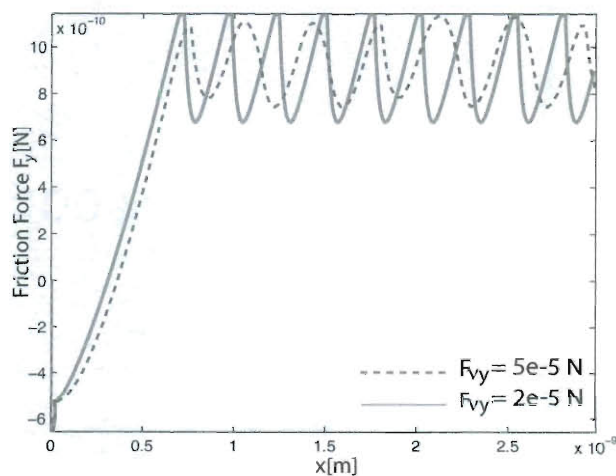


**Figure 4.6:** Effect of the viscous friction on the sawtooth characteristic

In Figure 4.6, we superposed the friction force obtained for $F_{\nu y} = 2e-5N$ and $F_{\nu y} = 5e-5N$. Increasing the value of the viscous friction, we note that the sawtooth characteristic is more distorted towards a square-wave like shape. This is in agreement with the experiments reported in [63].

In conclusion, simulations show that the main characteristic of nano-pushing is a stick-slip behavior arising from the sample-substrate interactions. This behavior depends mainly on the pushing speed and substrate lattice structure. A deeper understanding of the zigzag motion of the tip and the transitions from discrete jumps to continuous motion is needed. In the next section, nonlinear analysis techniques will be used to study the occurrence and evolution of stick-slip in nano-pushing. Emphasis will be given to investigate the effects of the manipulation speed and loading force. The obtained results bear important information that can help improve nano-pushing manipulation through the proper selection of these parameters.

## 4.1.3 Analysis of Stick-Slip During Nano-Pushing

For the purpose of this section, a simple nano-pushing model is developed to analyze the stick-slip behavior (Figure 4.7). The structural characteristics of the probe tip will be denoted by $m_1$, $k_1$ and $c_1$. $m_2$ and $k_2$ represent the sample mass and the tip-sample contact stiffness, respectively. The linear approximation of the tip-sample interactions is only valid for small tip-sample separation distances [116]. The damping coefficient $c_2$ is introduced to take into account the effect of the phonon dissipation. The sample-substrate interaction potential will be approximated to the first order by:

$$U = U_0 \cos\left(\frac{2\pi}{a}X\right) \tag{4.1}$$

where $U_0$ is the amplitude of the interactions which depends mainly on the loading force. The corresponding force is given by the gradient of this potential in the $X$-direction. Simulations show that the first order approximation is sufficient to predict the characteristics of these interactions for different materials [36].
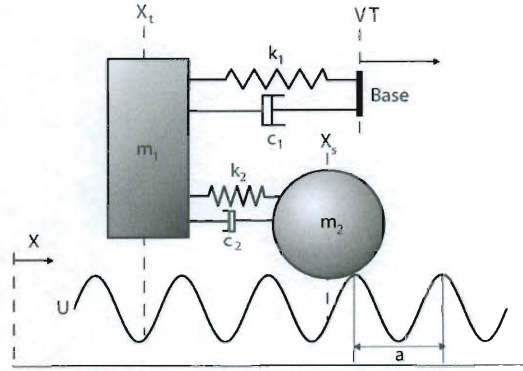
**Figure 4.7:** Simplified model of AFM-based nano-pushing

The governing equations of the system can be written in the form:

$$
\begin{cases}
m_1 \frac{d^2 X_t}{dT^2} = -c_1(\frac{dX_t}{dT} - V) - c_2(\frac{dX_t}{dT} - \frac{dX_s}{dT}) - k_1(X_t - VT) - k_2(X_t - X_s), \\
m_2 \frac{d^2 X_s}{dT^2} = -c_2(\frac{dX_s}{dT} - \frac{dX_t}{dT}) - k_2(X_s - X_t) + \frac{2\pi U_0}{a} \sin(\frac{2\pi}{a} X_s).
\end{cases}
\tag{4.2}
$$

$X_t$ and $X_s$ are the coordinates of the tip and sample, respectively. $T$ denotes the time variable and $V$ represents the manipulation speed. In order to avoid numerical problems when integrating the above system, we adopt the non-dimensionalization procedure proposed by Conley et al. [77]. A new time variable $t$ is defined by:

$$
t = \sqrt{\frac{k}{m}} T,
\tag{4.3}
$$

such that

$$
\dot{s} = \frac{ds}{dt} = \sqrt{\frac{m}{k}} \frac{ds}{dT}.
\tag{4.4}
$$

where $m$ and $k$ denote the effective mass and stiffness coefficients of the tip-sample system given by:

$$
m = \frac{m_1 m_2}{m_1 + m_2}, \qquad k = \frac{k_1 k_2}{k_1 + k_2}.
\tag{4.5}
$$

We then scale the $X$ axis and change the frames using the following change of variables:

$$
y_1 = \frac{2\pi}{a} X_t - vt, \qquad y_2 = \frac{2\pi}{a} X_s - vt,
\tag{4.6}
$$

where $v = \frac{2\pi}{a}\sqrt{\frac{m}{k}}V$. This change of variables is equivalent to attaching moving frames to the tip and nano-sample. Substituting the new space and time variables in the system of equations (4.2), we obtain the following non-dimensional governing equations:

$$\begin{cases} \frac{m_1}{m}\ddot{y}_1 = -2\zeta_1\dot{y}_1 - 2\zeta_2(\dot{y}_1 - \dot{y}_2) - \frac{k_1}{k}y_1 - \frac{k_2}{k}(y_1 - y_2), \\ \frac{m_2}{m}\ddot{y}_2 = -2\zeta_2(\dot{y}_2 - \dot{y}_1) - \frac{k_2}{k}(y_2 - y_1) + u_0\sin(y_2 + vt), \end{cases}$$ (4.7)

where $\zeta_1 = \frac{c_1}{2\sqrt{km}}$, $\zeta_2 = \frac{c_2}{2\sqrt{km}}$ and $u_0 = \frac{4\pi^2}{ka^2}U_0$. Equations (4.7) can be written in the state space form:

$$\dot{\underline{x}} = \underline{f}(\underline{x}, t),$$ (4.8)

where the state vector $\underline{x}$ is given by:

$$\underline{x} = [x_1 \quad x_2 \quad x_3 \quad x_4]^T = [y_1 \quad \dot{y}_1 \quad y_2 \quad \dot{y}_2]^T.$$ (4.9)

Unless otherwise stated, the numerical values used in the simulations of the next sections are those given in Table 4.3. The choice of the damping coefficient $\zeta_1$ is motivated by different experimental results which reported that the AFM probes operating in contact mode are underdamped [70]. We will also use a critical damping coefficient $\zeta_2 = 1$ to emphasize the effect of capillary forces and phonon dissipation in the substrate.

**Table 4.3:** Parameters used in investigating stick-slip behavior during nano-pushing

| PARAMETER | VALUE | PARAMETER | VALUE | PARAMETER | VALUE |
|---|---|---|---|---|---|
| $m_1$ | $2e{-}11\ kg$ | $k_1$ | $1\ Nm^{-1}$ | $\zeta_1$ | 0.1 |
| $m_2$ | $2e{-}12\ kg$ | $k_2$ | $1e{-}5\ Nm^{-1}$ | $\zeta_2$ | 1 |

Next, low and fast speed manipulation dynamics will be analyzed. The results show the existence of a transition from no stick-slip to a complex range of stick-slip behaviors as the speed increases. In addition, simulation reveals the possibility of hysteresis when the sample is pushed to the left or to the right.

### 4.1.3.1 Low speed manipulation dynamics

Slow manipulation refers to pushing speeds in the range of $10-100$ $nm/s$. For this speed range, the tip-sample dynamics correspond to the quasi-static equilibrium of equations (4.7). The quasi-static solution is given by:

$$\underline{x}_{v\ll 1} = \left[ \frac{k_2}{k_1 + k_2}X \quad 0 \quad X \quad 0 \right]^T, \tag{4.10}$$

where $X$ satisfies the equality:

$$X = u_0 \sin(X + \psi). \tag{4.11}$$

$\psi$ denotes the quasistatically varying phase of the sample motion. The above equation arises also in the analysis of slow speed FFM experiments where it was related to multi-valued friction at low speeds [117, 77]. In this section, we will study the quasistatic solution from the perspective of understanding the sample dynamics during low speed nano-pushing. The corresponding tip motion can be deduced using equation (4.10). The $\frac{k_2}{k_1+k_2}$ ratio shows that the cantilever stiffness significantly affects the system dynamics which is in agreement with experimental observations [52]. For a given value of $\psi$ and $u_0$, equation (4.11) may have one or more stable solutions and none, one or more unstable solutions. The stability can be determined using Lagrange-Dirichlet theorem by examining the sign of:

$$L(X) = 1 - u_0 \cos(X + \psi). \tag{4.12}$$

Stable and unstable solutions correspond to nodes and saddle points in the sample phase space, respectively. In Figure 4.8, we plotted the solution of equation (4.11) for $u_0 = 0.5$, $u_0 = 6$ and $u_0 = 25$ which correspond to values of $U_0$ ranging from $10^{-2}ev$ to $1ev$ (continuous lines denote stable solutions whereas dashed lines represent unstable solutions). The corresponding sample phase space plots obtained for $\psi = 5$ are represented in the left half side of the same figure. Clearly, for $u_0 \leq 1$ equation (4.11) admits a unique solution for each value of $\psi$. This solution is stable and corresponds to one possible motion of the sample. No hysteresis will occur if the tip is pushed to the right or to the left.
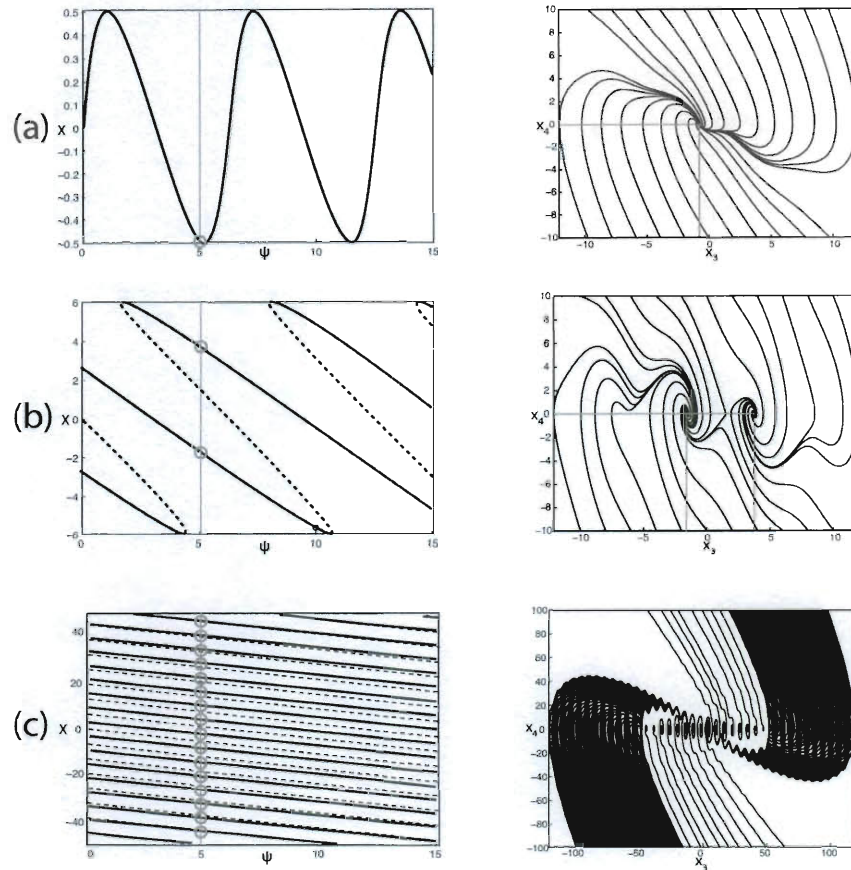
**Figure 4.8:** Quasistatic solutions of equation (4.11) for: (a) $u_0 = 0.5$ (b) $u_0 = 6$ (c) $u_0 = 25$ and corresponding sample phase plots for $\psi = 5$

However for $u_0 > 1$, which corresponds to higher loading forces or higher interactions between the sample and substrate, hysteresis occurs. In fact, for $u_0 > 1$ multiple solutions of the aforementioned equation exist resulting in different paths of the sample as the AFM cantilever base is moved to the right or to the left. For increased values of $u_0$, the dynamics of the sample become more complicated. It is informative to look at the changes in the sample phase space as $u_0$ increases. These plots represent trajectories in the $(x_3, x_4)$ domain obtained by integrating the governing equations for different initial conditions. Positive and negative $x_3$ values correspond to the sample moving in front or lagging behind the cantilever base, respectively.

All plots include at least one stable node to which the different trajectories of the sample converge. As predicted by solving the quasistatic equilibrium equation (4.11), the phase plot nodes correspond to $x_4 = 0$ which reflects steady regimes where the sample moves with the same speed as the probe base. However, before that regime is reached the sample may move with a speed which is faster than the input speed. These fast sample dynamics are the result of the sample-substrate interactions. Unstable solutions, represented by saddles points, separate trajectories between nodes (Figure 4.8). The creation of a new node is accompanied by the creation of a new saddle point. Increasing further the value of $u_0$, more complicated dynamics arise. For the particular value of $u_0 = 25$ which corresponds to $U_0 \sim 1ev$, the phase plot includes 16 nodes and 15 saddle points (Figure 4.8-c). Predicting the motion of the sample and the possible transitions require advanced numerical techniques. However as it is clear from the aforementioned figure, some of these nodes are more attractive than others. This motivates the analysis of the basins of attractions in the $(x_3(0), x_4(0))$ domain. In Figure 4.9, the sample basins of attraction for $u_0 = 8$ (Figure 4.9-a) and $u_0 = 20$ (Figure 4.9-b) are represented.
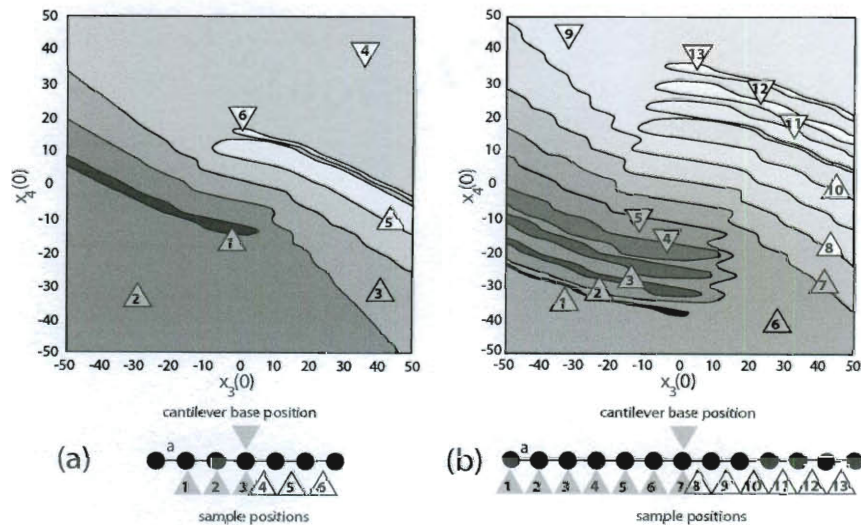


**Figure 4.9:** Basins of attraction of the sample motion for $\psi = 5$ and (a) $u_0 = 8$ (b) $u_0 = 20$

The different domains correspond to possible steady sample-base separation distances during the pushing manipulation. As noted before, the structure of the plots shows that two basins are more attractive than the others. For instance, the steady states labeled by 2 and 4 dominate the sample motion for $(u_0, \psi) = (8, 5)$. These domains correspond to the sample being behind or in front of the probe base and are symmetric with respect to the central domain. For increased values of $u_0$ more basins corresponding to increased separation distances appear. However, the characteristic structure of the plot is conserved: two dominant basins symmetric with respect to the base position (domains 6 and 9 in Figure 4.9-b). Analyzing the slow speed dynamics of AFM-based nano-pushing, clearly shows the effects of the relevant interactions on the sample motion and thus the manipulation outcome. Increased interactions lead to more complex dynamics that make repeatable operation very difficult.

The discussion this far has focused on the quasistatic dynamics that correspond to manipulation speeds in the range of $10nm-100nm$. With current improvements to AFM positioning systems, speeds in the range of $1\mu m/s-100\mu m/s$ can be achieved. More recently, faster positioning techniques that allow for manipulation speeds up to $5mm/s$ were proposed [118]. Next, fast speed nano-pushing will be analyzed.

### 4.1.3.2 High speed manipulation dynamics

In this section, the original system of governing equations (4.7) is integrated numerically. Both time scales corresponding to the uniform sliding of the AFM base and to the sample oscillations are taken into account. The main parameters that affect the sample motion are the pushing speed $v$ and amplitude of the interactions. It is expected that for speeds of the order of $10\mu m/s$ the sample will experience a stick-slip motion. Sample phase plots for pushing speeds $V = 3\mu m/s$, $V = 30\mu m/s$ and $V = 0.3mm/s$ are represented in Figure 4.10. For relatively slow manipulation speeds (Figure 4.10-a), the structure of the phase plot is similar to the corresponding one in the quasistatic regime. However, an interesting phenomenon takes place where a sudden jump of the sample occurs (Figure

4.10-d). This is related to the emergence of short time dynamics caused by the periodic substrate interaction potential. Increasing the pushing speed to $V = 30\mu m/s$, a limit cycle appears in the sample phase space (Figure 4.10-b). The limit cycle reveals a periodic motion of the sample that includes strain and relaxation phases. This proves in fact the occurrence of the stick-slip behavior. For fast manipulation velocities in the order of $mm/s$, the periodic behavior disappears giving place to a uniform sliding of the sample with the same velocity as the AFM base (Figure 4.10-c and Figure 4.10-f).
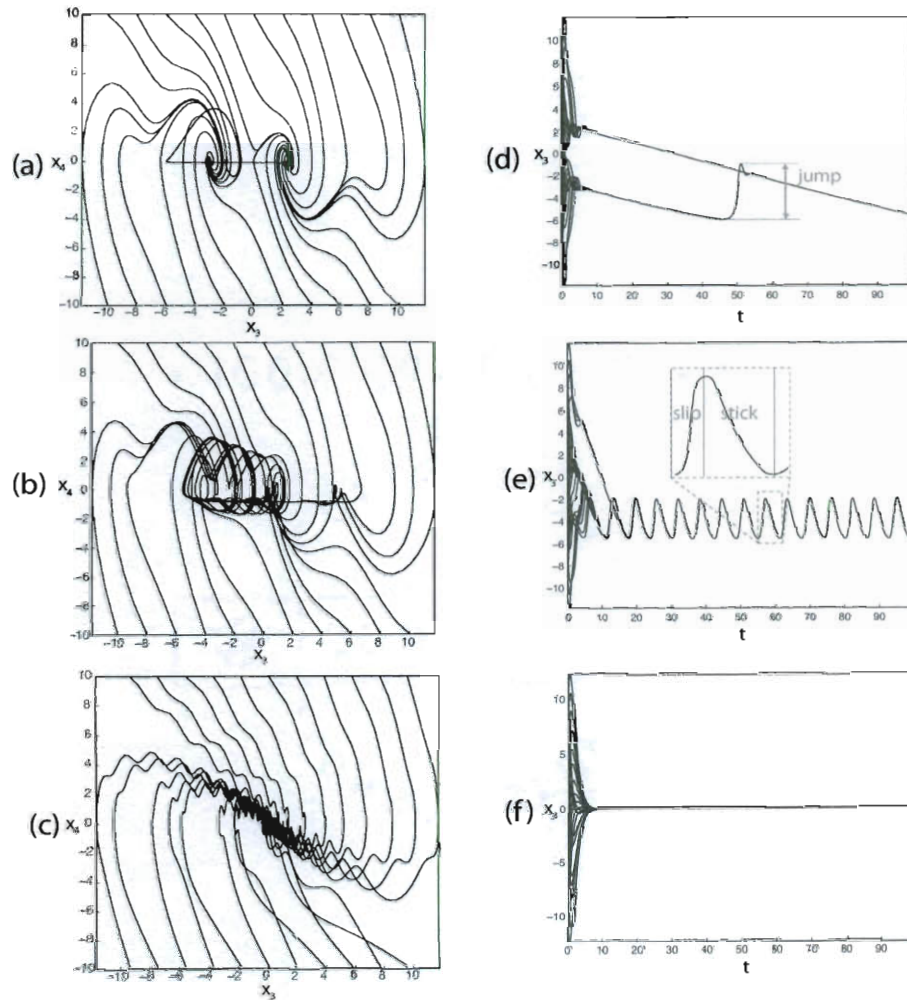


**Figure 4.10:** Phase portraits and corresponding sample position time variations for $u_0 = 3$ and (a),(d) $V = 3\mu m/s$ (b),(e) $V = 30\mu m/s$ and (c),(f) $V = 0.3mm/s$

In order to investigate the transition from stick-slip to uniform sliding, we represented the limit cycles obtained for $u_0 = 3$ and increased pushing speeds (Figure 4.11). The range of considered speeds spans from $\mu m/s$ to $mm/s$. Clearly, changing the manipulation speed affects the shape of the limit cycle. As the speed is increased, the limit cycle is contracted. In addition, the center of the limit cycle approaches the center of the phase plane reflecting a higher coupling between the tip and sample motions. In fact, smaller attractors correspond to shorter sample-base separation distances. For relatively fast pushing speeds, the limit cycle is reduced to a node. This corresponds to the steady sliding regime.
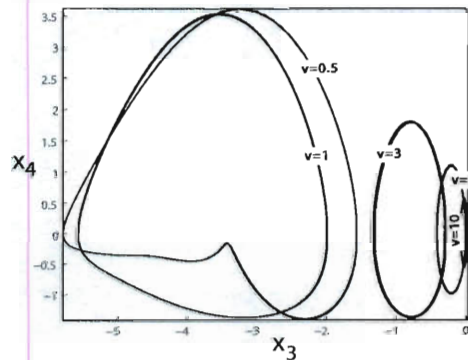


**Figure 4.11:** Limit cycles for $u_0 = 3$ corresponding to increased values of $v$

For increased values of $u_0$ multiple stick-slip regimes coexist. In Figure 4.12, we represented the projection of the possible steady state sample positions (denoted by $x_3^*$) as the value of $u_0$ is increased. The results corresponding to the quasistatic (Figure 4.12-a) and fast manipulation (Figure 4.12-b) regimes are represented in the same figure to analyze the change in the dynamics of the sample as the speed increases. Branches in the plot correspond to the different possible steady state values obtained for different initial conditions. The widening of these branches for fast manipulation speeds corresponds to the occurrence of stick-slip. The case of the quasistatic regime represented by Figure 4.12-a corresponds to a symmetric characteristic with equally spaced branches.

(a)                                    (b)
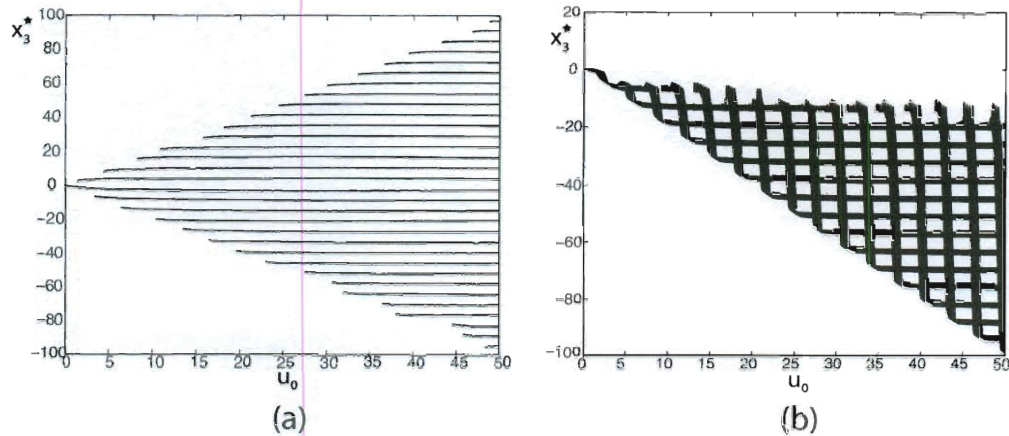
**Figure 4.12:** Steady state sample coordinate corresponding to (a) quasistatic regime and (b) fast regime dynamics

The spacing is correlated with the substrate lattice parameter $a$. As the value of $u_0$ increases, new branches appear corresponding to additional possible steady values of the sample-base separation distance. This result is to relate to the basins of attraction plots in Figure 4.9. In the case of fast manipulation speeds (Figure 4.12-b), the structure of equally spaced branches is conserved. The vertical connections between the branches represent transitions from different stick-slip regimes. Interestingly, only branches corresponding to negative values of $x_3^*$ remain compared to the quasistatic regime. These correspond to the sample lagging behind the AFM probe base. This shows again that for increased pushing speeds the coupling between the tip and sample motion increases.

Figure 4.13 summarizes the most important results on the occurrence and evolution of the stick-slip behavior during AFM-based nano-pushing manipulation. According to the previous analysis, a complex range of stick-slip behaviors can emerge during nano-pushing. The boundaries between the different regions depend on many factors including the material properties of the probe. For practical applications, the quasi-static regime is not of real interest. However, the regime of very fast manipulation speeds presents the advantage of reduced effects of the undesired oscillations.
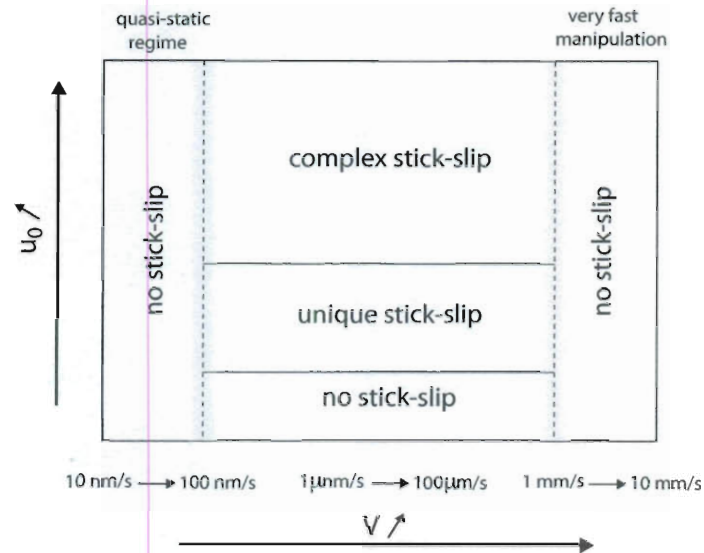
**Figure 4.13:** Evolution of the characteristics of nano-friction

In summary, nano-pushing manipulation, with the proper selection of the different parameters and the use of the advanced capabilities of the proposed probes, is very promising. However, this manipulation technique suffers two limitations that must be addressed to be commercially viable. These are the slow operation of current implementations and the severe restrictions on the flatness of the substrate. To address these limitations, we proposed a new manipulation scheme, labeled vibrational nano-placing, that exploits the interactions at the nanoscale to move samples over relatively long distances.

## 4.2 Nano-Placing

In the present section, we will introduce a new nanomanipulation scheme that we will refer to as vibrational nano-placing or in short nano-placing. The proposed approach is based on a similar technique used to arrange samples at the micro-scale. However, nano-placing explores the probe oscillations to achieve controlled release phase.

## 4.2.1 Micro-Placing

The most common probe-based manipulation schemes use mechanical forces to push and arrange samples [119, 30, 16, 120]. However these schemes suffer from undesired oscillations resulting from tip-sample interactions and sample-substrate friction. In fact, irregular substrate topography may even lead to the failure of the manipulation task. A new manipulation scheme, proposed to manipulate matter at the micro-scale, relaxes the requirement on the substrate flatness and promises faster operation. This scheme is referred to as *capture-release* or *micro-placing* manipulation [121, 122]. In micro-placing, the probe is brought into contact with micro-scale samples to achieve the capture phase. After reaching the desired position the cantilever is tilted in order to release the sample (Figure 4.14). Generalizing this technique to nanoscale samples faces the impossibility of releasing the sample because of the importance of adhesion forces at the nanoscale.
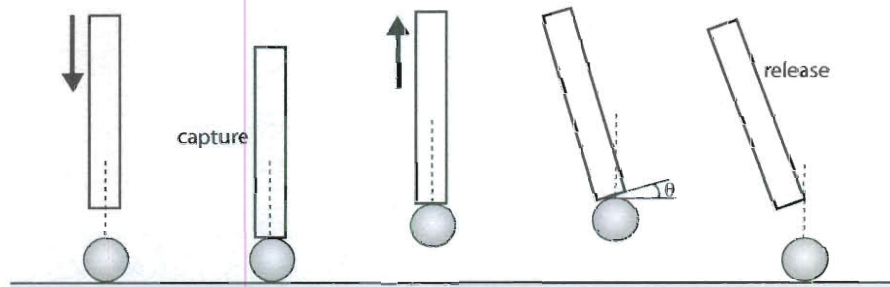


**Figure 4.14:** Micro-placing manipulation

In order to get more control on the release phase, researchers proposed the use of vibrating cantilevers. The sample is released by tuning the amplitude and frequency of the probe vibrations. Experimental studies validating this approach for micro-scale objects were reported [123]. However, applying this technique to manipulate nanoscale samples presents the complication of difficult and uncontrolled release phase. Streator [124] showed that dynamic oscillations affect the pull-off forces and modify the contact characteristics. Fang and Tan [125] introduced a modified contact model where interaction

forces do not depend only on the contact displacement distance, but also on the rate at which this distance changes. Clearly, these dynamic effects need to be taken into account in vibrational nano-placing. In the following, we will study vibrational placing manipulation and investigate its generalization to nano-samples. Emphasis will be given to analyze the effects of the probe oscillations and the relevant interaction forces on the manipulation. Simulations will be conducted to help tune the release phase parameters in order to achieve the desired positioning accuracy.

## 4.2.2 Vibrational Nano-Placing

Vibrational nano-placing uses adhesion forces to manipulate matter at the nanoscale. Sticking effects are used in order to capture the nano-sample. This implies a proper choice of the probe and sample materials [122]. After being transported to the desired position, the sample is released by increasing the cantilever oscillations (Figure 4.15). The release phase is crucial and requires sub-nanometer precision. As mentioned in the second chapter, the MD contact model is adopted to characterize the contact forces. This choice is motivated by the fact that the MD model can be applied to a wide range of tip-sample characteristics. In addition, the effect of short range attractive van der Waals forces will be taken into account during non-contact phases.
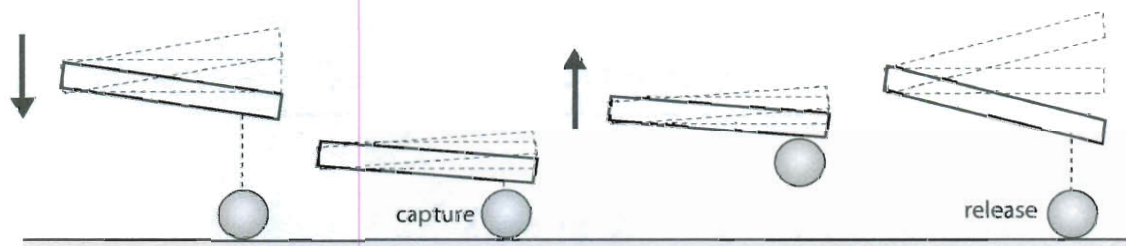


**Figure 4.15:** Vibrational AFM-based nano-placing

The manipulation task can be subdivided into three phases: the approach, the capture and the release phases. In the following, the analysis of the probe oscillations during these

different phases will be shown to give important feedback about the manipulation.

**Approach phase:** The probe is approached of the sample. The constitutive material of the manipulator is chosen to allow the capture. During this phase, the cantilever, which undergoes small amplitude oscillations, can be modeled as a 1 d.o.f mass and spring system (Figure 4.16). A damper represents the effect of the molecular vibration damping. The motion of the vibrating cantilever is affected by the interactions with the sample. The equation of motion of the cantilever oscillating at an arbitrary position $z_0$ from the sample is given by:

$$m\ddot{z} + \mu\dot{z} - k(z - z_0) + I_{nc}(z) = F_0 \sin(\omega t), \tag{4.13}$$

where $I_{nc}(z)$ represents van der Waals attractions between the cantilever and sample. This force can be expressed by [87]:

$$I_{nc}(z) = \frac{-H_{sb}R}{6(z - \zeta_0)^2}, \tag{4.14}$$

where $m$, $H_{sb}$ and $R$ represent the cantilever mass, the cantilever-sample Hamaker constant and the system effective radius, respectively. $\zeta_0$ is the inter-atomic distance introduced in [87] to avoid numerical divergence of the interaction force.
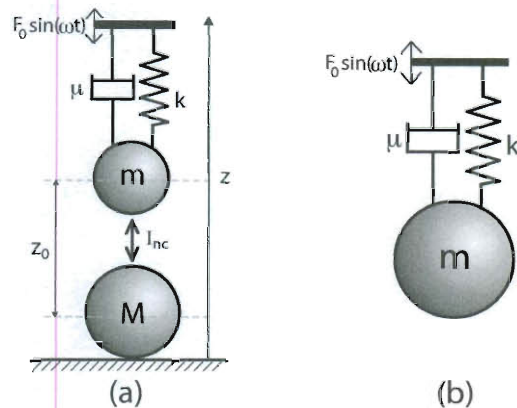


**Figure 4.16:** Approach phase (a) probe-sample lumped-parameters model (b) equivalent reduced model

A linear expansion can be made of the interaction force for the range of operation such that:

$$I_{nc}(z) \approx \frac{-HR}{6(z_0 - \zeta_0)^2} + \frac{HR}{3(z_0 - \zeta_0)^3}(z - z_0). \qquad (4.15)$$

The probe governing equation can be rewritten in the form:

$$m\ddot{z} + \mu\dot{z} - k^*(z - z0) = F_0 \sin(\omega t) + \frac{HR}{6(z_0 - \zeta_0)^2}, \qquad (4.16)$$

where the effective stiffness of the system $k^*$ is given by:

$$k^* = k - \frac{HR}{3(z_0 - \zeta_0)^3}. \qquad (4.17)$$

Assuming that the solution to equation (4.16) has the form:

$$z(t) = F_0|G(i\omega)|e^{-i\omega t}, \qquad (4.18)$$

the corresponding gain and phase are given by:

$$|G(i\omega)| = \frac{1}{\sqrt{(1 - (\omega/\omega_n)^2)^2 + (2\zeta\omega/\omega_n)^2}}, \qquad (4.19)$$

$$\phi(\omega) = \tan^{-1}\left(\frac{2\zeta\omega/\omega_n}{1 - (\omega/\omega_n)^2}\right), \qquad (4.20)$$

where $\zeta$ represents the viscous damping coefficient. The observed resonance frequency of the probe at an arbitrary position $z$ away from the surface is given by:

$$\omega_n(z) = \sqrt{\frac{k^*}{m}} = \sqrt{\frac{k}{m} - \frac{1}{m}\frac{\partial I_{nc}}{\partial z}\Big|_{z=z_0}}. \qquad (4.21)$$

Using the above formulas, the gradient of the interaction force can be estimated. In addition, accurate detection of the nano-sample capture can be achieved. This detection is very important at the nanoscale where optical techniques cannot be used for this purpose.

**Capture Phase:** In this phase, the nano-sample is captured by the probe through adhesion and transported to the desired position. In order to study the effect of the sample on the manipulation dynamics, we adopt the distributed model of the AFM cantilever (Figure 4.17).
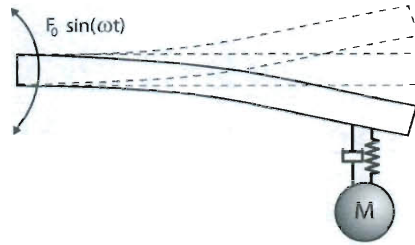
**Figure 4.17:** Capture phase model of the nanomanipulator

During this phase, the system can be represented as a cantilever with a mass-spring-damper end. The spring represents the nonlinear probe-sample contact forces $I_c$. Neglecting the damping, the flexural vibrations of the cantilever are governed by:

$$\rho A \ddot{u}(x,t) + EI u^{(4)}(x,t) = F_0 \sin(\omega t)\delta(x), \tag{4.22}$$

The corresponding BCs are given by:

$$u|_{x=0} = 0, \tag{4.23}$$

$$u^{(1)}|_{x=0} = 0, \tag{4.24}$$

$$u^{(2)}|_{x=L} = 0, \tag{4.25}$$

$$EI u^{(3)}|_{x=L} = \frac{3EI}{L^3}\bar{u}(L) - I_c(\Delta) - \mu\dot{\Delta} + M\ddot{\Delta}. \tag{4.26}$$

$L$, $A$, $I$, $\rho$ and $E$ are geometrical and material properties of the probe. We used $\dot{u} = \frac{\partial u}{\partial t}$ and $u^{(i)} = \frac{\partial^i u}{\partial x^i}$ to denote time and space derivatives. $\bar{u}$ and $\Delta$ represent the cantilever initial static deflection and the contact displacement, respectively. The proposed model takes into account the effects of the oscillations on the cantilever-sample contact through the damping and inertia terms in the force boundary condition at $x = L$. The contact displacement $\Delta$ is given by:

$$\Delta = z_0 - \bar{u}(L) - u(L,t). \tag{4.27}$$

The equilibrium between the probe and sample in the absence of the sinusoidal excitation of the cantilever base yields:

$$\frac{3EI}{L^3}\bar{u}(L) - I_c(z_0 - \bar{u}(L)) = 0. \tag{4.28}$$

The relation between the contact force and the contact displacement according to the MD contact model is highly nonlinear and implicitly given by the parametric equations defining the model as discussed in Chapter 2. For the purpose of the current section, we will approximate it by piecewise linear functions of the form:

$$I_c(\Delta) = k_1 \Delta + k_0. \tag{4.29}$$

The accuracy of the approximation can be increased by refining the discretization (Figure 4.18). However, this leads to increased computational cost.
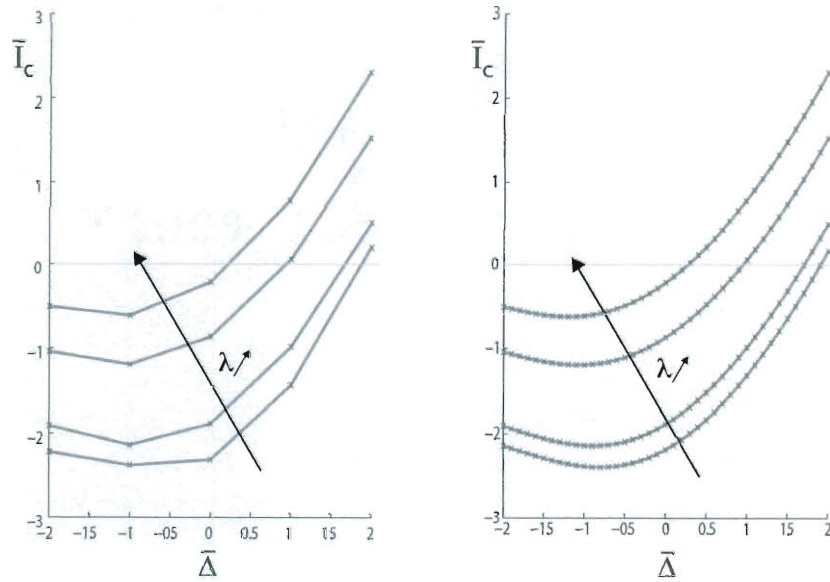


**Figure 4.18:** Piecewise linear approximation of the MD contact force

Substituting relations (4.28) and (4.29) in the expression of the force boundary condition at $x = L$, we obtain:

$$EIu^{(3)} = \frac{3EI}{L^3}\bar{u} - k_1(z_0 - \bar{u} - u) - k_0 - \mu\dot{\Delta} + M\ddot{\Delta}, \tag{4.30}$$

$$= k_1 u + \mu\dot{u} - M\ddot{u}. \tag{4.31}$$

Let $u(x,t) = U(x)e^{i\omega_n t}$. The eigenvalue problem associated with the considered cantilever

vibration can be written in the form:

$$U^{(4)}(x) - \alpha_n^2 U(x) = 0, \tag{4.32}$$

where $\alpha_n = \sqrt{\frac{\rho A}{EI}}\omega_n$. The corresponding BCs can be rewritten as:

$$U|_{x=0} = 0, \tag{4.33}$$

$$U^{(1)}|_{x=0} = 0, \tag{4.34}$$

$$U^{(2)}|_{x=L} = 0, \tag{4.35}$$

$$EIU^{(3)}|_{x=L} = \beta_n U|_{x=L}. \tag{4.36}$$

The coefficient $\beta_n$ is given by:

$$\beta_n = \frac{k_1}{EI} + \alpha_n^2 \frac{M}{\rho A} = \frac{k_1}{EI}\left(1 + \left(\frac{\omega_n}{\omega_c}\right)^2\right), \tag{4.37}$$

where $\omega_c = \sqrt{\frac{k_1}{M}}$. The corresponding transcendental equation is defined by:

$$\begin{aligned}
&-\alpha_n\sqrt{\alpha_n}\cos(\sqrt{\alpha_n}L)\cosh(\sqrt{\alpha_n}L)+\\
&\beta_n\left(\cos(\sqrt{\alpha_n})\sinh(\sqrt{\alpha_n}L) - \sin(\sqrt{\alpha_n}L)\cosh(\sqrt{\alpha_n}L)\right) = \alpha\sqrt{\alpha_n}.
\end{aligned} \tag{4.38}$$

For $\beta_n = 0$, the above relation reduces to the transcendental equation of a regular cantilever vibrations:

$$\cos(\sqrt{\alpha_n}L)\cosh(\sqrt{\alpha_n}L) = -1. \tag{4.39}$$

The modeshapes are given by:

$$\begin{aligned}
\psi_n(x) &= \cos(\sqrt{\alpha_n}x) - \cosh(\sqrt{\alpha_n}x)\\
&+\left(\frac{\cos(\sqrt{\alpha_n}L)+\cosh(\sqrt{\alpha_n}L)}{\sin(\sqrt{\alpha_n}L)+\sinh(\sqrt{\alpha_n}L)}\right)(-\sin(\sqrt{\alpha_n}x) + \sinh(\sqrt{\alpha_n}x)).
\end{aligned} \tag{4.40}$$

Thus, the forced vibrations of the cantilever can be expressed as:

$$u(x,t) = \sum_{n=1}^{\infty} \frac{F_0\psi_n(L)}{\omega_n^2 - \omega^2}\psi_n(x)\sin(\omega t). \tag{4.41}$$

**Release Phase:** When the manipulator reaches the desired final position, the sample must be released. The accuracy of this phase is crucial to the success of the manipulation. The equilibrium of the mass at the cantilever end gives:

$$k_1 \Delta + k_0 + \mu \dot{\Delta} + M \ddot{\Delta} = u(L) \omega^2 M \sin(\omega t). \tag{4.42}$$

For a given amplitude and frequency of the probe oscillations, the above relation yields the sample mass required for separation. Whenever the pull-off force is reached, the separation occurs. After release the nano-sample is subjected to different forces, namely gravity and attractive van der Waals forces with the probe and substrate denoted respectively by $F_g$, $F_c$ and $F_s$. Surface forces are dominant at the nanoscale. However, the effects of gravity and inertial forces cannot be neglected in this particular application. The sample force balance can be written as:

$$\begin{cases} m\ddot{y} = \dfrac{H_{sb} R \cos(\theta)}{6(\cos(\theta)[(D-y)-x \, \tan(\theta)]-\zeta_0)^2} - \dfrac{H_{ss} R}{6(y-\zeta_0)^2} - Mg \\ m\ddot{x} = \dfrac{H_{sb} R \sin(\theta)}{6(\cos(\theta)[(D-y)-x \, \tan(\theta)]-\zeta_0)^2} \end{cases} \tag{4.43}$$

where $x$, $y$ and $D$ denote the coordinates of the nano-sample and the release height, respectively. The angle $\theta$ is related to the amplitude of the probe oscillations $F_0$ through the geometrical relation:

$$tan^{-1}(\theta) = \frac{F_0}{L} \tag{4.44}$$

$H_{sb}$ and $H_{ss}$ represent the Hamaker constants of the probe-sample and sample-substrate interactions. The landing radius $R_L$, defined in Figure 4.19, characterizes the uncertainty after separation. A good estimate of the landing radius and its dependence on the main parameters of the manipulation are required.

The different formulas developed in this section show that the oscillations of the probe can be used to monitor the sample transport and realize the controlled release. As discussed earlier, the effects of the substrate topography on the manipulation are minimal specially during the transport phase. The previous developments assumed that only one sample is captured during the initial phase. In the next section, we will investigate the generalization of the proposed manipulation technique to multi-samples.
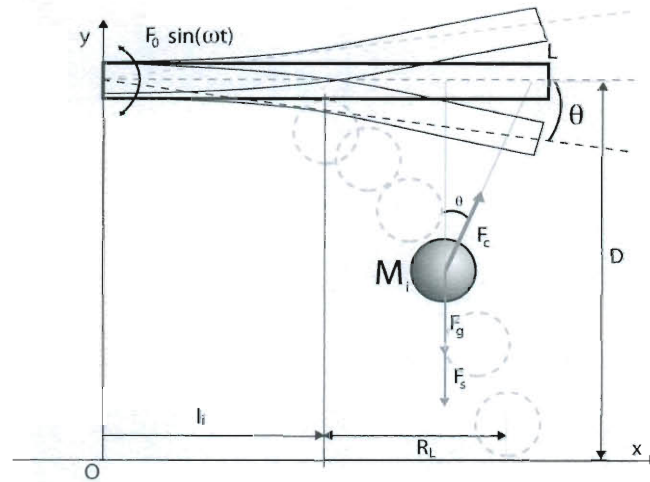
**Figure 4.19:** Free body diagram of the nano-sample after release

## 4.2.3 Multi-Sample Nano-Placing

Generalizing vibrational nano-placing to multi-samples will allow for parallel operation and increased speeds. However, this technique faces the hurdle of complex physics leading to difficult selective release. As a result, improved modeling of the relevant physics and dynamics is a must have to investigate the feasibility of parallel operation. During the capture phase, samples are captured by the probe through adhesion and transported to the desired position. The Rayleigh-Ritz method [126] can be used to study the effect of the additional masses on the dynamics of the manipulation. This technique can be employed to determine the number of attached samples or the attaching positions through monitoring the probe frequency. Rayleigh-Ritz method yields an approximation of the natural frequency of a system and requires the use of shape functions. A proper choice of these functions allows to obtain important information in the manipulation of an arbitrary number of samples.

Assuming that the flexural vibration of the probe-samples system is given by:

$$z(x) = \sum_i \alpha_i \psi_i(x),$$

(4.45)

where $\psi_i$ are shape functions, the corresponding maximum potential and kinetic energies can be expressed by:

$$U = \frac{1}{2}EI\int_0^L \sum_i \alpha_i \frac{\partial \psi_i^2(x)}{\partial x^2} \sum_j \alpha_j \frac{\partial \psi_j^2(x)}{\partial x^2} dx, \tag{4.46}$$

$$T = \frac{1}{2}\rho S\omega^2 \int_0^L \sum_i \alpha_i \psi_i^2(x) \sum_j \alpha_j \psi_j^2(x) dx, \tag{4.47}$$

where $E$, $I$, $\rho$ and $S$ are the cantilever's Young's modulus, moment of inertia, density and cross-sectional area, respectively. Rayleigh-Ritz method states that:

$$[\mathbf{K} - \omega^2 \mathbf{M}]\{\alpha_i\} = 0. \tag{4.48}$$

As this is true for an arbitrary set of coefficients $\{\alpha_i\}$, we obtain:

$$det(\mathbf{K} - \omega^2 \mathbf{M}) = 0. \tag{4.49}$$

In the case of the manipulation of $N$ samples, the stiffness matrix and mass matrix entries are given by:

$$K_{ij} = EI\int_0^L \frac{\partial^2 \psi_i(x)}{\partial x^2} \frac{\partial^2 \psi_j(x)}{\partial x^2} dx, \tag{4.50}$$

$$M_{ij} = \rho \int_0^L \psi_i(x)\psi_j(x)dx + \sum_{k=1}^N M_k \psi_i(l_k)\psi_j(l_k). \tag{4.51}$$

where $M_k$ is the mass of the $k^{th}$ transported sample.

Using the above expressions of $\mathbf{K}$ and $\mathbf{M}$, equation (4.49) can be rewritten in the form:

$$f(l_i, M_i, \omega) = 0 \qquad (i = 1..N). \tag{4.52}$$

Note that there are three variables in the above equation for a given index $i$, so at least two of them are needed to solve it. For example, if we know the attaching position of the samples and the resonant frequency, the masses $M_i$ can be calculated, or if the resonant frequency and the mass of a sample are known, its attaching position can be easily obtained.

When the manipulator reaches a desired position, the corresponding sample must be released. The release of the desired sample should be achieved without loosing contact with any other sample. The accuracy of this phase is crucial to the success of the manipulation. The equilibrium of the samples at their different attaching positions gives:

$$\begin{cases} k_{11}\Delta_1 + k_{10} + \mu\dot{\Delta}_1 + M_1\ddot{\Delta}_1 = u(l_1,t)\omega^2 M_1 \sin(\omega t) \\ k_{21}\Delta_2 + k_{20} + \mu\dot{\Delta}_2 + M_2\ddot{\Delta}_2 = u(l_2,t)\omega^2 M_2 \sin(\omega t) \\ \qquad \vdots \qquad\quad \vdots \qquad\quad \vdots \qquad\quad \vdots \\ k_{N1}\Delta_N + k_{N0} + \mu\dot{\Delta}_N + M_N\ddot{\Delta}_n = u(l_N,t)\omega^2 M_N \sin(\omega t) \end{cases} \qquad (4.53)$$

The coupling between the different equations of system (4.53) is ensured by the flexural vibrations of the probe-samples system. Several techniques were proposed in the literature to evaluate $u$. Qiao et al. [127] approach will be adopted in the present work. Qiao et al. formulas are valid to study the free flexural vibrations of non-uniform multi-step Euler Bernoulli beams carrying an arbitrary number of single-degree-of-freedom and two-degree-of-freedom systems. In the case of multi-sample nano-placing, the formulas will be adopted to the case of a uniform cantilever and the linear springs will be replaced by MD piecewise linear springs.

In the next section, simulations will be conducted in order to get a better insight into vibrational nano-placing manipulation dynamics. Both cases of single and multi-sample manipulation will be analyzed.

## 4.2.4   Simulation Results and Discussion

Simulating the manipulator dynamics during the approach, capture and release phases will be conducted. Emphasis is given to study the adhesion and sample mass effects. In addition, simulation results are provided to help select the frequency, amplitude and initial conditions of the release phase. The nano-placing manipulation model was implemented using build in MATLAB solvers. The numerical values used in the simulations are summarized in Table 4.4 [52, 122].

**Table 4.4:** Vibrational nano-placing simulations parameters

| PARAMETER | VALUE | PARAMETER | VALUE | PARAMETER | VALUE |
|---|---|---|---|---|---|
| $M=M_1$ | $2e{-}18$ kg | $m$ | $2e{-}12$ kg | $\omega$ | 2.5 k rad/s |
| $k$ | 1 N/m | $\mu$ | 0.1 | $\lambda$ | 2 |
| $R_t$ | $50e{-}9$ m | $R_s$ | $160e{-}9$m | $D$ | $5e{-}6$ m |
| $H_{sb}$ | $19.95e{-}20$ J | $H_{ss}$ | $13.2e{-}20$ J | $F_0$ | $5e{-}7$ N |
| $\zeta_0$ | $3.75e{-}10$ m | $L$ | $2e{-}3$ m | $M_2$ | $2e{-}18$ kg |

#### 4.2.4.1 Single sample manipulation

In this section, we will consider the case of single sample nano-placing. It is assumed that the initial phase results in a single sample being attached to the probe. The oscillations of the cantilever will be used to monitor the different phases of the manipulation.

**Approach Phase:** The analysis of this phase, based on the equations developed in the corresponding paragraph in the previous section, allows the detection of the sample capture and reveals the occurrence of the jump-into contact phenomenon. Figure 4.20-a represents the total force acting on the probe tip. When the force crosses the $x$-axis for a given value of $z_0$, the intersection point represents an equilibrium position where the tip-sample interactions and the cantilever restoring force are equal. The special case where the maximum of the net interaction force is equal to zero (marked by a square in the figure) corresponds to the jump-into contact phenomenon. In fact, while approaching the cantilever to the sample (decreasing $z_0$), a cantilever jump occurs reflecting the capture of the sample. Figures 4.20-b and 4.20-c represent the variations in the manipulator vibrations for different values of the separation distance $z_0$. Clearly, as $z_0$ decreases, the resonance frequency decreases. A practical method to insure that no loss of contact occurs while transporting the sample is through monitoring the manipulator vibrations.
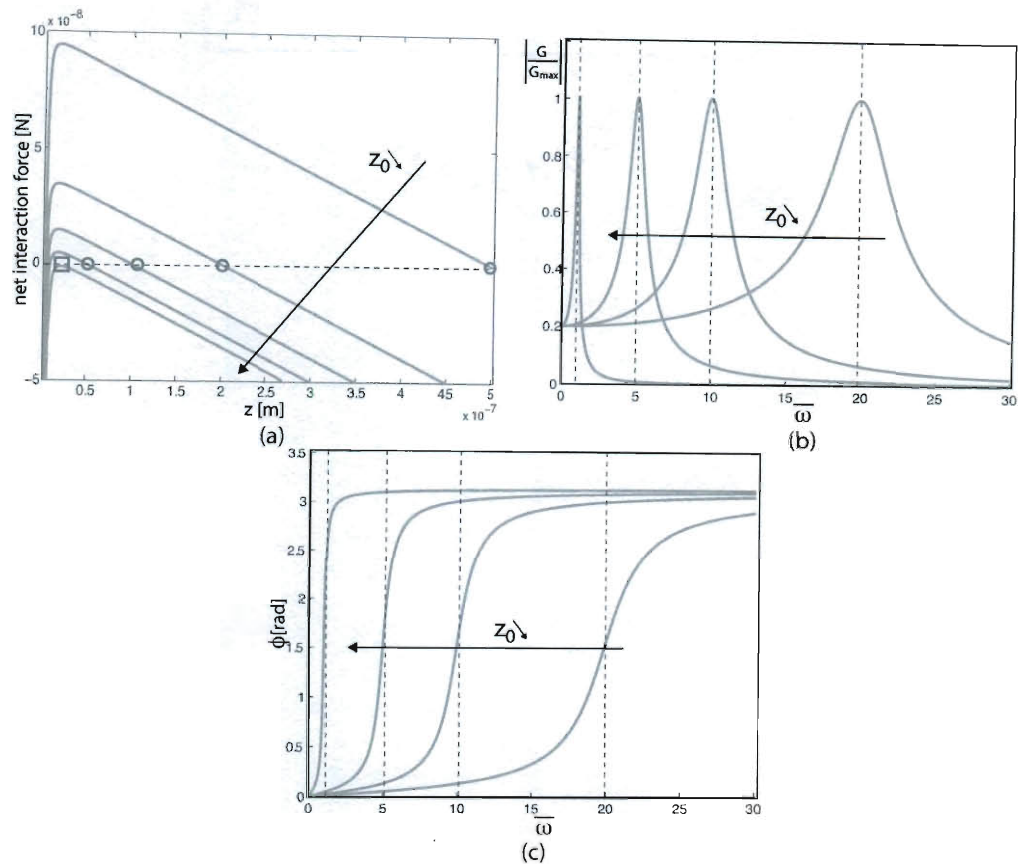
**Figure 4.20:** Approach phase simulations (a) force balance (b) cantilever oscillation gain and (c) phase variations as a function of $z_0$ ($\bar{\omega} = \omega/\sqrt{\frac{k}{m}}$)

**Capture Phase:** The capture phase starts when the sample adheres to the probe and includes its transport. For convenience, we assume that the sample is located at the free-end of the probe. In practical applications, the exact position of the sample during the capture phase can be known with high precision. Detecting the sample position relative to the cantilever was analyzed for mass detection applications using different methods and validated experimentally [128]. The focus in this section is how to ensure that the sample is not dropped during the capture phase. Analyzing the nanomanipulator oscillations is the answer (Figure 4.21). In fact, the captured sample affects the vibrations of the nanomanipulator as reflected by equation (4.38).
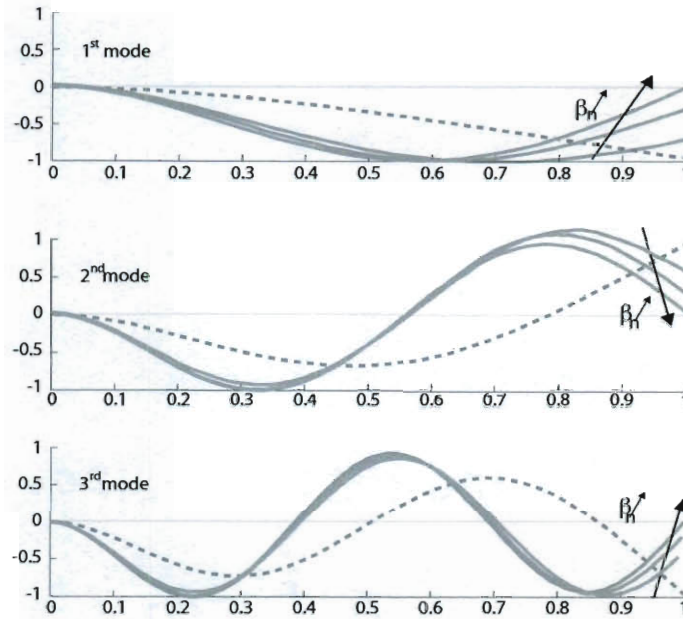
**Figure 4.21:** Nanomanipulator modeshapes for different values of $\beta_n$

Figure 4.21 represents the first three nanomanipulator modeshapes obtained for different values of $\beta_n$ (dashed curves correspond to $\beta_n = 0$). The aforementioned figure shows that increasing the value of $\beta_n$, which corresponds to heavier samples or stronger probe-sample adhesion, leads to the creation of a node at the cantilever free-end. The presence of the nano-sample affects also the natural frequency of the nanomanipulator. One important note is that heavier samples correspond to higher natural frequencies. Thus, monitoring the probe frequency can yield reliable information on the probe-sample contact.

**Release Phase:** As mentioned before, the success of the nano-placing manipulation depends largely on the accuracy of the release phase. A good understanding of the effects of the sample mass $M$ and release height $D$ on the landing radius $R_L$ is required in order to precisely position the sample. Using equation (4.42) for a given value of the amplitude and frequency of the nanomanipulator vibrations, there are three possible outcomes depending on the mass of the sample (Figure 4.22).
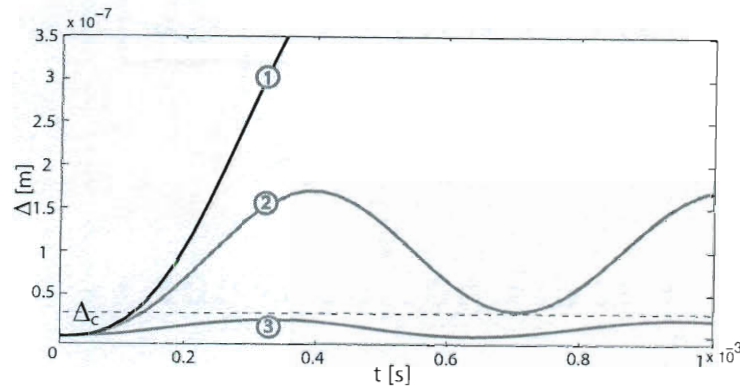
**Figure 4.22:** Evolution of contact displacement during the release phase for different sample mass values

If the sample mass is relatively high, the release occurs (plot (1)) and the sample lands on the substrate. However, when the inertial forces cannot overcome the cantilever-sample adhesion (plot (3)), the sample remains attached to the cantilever. The limiting case represented in plot (2) shows the recapture phenomenon. When the contact distance reaches the distance $\Delta_c$ corresponding to the pull-off force, the sample is released and then captured again as the nanomanipulator oscillates. For a given frequency, recapture occurs when the amplitude exceeds a critical value. Recapture should be avoided in practice.

Another important parameter that affects the release outcome is the release height $D$. In Figure 4.23, the variation of the sample coordinates during time is represented for different values of $D$. We conclude that depending on the release height, we may have the recapture of the sample as shown in plot (3). In fact, for a given oscillation amplitude the sample can be captured again if the distance $D$ is not high enough. The simulations show also that additional time is required for the sample to reach equilibrium on the substrate for higher release heights ($D = 7e-6m$ for plot (1) versus $D = 5e-6m$ for plot (2)). This is in agreement with simple physical intuition.

In the next section, we will consider the case of multi-sample manipulation. The practicality of selective release will be investiagted.
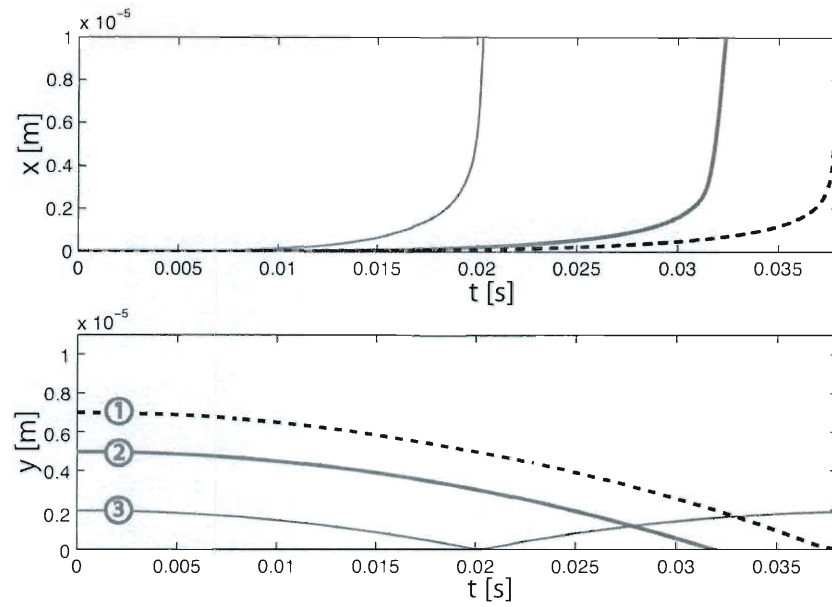
**Figure 4.23:** The coordinates of the nano-sample after release for different values of the release distance $D$

### 4.2.4.2 **Multi-sample** manipulation

The adopted manipulation scenario is the nano-placing of two samples. The sample masses $M_1$ and $M_2$ are assumed to be known with high accuracy. The main focus of the section is to validate the feasibility of selective release. For this end, we will study the possibility of exploring the probe's vibration frequency and amplitude to achieve controlled release. The Rayleigh-Ritz method can be used to determine the attaching positions of the samples denoted by $l_1$ and $l_2$ (Figure 4.24). An accurate approximation of these positions is needed to improve the estimation of the landing radius and thus the positioning accuracy. Using polynomial shape functions, the mass and stiffness matrices in the case of the adopted manipulation scenario are given by:

$$\mathbf{M} = \begin{bmatrix} \frac{1}{5}\rho SL^5 + \sum_{i=1}^{2} M_i l_i^4 & \frac{1}{6}\rho SL^6 + \sum_{i=1}^{2} M_i l_i^5 \\ \frac{1}{6}\rho SL^6 + \sum_{i=1}^{2} M_i l_i^5 & \frac{1}{7}\rho SL^7 + \sum_{i=1}^{2} M_i l_i^6 \end{bmatrix}, \tag{4.54}$$

$$\mathbf{K} = \begin{bmatrix} 4EIL & 6EIL^2 \\ 6EIL^2 & 12EIL^3 \end{bmatrix}. \tag{4.55}$$
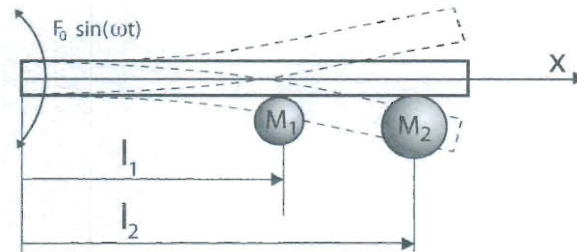


**Figure 4.24:** Multi-sample nano-placing simulation scenario

Knowing the sample masses, equation (4.52) can be solved for a given oscillating resonance frequency to obtain the corresponding attaching positions. Solving the system of equations for the selected frequency $\omega$ leads to $l_1 = 0.5L$ and $l_2 = L$. Thus, the simulation scenario is equivalent to the transport of two masses one at the mid-span of the probe and the second at its free-end. Simulations were then run to study the release phase (Figure 4.25 and Figure 4.26).
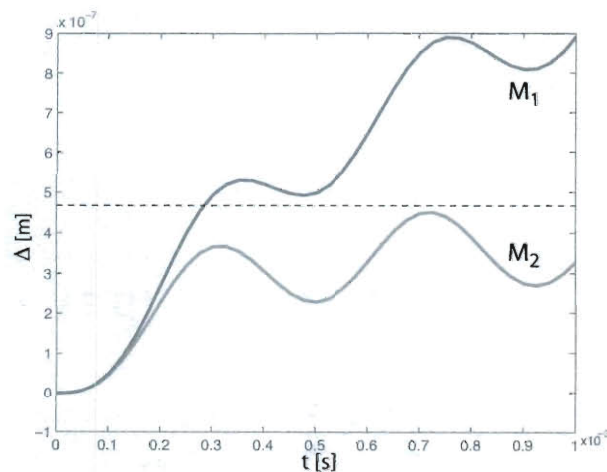


**Figure 4.25:** Frequency-based selective release ($\omega = 2.5\ krad/s$)
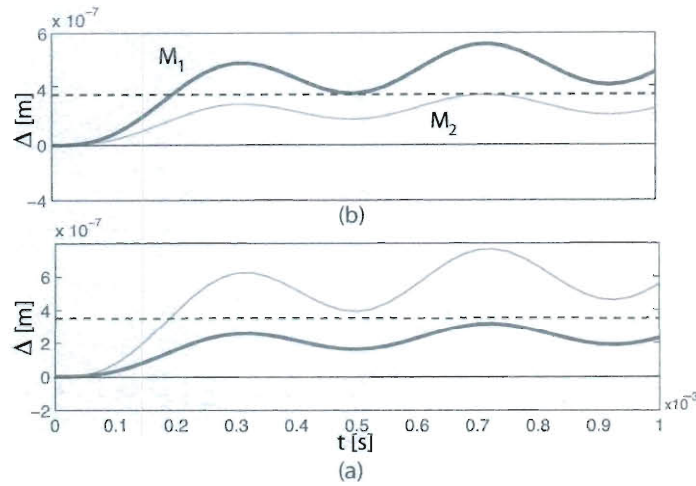
**Figure 4.26:** Amplitude-based selective release (a) $F_0 = 5e{-}7N$ (b) $F_0 = 1e{-}6N$

Results show that selective release of samples is possible using the oscillation frequency or amplitude. As shown in Figure 4.25, the oscillation frequency can be chosen such that a specific sample is released (sample 1 in this case) while the other sample remains attached to the probe. The selection of the oscillation frequency depends mainly on the sample masses and attaching positions. The same conclusions apply to using the vibrations amplitude to achieve selective release (Figure 4.26). For an amplitude of $F_0 = 5e{-}7N$, sample 1 is released while sample 2 is still located at the attaching position $l_2$. The oscillation amplitude must then be increased to $F_0 = 1e{-}6N$ to release the second sample at the desired location.

The initial results on selective release are very promising with respect to ensuring parallel operation of vibrational nano-placing. However, a deeper understanding of the effects of the main parameters on the release accuracy is needed.

### 4.2.4.3 Effect of key parameters on the positioning accuracy

It is not sufficient to achieve the release, but an accurate estimate of the landing radius is required for precise positioning of the sample. In the case where the release succeeds, the $x$

coordinate of the sample corresponding to $y = 0$ represents the landing radius. The landing radius depends on the material properties of the cantilever and sample. In fact as shown in Figure 4.27, as the cantilever-sample Hamaker constant $H_{sb}$ (which is a measure of the corresponding interactions) increases, the influence of the substrate attraction decreases and the sample takes more time to come to rest. Thus, a good knowledge of the probe-sample-substrate material properties is required.
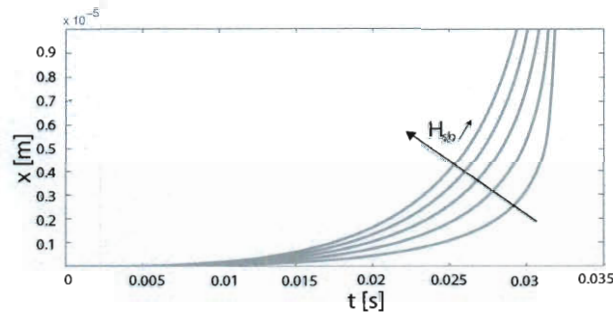


**Figure 4.27:** Effect of $H_{sb}$ on the sample $x$ coordinate

In order to have more control on the release phase, the operator needs to tune the nanomanipulator oscillations. Figure 4.28-a investigates the dependence of $R_L$ on the amplitude and frequency of the oscillations for a given mass of the sample. As it is expected, increasing the frequency and the amplitude of the oscillations lead to an increase in the landing radius. However, as it is clearly shown in the figure the effect of the amplitude is more important. It is essential to note that the release height needs to be adjusted for higher vibration amplitudes in order to avoid recapture.

We run additional simulations to investigate the effect of the sample mass on the landing radius (Figure 4.28-b). Interestingly, for a given oscillation frequency and amplitude lighter samples correspond to higher landing radius. This agrees with physical intuition since for light samples the effect of the gravity decreases and the dynamics of the sample after release are mainly affected by the relevant interactions. This result illustrates clearly the challenges facing nano-placing manipulation.
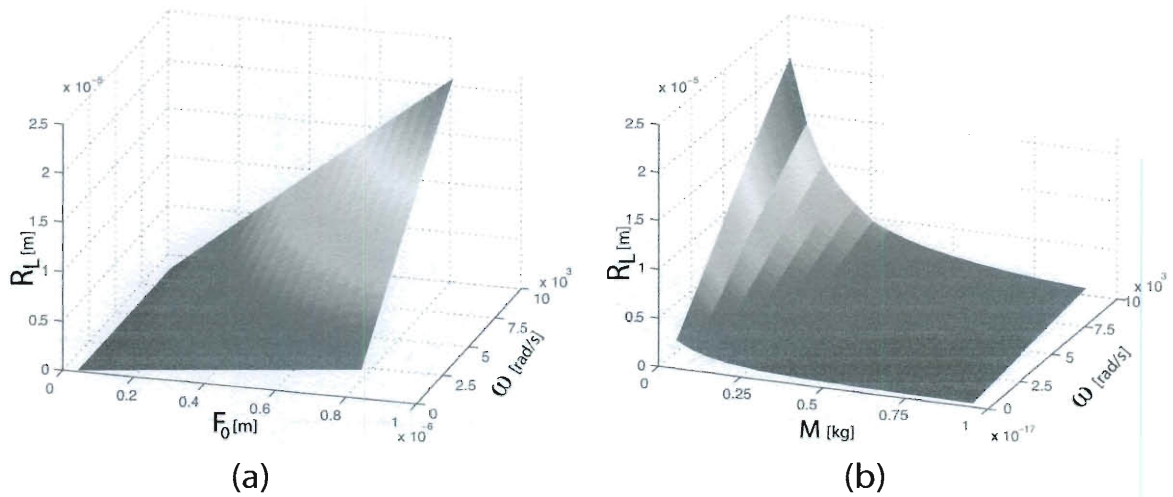
**Figure 4.28:** Effects of key parameters on $R_L$ (a) oscillation amplitude and frequency (b) sample mass and oscillation frequency

The main conclusion from this set of simulations is that for a given frequency and amplitude of the oscillations, the mass of the sample should be increased. On the other hand, for a given mass of the sample, the frequency and amplitude of the oscillations need to be increased to achieve the release. However, there are limitations to the allowed range of the nanomanipulator oscillations in order to avoid sample recapture and also imposed by the AFM setup design.

## 4.3 Conclusions

In the present chapter, nanomanipulation experiments were simulated. The manipulation scenarios include nano-pushing and nano-placing. The schemes exploit the relevant interactions at the nanoscale. The combination of improved physics modeling, advanced tools and proposed schemes are expected to make mechanical force manipulation a commercially viable fabrication process.

# Chapter 5

# Conclusions

Direct force nanomanipulation is a very promising bottom-up fabrication technique setting an interesting framework for nano-device diagnostics and analysis. The potential applications are of relevance in different fields including telecommunications, medicine and transport. This thesis develops new methods and techniques for direct force nanomanipulation using AFM probe force interactions. The developments are expected to enable the manipulation of nanoscale entities in a precise and controlled manner. The ultimate goal being to assemble and produce useful devices and systems at the nanoscale. The intellectual merit of this research stems from the development of new modeling of the physics and mechanics of probe interaction with nanoscale entities, coupled with the design of new smart probes with multiple degrees of freedom. Using the adopted modeling of the physics and the advanced capabilities of the new probes, improved nanomanipulation schemes can be implemented.

The physics at the nanoscale are complex making controllable manipulation difficult to achieve. An improved understanding of scale effects on motion and contact dynamics is crucial to avoid the use of restrictive contact conditions and limiting static considerations. In this thesis, we analyzed in depth the relevant physics and mechanics involved in probe-based mechanical nanomanipulation. These include nanoscale friction and surface force interactions. A new dynamic nano-friction model, introducing the notion of generalized bristle deflection, was proposed. The different model parameters are obtained using FFM scans. The scheme was validated by comparing simulated and experimental frictional data of different materials generally used as substrates in nanomanipulation. Results show that

the proposed model is able to represent the main characteristics of nano-friction including stick-slip and pre-sliding phenomena. Additional analysis demonstrates the ability of the proposed nano-friction model to represent the interesting reverse stick-slip behavior observed for VAMWCNTs.

Besides the improved understanding of friction at the nanoscale, an advanced modeling of the effects of surface force interactions was adopted. The proposed interaction model assumes that tip-sample contact phases can be represented using MD contact mechanics. Furthermore, the interactions during non-contact were taken into account as a superposition of short and relatively long van der Waals attractions. The continuity of the interactions during the transitions between non-contact and contact phases was ensured through the application of proper normalization. As a result, the adopted model can be applied to low and high adhesion systems and is able to represent a wide range of tip-sample characteristics. In addition, the analysis of the complete initial tip-sample collision process is possible. Using the adopted physics modeling, simulations were conducted to investigate the coupling between the friction and the interactions at the nanoscale. The gained knowledge is expected to help increase nanomanipulation accuracy.

On top of complex physics and dynamics at the nanoscale, current nanomanipulators suffer from restricted workspace and limited end-effector maneuverability. To address the lack of maneuverability, we proposed two new smart probes suitable for nanomanipulation. The term smart is used to emphasize the active nature of the probes relying respectively on duo-biomorph and piezotube actuators to realize accurate local tip motion. The first probe uses duo-biomorph extensions to generate vertical and lateral tip displacements. This design is perfect for nanomachining of vertical surfaces and controlled load nano-lithography. The second design employs a horizontal piezotube to allow for true maneuverability and 3D motion of the tip. Both probes include a frontal piezolayer used to tune the cantilever stiffness in-situ. In addition, the proposed designs offer simultaneous actuation and sensing of the tip motion facilitating their inclusion in haptic interfaces. Using the

adopted modeling of the physics and the advanced capabilities of the new probes, improved nanomanipulation schemes can be developed.

The most common probe-based manipulation scheme used at the nanoscale is nano-pushing. The first corresponding experimental investigations dates to 1991. In the present thesis, we analyzed nano-pushing manipulation in depth using the adopted physics modeling. Simulations show the occurrence of a sample stick-slip motion that may lead to reduced positioning accuracy. Nonlinear analysis were used to study the evolution of the stick-slip behavior. The obtained results bear important information that can help improve nano-pushing manipulation through the proper selection of the manipulation speed and loading force. However, this manipulation technique suffers from an inherent limitation related to the severe restrictions on the flatness of the substrate. To address this issue, a new manipulation scheme, labeled vibrational nano-placing, was proposed.

Vibrational nano-placing exploits the interactions at the nanoscale in order to move and arrange samples. The sample is captured by the probe then lifted and transported over relatively long distances. The vibrations of the probe are used to achieve the release of the sample in the desired location. The accuracy of the positioning is measured through the landing radius. Conducted simulations show that the landing radius depends on many factors, mainly the probe oscillations, the sample mass and the release high. Additional simulations investigated the generalization of nano-placing to multi-samples. Results are promising and show that the oscillation frequency and amplitude can be used to achieve selective release. Combining nano-pushing and nano-placing can offer a commercially viable fabrication technique at the nanoscale.

In summary, this thesis provides a solid foundation for probe-based manipulation at the nanoscale. Using the advanced physics modeling and new probe designs will enable the implementation of improved nanomanipulation schemes. It is expected that the gained knowledge from the conducted simulations can be used to create improved nanomanipulators and develop more advanced control strategies. A better selection of the different

parameters and estimation of the disturbances, ever present at the nanoscale, opens the door for higher accuracy and repeatability. When reached, the new levels of direct force manipulation will make it a commercially viable fabrication process and constitute an essential step forward in the long path towards nanorobots.

# Bibliography

[1] G. Cao, *Nanostrutures and Nannomaterials: Synthesis, Properties and Applications.* Imperial College Press, 2004.

[2] *NNI Investments by Agency 2001-2010.* NNI, 2010.

[3] S. A. Edwards, *The Nanotech Pioneers: Where Are They Taking Us?* Wiley-VCH, 2006.

[4] F. Biscarini, J. Chen, R. Komanduri, and C. Taliani, "NSF-EC workshop on nanomanufacturing and processing," tech. rep., NSF, 2002.

[5] *Nanotechnology Revolutionary Opportunities and Societal Implications*, 3rd Joint EC-NSF Workshop on Nanotechnology, 2002.

[6] *Tools and Instruments for Research and Manufacturing*, 4th Joint EC-NSF Workshop on Nanotechnology, 2002.

[7] B. Bhushan, ed., *Springer Handbook of Nanotechnology.* Springer, 2004.

[8] K. E. Drexler, *Nanosystems: Molecular Machinery, Manufacturing and Computation.* Johm Wiley and Sons, 1992.

[9] W. J. Li, N. Xi, W. K. Fung, and T. S. Wong, "Nanorobotics and nanomanipulation," *Encyclopedia of Nanoscience and Nanotechnology*, pp. 351–365, 2004.

[10] F. H. Ghorbel and F. Landolsi, "Mechanical nanomanipulation." Internal Report, RiSYS Lab, Department of Mechanical Engineering and Materials Science, Rice University, 2010.

[11] N. Bowden, A. Terfort, J. Carbeck, and G. M. Whitesides, "Self-assembly of mesoscale objects into ordered two-dimensional arrays," *Science*, vol. 276, pp. 233–235, 1997.

[12] A. K. Boal, F. Ilhan, J. E. DeRouchey, T. Thurn-Albrecht, T. P. Russell, and V. M. Rotello, "Self-assembly of nanoparticles into structured spherical and network aggregates," *Nature*, vol. 404, pp. 746–748, 2000.

[13] T. R. Ramachandrany, C. Baur, A. Bugacov, A. Madhukar, B. E. Koel, A. Requicha, and C. Gazen, "Direct and controlled manipulation of nanometer-sized particles using the non-contact atomic force microscope," *Nanotechnology*, vol. 9, pp. 237–245, 1998.

[14] M. Setti, "Micro- and nano-scale robotics," in *Proceeding of the 2004 American Control Conferen, Boston, Massachusetts June 30 -July 2*, 2004.

[15] C. C. Doumanidis, "Nanomanufacturing: technical advances, research challenges, and future directions," *Proceedings of the Institution of Mechanical Engineers, Part N: Journal of Nanoengineering and Nanosystems*, vol. 218, pp. 51–70, 2004.

[16] M. Falvo, G. Clary, A. Helser, S. Paulson, R. Taylor, V. Chi, J. F.P. Brooks, S. Washburn, and R. Superfine, "Nanomanipulation experiments exploring frictional and mechanical properties of carbon nanotubes," *Microscopy and Microanalysis*, vol. 4, 1999.

[17] M. R. Falvo, R. M. T. II, A. Helser, V. Chi, F. P. B. Jr, S. Washburn, and R. Superfine, "Nanometre-scale rolling and sliding of carbon nanotubes," *Nature —VOL 397*, vol. 397, pp. 236–238, 1999.

[18] Zyvex Instruments, *Zyvex S100 Nanomanipulator: The Premier Choice for Nanomanipulation Inside a High-Resolution Imaging Tool*, 2007.

[19] G. Binnig, H. Rohrer, C. Gerber, and E. Weibel, "Tunneling through a controllable vacuum gap," *Applied Physics Letters*, vol. 40, pp. 178–180, 1982.

[20] G. Binnig, H. Rohrer, C. Gerber, and E. Weibel, "Surface studies by scanning tunneling microscopy,"

[21] J. A. Stroscio and D. M. Eigler, "Atomic and molecular manipulation with the scanning tunneling microscope," *Science*, vol. 254, pp. 1319–1326, 1991.

[22] G. Binnig, C. F. Quate, and C. Gerber, "Atomic force microscope," *Physical Review Letters*, vol. 56, pp. 930–934, 1986.

[23] D. M. Schaefer, R. Reifenberger, A. Patil, and R. P. Andres, "Fabrication of two-dimensional arrays of nanometer-size clusters with the atomic force microscope," *Applied Physics Letters, 20 February 1995*, vol. 66 (8), pp. 1012–1014, 1995.

[24] T. Junno, K. Deppert, L. Montelius, and L. Samuelson, "Controlled manipulation of nanoparticles with an atomic force microscope," *Applied Physics Letters*, vol. 66(26), pp. 3627–3629, 1995.

[25] M. Sitti and H. Hashimoto, "Controlled pushing of nanoparticles: Modeling and experiments," *IEEE/ASME Transactions on Mechatronics*, vol. 5(2), pp. 199–211, 2000.

[26] S. Decossas, F. Mazen, T. Baron, G. Bremond, and A. Souifi, "Atomic force microscopy nanomanipulation of Silicon nanocrystals for nanodevice fabrication," *Nanotechnology*, vol. 14, pp. 1272–1278, 2003.

[27] Tafazzoli, Pawashe, and Sitti, "Atomic force microscope based two-dimensional assembly of micro/nanoparticles," *IEEE*, 2005.

[28] F. J. Rubio-Sierra, W. M. Heckl, and R. W. Stark, "Nanomanipulation by atomic force microscopy," *Advanced Engineering Material*, vol. 7(4), pp. 193–196, 2005.

[29] R. Resch, A. Bugacov, C. Baur, B. Koel, A. Madhukar, A. Requicha, and P. Will, "Manipulation of nanoparticles using dynamic force microscopy: simulation and experiments," *Applied Physics A*, vol. 67, pp. 265–271, 1998.

[30] R. Resch, C. Baur, A. Bugacov, B. E. Koel, A. Madhukar, A. A. G. Requicha, and P. Will, "Building and manipulating three-dimensional and linked two-dimensional structures of nanoparticles using scanning force microscopy," *The ACS Journal of Surfaces and Colloids*, vol. 14, p. 6613, 1998.

[31] M. Ammi and A. Ferreira, "Haptically generated paths of an AFM-based nanomanipulator using potential fields," in *2004 4th IEEE Conference on Nanotechnology*.

[32] J. Zhang, N. Xi, G. Li, H. Y. Chan, and U. C. Wejinya, "Adaptable end effector for atomic force microscopy based nanomanipulation," *IEEE Transactions on Nanotechnology*, vol. 5(6), pp. 628–642, 2006.

[33] E. Du, H. Cui, and Z. Zhu, "Review of nanomanipulators for nanomanufacturing," *International Journal of Nanomanufacturing*, vol. 1, pp. 83–104, 2006.

[34] A. Ferreira and C. Mavroidis, "Virtual reality and haptics for nano robotics: A review study," *IEEE Robotics and Automation Magazine*, vol. 13, pp. 78–92, 2006.

[35] H. W. C. Postma, T. Teepen, Z. Yao, M. Grifoni, and C. Dekker, "Carbon nanotube single-electron transistors at room temperature," *Science*, vol. 293, no. 76-79, 2001.

[36] E. Gnecco, R. Bennewitz, T. Gyalog, and E. Meyer, "Friction experiments on the nanometer scale," *Journal of Physics: Condensed Matter*, vol. 13, pp. R619–R642, 2001.

[37] M. R. Falvo and R. Superfine, "Mechanics and friction at the nanometer scale," *Journal of Nanoparticle Research*, vol. 2, pp. 237–248, 2000.

[38] M. A. Lantz, S. J. O'Shea, and M. E. Welland, "Atomic-force-microscope study of contact area and friction on NbSe2," *Physical Review B*, vol. 55(16), pp. 10776–10784, 1997.

[39] S. Fujisawa, E. Kishi, Y. Sugawara, and S. Morita, "Atomic scale friction observed with a two-dimensional frictional force microscope," *Physical Review B*, vol. 51, pp. 7849–7857, 1995(12).

[40] J. Kerssemakers and J. T. M. D. Hosson, "Influence of spring stiffness and anisotropy on stick-slip atomic force microscopy imaging," *Applied Physics*, vol. 80(2), pp. 623–631, 1996.

[41] S. Fujisawa, E. Kishi, Y. Sugawara, and S. Morita, "Load dependence of two dimensional atomic scale friction," *Physical review B*, vol. 52(7), pp. 5302–5305, 1995.

[42] S. Morita, S. Fujisawa, and Y. Sugawara, "Spatially quantized friction with a lattice periodicity," *Surface Science Reports*, vol. 23, pp. 1–41, 1996.

[43] J. Israelachvili, *Intermolecular and Surface Forces*. Academic Press Limited, 2 ed., 1995.

[44] G. Li, N. Xi, H. Chen, C. Pomeroy, and M. Prokos, "Videolized atomic force microscopy for interactive nanomanipulation and nanoassembly," *IEEE Transactions on Nanotechnology*, vol. 4, pp. 605–615, 2005.

[45] Q. Zhou, P. Kallio, F. Arai, T. Fukuda, and H. N. Koivoc, "A model for operating spherical micro objects," in *International Symposium on Micromechatronics and Human Science*, 1999.

[46] A. Tafazzoli and M. Sitti, "Dynamic behavior and simulation of nanoparticle during nanoprobe-based positionning," in *Proceedings of the ASME International Mechanical Engineering Congress, Anaheim, CA, November 13-19*, 2004.

[47] A. Meurk, "Microscopic stick-slip in friction force microscopy," *Tribology Letters*, vol. 8, pp. 161–169, 2000.

[48] S. Saito, H. T. Miyazaki, T. Sato, and K. Takahashi, "Kinematics of mechanical and adhesional micromanipulation under a scanning electron microscope," *Journal of Applied Physics*, vol. 92, pp. 5140–5149, 2002.

[49] R. W. Stark, G. Schitter, and A. Stemmer, "Velocity dependent friction laws in contact mode atomic force microscopy," *Ultramicroscopy*, vol. 100, pp. 309–317, 2004.

[50] H. Olsson, *Control Systems with Friction*. PhD thesis, Lund Institute of Technology, 1996.

[51] B. N. J. Persson, *Sliding Friction*. Springer, 2000.

[52] B. Bhushan, *Handbook of Micro/Nano Tribology*. CRC Press, 2 ed., 1999.

[53] N. Sasaki, K. Kobayashi, and M. Tsukada, "Atomic-scale friction image of graphite in atomic-force microscopy," *Physical Review B*, vol. 54, pp. 2138–2149, 1996.

[54] R. W. Carpick, D. F. Ogletree, and M. Salmeron, "Lateral stiffness: A new nanomechanical measurement for the determination of shear strengths with friction force microscopy," *Applied Physical Letters*, vol. 70, pp. 1548–1550, 1997.

[55] R. Carpick, E. Flater, K. Sridharan, D. Ogletree, and M. Salmeron, "Atomic-scale friction and its connection to fracture mechanics," *JOM*, pp. 48–52, 2004.

[56] S. Fujisawa, E. Kishi, Y. Sugawara, and S. Morita, "Two-dimensionally discrete friction on the NaF(100) surface with the lattice periodicity," *Nanotechnology*, vol. 5, pp. 8–11, 1994.

[57] C. M. Mate, G. M. McClelland, R. Erllandsson, and S. Chiang, "Atomic-scale friction of a tungsten tip on a graphite surface," *Physical Review Letters*, vol. 59, pp. 535–577, 1987.

[58] L. Howald, R. Luthi, E. Meyer, Guthner, and H. Guntherodt, "Scanning force microscopy on the Si (111) 7 x 7 surface reconstruction," *Zeitschrift for Physik B*, vol. 93, pp. 267–268, 1994.

[59] L. Howald, H. Haefke, R. Luthi, E. Meyer, G. Gerth, H. Rudin, and H. Guntherodt, "Ultrahigh-vaccum scanning force microscopy: Atomic-scale resolution at monatomic cleavage steps," *Physical Review B*, vol. 49, pp. 5651–5656, 1994.

[60] L. Howald, R. Luthi, E. Meyer, and H. Guntherodt, "Atomic-force microscopy on the Si (111) 7 x 7 surface," *Physical Review B*, vol. 51, pp. 5484–5487, 1995.

[61] R. Bennewitz, T. Gyalog, M. Guggisberg, M. Bammerlin, E. Meyer, and H.-J. Guntherodt, "Atomic-scale stick-slip processes on Cu(111)," *Physical Review B*, vol. 60, pp. R11 301, R11 304, 1999.

[62] R. J. A. van den Oetelaar and C. F. J. Flipse, "Atomic-scale friction on diamond (111) studied by ultra-high vacuum atomic force microscopy," *Surface Science*, vol. 384, pp. 828–835, 1997.

[63] S. Fujisawa, Y. Sugawara, S. Ito, S. Mishima, T. Okada, and S. Morita, "The two-dimentional stick-slip phenomenon with atomic resolution," *Nanotechnology*, vol. 4, pp. 138–142, 1993.

[64] J. Lou and K.-S. Kim, "Effects of interfaces on nano-friction of vertically aligned multi-walled carbon nanotube arrays," *Materials Science and Engineering A*, vol. 483-484, pp. 664–667, 2008.

[65] J. Lou, F. Ding, H. Lu, J. Goldman, Y. Sun, and B. I. Yakobson, "Mesoscale reverse stick-slip nanofriction behavior of vertically aligned multiwalled carbon nanotube superlattices," *Applied Physics Letters*, vol. 92, pp. 203115–1–203115–3, 2008.

[66] H. Kinoshita, I. Kume, M. Tagawa, and N. Ohmae, "High friction of a vertically aligned carbon-nanotube film in microtribology," *Applied Physics Letters*, vol. 85, pp. 2780–2781, 2004.

[67] K. Gjerde, J. Kjelstrup-Hansen, C. H. Clausen, K. B. K. Teo, W. I. Milne, H.-G. Rubahn, and P. Boggild, "Carbon nanotube forests: a non-stick workbench for nanomanipulation," *Nanotechnology*, vol. 2006, pp. 4917–4922, 17.

[68] K. Miyake, M. Kusunoki, H. Usami, N. Umehara, and S. Sasaki, "Tribological properties of densely packed vertically aligned carbon nanotube film on SiC formed by surface decomposition," *Nano Letters*, vol. 7, pp. 3285–3289, 2007.

[69] E. Gnecco, R. Bennewitz, T. Gyalog, C. Loppacher, M. Bammerlin, E. Meyer, and H.-J. Guntherodt, "Velocity dependence of atomic friction," *Physical Review Letters*, vol. 84, pp. 1172–1175, 2000.

[70] Y. Hoshi, T. Kawagishi, and H. Kawakatsu, "Velocity dependence and limitations of friction force microscopy of mica and graphite," *Japanese Journal of Applied Physics*, vol. 39, pp. 3804–3807, 2000.

[71] G. A. Tomlinson, "A molecular theory of friction," *Philosophical Magazine*, vol. 7, pp. 905–939, 1929.

[72] D. Tomanek, W. Zhong, and H. Thomas, "Calculation of an atomically modulated friction force in atomic-force microscopy," *Europhysics. Letters*, vol. 15, pp. 887–892, 1991.

[73] T. Gyalog, M. Bammerlin, R. Luthi, E. . Meyer, and H. Thomas, "Mechanism of atomic friction," *Europhysics Letters*, vol. 31, pp. 269–274, 1995.

[74] J. A. Hurtado and K.-S. Kim, "Scale effects in friction of single-asperity contacts. i. from concurrent slip to single-dislocation-assisted slip," *Proceedings of the Royal Society London A*, vol. 455, pp. 3363–3384, 1999.

[75] J. A. Hurtado and K.-S. Kim, "Scale effects in friction of single-asperity contacts. ii. multiple-dislocation-cooperated slip," *Royal Society London A*, vol. 455, pp. 3385–3400, 1999.

[76] S. S. Rekhviashvili, "A dislocation mechanism of friction between a nanoprobe and solid surface," *Technical Physics*, vol. 47, pp. 278–280, 2002.

[77] W. G. Conley, A. Raman, and C. M. Krousgrill, "Nonlinear dynamics in Tomlinson's model for atomic-scale friction and friction force microscopy," *Journal of Applied Physics*, vol. 98, pp. 053519–1–053519–10, 2005.

[78] J. M. Carlson and A. A. Batista, "Constitutive relation for the friction between lubricated surfaces," *Physical Review E*, vol. 53(4), pp. 4153–4165, 1996.

[79] P. A. Bliman and M. Sorine, "Friction modeling by hysteresis operators. Application to Dahl, stiction and Stribeck effects," in *Proceedings of the Conference "Models of Hysteresis"*, 1991.

[80] P. A. Bliman and M. Sorine, "A system-theoretic approach of systems with hysteresis. Application to friction modeling and compensation.," in *Proceedings of The Second European Control Conference, Groningen, The Netherlands*, 1993.

[81] P. Dahl, "Solid friction damping of mechanical vibrations," *AIAA Journal*, vol. 14(12), pp. 1675–1682, 1976.

[82] Haessig and Friedland, "Modeling and simulation of friction," *Journal of Dynamical System Measurment and Control*, vol. 113, pp. 354–362, 1991.

[83] C. de Wit, H. Olsson, K. J. Astrom, and P. Lischinsky, "A new model for control of systems with friction," *IEEE Transactions on Automatic Control*, vol. 40(3), pp. 419–425, 1995.

[84] E. Velenis, P. Tsiotras, and C. C. de Wit, "Extension of the LuGre dynamic tire friction model to 2d motion," in *Proceedings of The Mediterranean Conference on Control and Automation*, 2002.

[85] R. W. Stark, G. Schitter, and A. Stemmer, "Tuning the interaction forces in tapping mode atomic force microscopy," *Phys. Rev. B*, vol. 68, p. 085401, Aug 2003.

[86] G. Schitter, P. Menold, H. F. Knapp, F. Allgower, and A. Stemmer, "High performance feedback for fast scanning atomic force microscopes," *Review of Scientific Instruments*, vol. 72, no. 8, pp. 3320–3327, 2001.

[87] R. Garcia and A. S. Paulo, "Dynamics of a vibrating tip near or in intermittent contact with a surface," *Physical Review B*, vol. 61(20), pp. 381–384, 2000.

[88] D. Maugis, *Contact, adhesion, and rupture of elastic solids*. Springer, 2000.

[89] D. Maugis, "Adhesion of spheres: The JKR-DMT transition using a Dugdale model," *Journal of Colloid and Interface Science*, vol. 150, pp. 243–269, 1992.

[90] T. R. Rodriguez and R. Garcia, "Tip motion in amplitude modulation (tapping-mode) atomic-force microscopy: Comparison between continuous and point-mass models," *Applied Physical Letters*, vol. 80, pp. 1646–1648, 2002.

[91] W. T. Thomson and M. D. Dahleh., *Theory of Vibration with Applications*. Pearson Education, 5 ed., 2003.

[92] L. Meirovitch, *Analytical methods in vibrations*. Macmillan, New York, 1967.

[93] H. J. Guntherodt, D. Anselmetti, and E. Meyer, eds., *Forces in scanning probe methods*. Kluwer Academic Publishers, 1994.

[94] U. Rabe, K. Janser, and W. Arnold, "Vibrations of free and surface-coupled atomic force microscope cantilevers: Theory and experiment," *Review of Scientific Instruments*, vol. 67, pp. 3281–3293, 1996.

[95] A. S. Paulo and R. Garcia, "Unifying theory of tapping mode atomic force microscopy," *Physical Review B*, vol. 66, pp. 041406–4, 2002.

[96] R. Garcia and R. Perez, "Dynamic atomic force microscopy methods," *Surface Science Reports 47 (2002)*, vol. 47, pp. 197–301, 2002.

[97] S. C. Minne, S. R. Manalis, and C. F. Quate, "Parallel atomic force microscopy using cantilevers with integrated piezoresistive sensors and integrated piezoelectric actuators," *Applied Physical Letters*, vol. 26, 2005.

[98] A. G. Onaran, M. Balantekin, W. Lee, W. L. Hughes, B. A. B. R. O. Guldiken, Z. Parlak, C. F. Quate, and F. L. Degertekin, "A new atomic force microscope probe with force sensing integrated readout and active tip," *Review of Scientific Instruments*, vol. 77, p. 023501, 2006.

[99] M. Muraoka and H. Ishikawa, "Nanomachining by rubbing at ultrasonic frequency under controlled shear force," tech. rep., Akita University, Japan, 2006.

[100] M. Muraoka, "Vibrational dynamics of concentrated-mass cantilevers in atomic force acoustic microscopy: Presence of modes with selective enhancement of vertical or lateral tip motion," *Journal of Physics: Conference Series*, vol. 61, pp. 836–840, 2007.

[101] J. Zhang, G. Li, and N. Xi, "Modeling and control of active end effector for the AFM based nano robotic manipulators," in *Proceedings of the 2005 IEEE International Conference on Robotics and Automation Barcelona, Spain*, 2005.

[102] Y. Chen, A. J. Dick, and F. H. Ghorbel, "Tip trajectories of a smart micro-cantilever beam: analysis and design," *Smart Materials and Structures*, vol. 18, pp. 115012–10, 2009.

[103] P. D. Lit, J. Agnus, C. Clevy, and N. Chaillet, "A four-degree-of-freedom microprehensile microrobot on chip," *Assembly Automation*, vol. 2004, pp. 33–42, 24.

[104] P. D. Lit, J. Agnus, and N. Chaillet, "The constitutive equations of a piezoelectric duo-bimorph," in *Proceedings of the 5th IEEE International Symposium on Assembly and Task Planning Besanqon, France*, 2003.

[105] T. Ohara and K. Youcef-Toumi, "Dynamics and control of piezotube actuators for subnanometer precision applications," in *Proceedings of the American Control Conference, Seattle, Washington, June*, 1995.

[106] L. Meirovitch, *Fundamentals of Vibrations*. McGraw-Hill, 2001.

[107] S. O. R. Moheimani, "Accurate and fast nanopositioning with piezoelectric tube scanners: Emerging trends and future challenges," *Review of Scientific Instruments*, vol. 79, p. 071101, 2008.

[108] H. Zhang, S. Dong, S. Zhang, T. Wang, Z. Zhang, and L. Fan, "Ultrasonic micromotor using miniature piezoelectric tube with diameter of 1.0 mm," *Ultrasonics*, vol. 44, pp. e603–e606, 2006.

[109] S. O. R. Moheimani and Y. K. Yong, "Simultaneous sensing and actuation with a piezoelectric tube scanner," *Review of Scientific Instruments*, vol. 79, p. 073702, 2008.

[110] D. Charnegie, "Frequency tuning concepts for piezoelectric cantilever beams and plates for energy harvesting," *(MA thesis, University of Pittsburgh, 2007)*, pp. 28–39.

[111] O. M. E. Rifai and K. Youcef-Toumi, "Coupling in piezoelectric tube scanners used in scanning probe microscopes," in *Proceedings of the American Control Conference Arlington, VA June 25-27*, 2001.

[112] F. H. Ghorbel and M. W. Spong, "Robustness of adaptive control of robots," *Journal of Intelligent Robotic Systems*, vol. 6, pp. 3–15, 1992.

[113] F. H. Ghorbel and M. W. Spong, "Integral manifolds of singularly perturbed systems with application to rigid-link flexible-joint multibody systems," *International Journal of Nonlinear Mechanics*, vol. 35, pp. 133–155, 2000.

[114] Z. Wang and F. H. Ghorbel, "Control of closed kinematic chains using a singularly perturbed dynamic model," *ASME Journal of Dynamic Systems, Measurement, and Control*, vol. 128, pp. 142–151, 2006.

[115] P. Kokotovic, H. K. Khalil, and J. O'Reilly, *Singular Perturbation Methods in Control: Analysis and Design*. The Society for Industrial and Applied Mathematics, 1999.

[116] F. Mokhtari-Nezhad, A. R. Saidi, and S. Ziaei-Rad, "Influence of the tip mass and position on the AFM cantilever dynamics: Coupling between bending, torsion and flexural modes," *Ultramicroscopy*, vol. 109, pp. 1193–1202, 2009.

[117] K. Johnson and J. Woodhouse, "Stick-slip motion in the atomic force microscope," *Tribology Letters*, vol. 5, pp. 155–160, 1998.

[118] Y. Yan, Q. Zou, and Z. Lin, "A control approach to high-speed probe-based nanofabrication," in *Proceedings of the 2009 American Control Conference Hyatt Regency Riverfront, St. Louis, MO, USA, June 10-12*, 2009.

[119] C. Baur, A. Bugacov, B. E. Koel, A. Madhukar, N. Montoya, T. R. Ramachandran, A. A. G. Requicha, R. Resch, and P. Will, "Nanoparticle manipulation by mechanical pushing: underlying phenomena and real-time monitoring," *Nanotechnology*, vol. 9, pp. 360–364, 1998.

[120] M. Ammi, A. Ferreira, and J.-G. Fontaine, "Virtualized reality interface for tele-micromanipulation," in *Proceedings of the 2004 IEEE International Conference on Robotics and Automation New Orleans, LA, USA*, 2004.

[121] J. T. Feddema, P. Xavier, and R. Brown, "Micro-assembly planning with van der Waals force," in *Proceedings of the 1999 IEEE International Symposium on Assembly and Task Planning Porto, Portugal*, 1999.

[122] Y. Rollot, S. Regnier, and J.-C. Guinot, "Simulation of micro-manipulations: Adhesion forces and specific dynamic models," *International Journal of Adhesion & Adhesives*, vol. 19, pp. 35–48, 1999.

[123] D. S. Haliyo, Y. Rollot, and S. Regnier, "Manipulation of micro-objects using adhesion forces and dynamical effects," in *Proceedings of the 2002 IEEE International Conference on Robotics & Automation Washington*, 2002.

[124] J. L. Streator, "Dynamic contact of a rigid sphere with an elastic half-space: A numerical simulation," *Journal of Tribology*, vol. 125, pp. 25–32, 2003.

[125] Y. Fang and X. Tan, "A dynamic JKR model with application to vibrational release in micromanipulation," in *Proceedings of the 2006 IEEE/RSJ International Conference on Intelligent Robots and Systems, Beijing, China*, 2006.

[126] A. Leissa, "The historical bases of the Rayleigh and Ritz methods," *Journal of Sound and Vibration*, vol. 287, pp. 961–978, 2005.

[127] H. Qiao, Q. Li, and G. Li, "Vibratory characteristics of flexural non-uniform Euler-Bernoulli beams carrying an arbitrary number of spring-mass systems," *International Journal of Mechanical Sciences*, vol. 44, pp. 725–743, 2002.

[128] H. Xie, J. Vitard, S. Haliyo, and S. Regnier, "High-sensitivity mass and position detection of micro-objects adhered to microcantilevers," *Journal of Micro-Nano Mechatronics*, vol. 4, pp. 17–25, 2008.